Buoyant plumes with inertial and chemical reaction-driven forcing

by

Michael C. Rogers

A thesis submitted in conformity with the requirements
for the degree of Doctor of Philosophy
Graduate Department of Physics
University of Toronto

Abstract

Buoyant plumes with inertial
and chemical reaction-driven forcing

Michael C. Rogers
Doctor of Philosophy
Graduate Department of Physics
University of Toronto
2010

Plumes are formed when a continuous buoyant forcing is supplied at a localized source. Buoyancy can be created by either a heat flux, a compositional difference between the fluid coming from the source and its surroundings, or a combination of both. In this thesis, two types of laminar plumes with different forcing mechanisms were investigated: forced plumes and autocatalytic plumes. The forced plumes were compositionally buoyant and were injected with inertial forcing into a fluid filled tank. The autocatalytic plumes were produced without mechanical forcing by buoyancy that was entirely the consequence of a nonlinear chemical reaction – the iodate-arsenous acid (IAA) reaction. This reaction propagates as a reacting front and produces buoyancy by its exothermicity, and by the compositional difference between the reactant and product. Both the forced and autocatalytic plumes were examined in starting and steady states. The starting, or transient, state of the plume occurs when it initially rises through a fluid and develops a plume head on top of a trailing conduit. The steady state emerges after the plume head has risen to the top of a fluid filled tank leaving only a persistent conduit. Plume behaviour was studied through experimentation, simulation, and by using simple theoretical analysis. We performed the first ever study of plumes as they crossed over the transition between buoyancy-driven to momentum-driven flow. Regardless of the driving mechanism, forced plumes were found to exhibit a single power law relationship that explains their ascent velocity. However, the morphology of the plume heads was found

to depend on the dominating driving mechanism. Confined heads were produced by buoyancy-driven plumes, and dispersed heads by momentum-driven plumes. Autocatalytic plumes were found to have rich dynamics that are a consequence of the interplay between fluid flow and chemical reaction. These plumes produced accelerating heads that detached from the conduit, forming free vortex rings. A second-generation head would then develop at the point of detachment. The detachment process for plumes was sensitively dependent on small fluctuations in their initial formation. In some cases, head detachment could occur multiple times for a single experimental run, thereby producing several generations of autocatalytic vortex rings. Head detachment was reproduced and studied using autocatalytic plume simulations. Autocatalytic flame balls, a phenomenon closely related to autocatalytic plumes, were also simulated. Flame balls were found to have three dynamical regimes. Below a critical radius, the smallest flame balls experienced front death. Above this radius, they formed elongating, reacting tails. The largest flame balls formed filamentary tails unable to sustain a reaction.

Acknowledgements

This thesis is dedicated to my mother, who told me once that my father could have been a rocket scientist, and to my father, who appreciates finer things in life than rocket science. Thank you Mom for being the best teacher I ever had.

Many people deserve more thanks than I can provide in this space. These people include my family, friends, and colleagues. Thank you for caring about my progress with this work, and most importantly thank you for providing so many distractions from my work throughout this journey.

I would like to express my deepest gratitude to my supervisor and mentor, Stephen Morris, for never running out of ideas and for having endless patience. Perhaps most importantly, I would like to thank Stephen for giving me the freedom to learn from my mistakes. Stephen, I could not have asked for a more wonderful experience as a graduate student than what I had as a member of your research group.

I would also like to thank my collaborators who contributed to the work in this thesis: Mick Mantle, Andrew Sederman, and Anne De Wit. It has been an absolute pleasure to work with all of you. Sadly, my collaborator Abdel Zebib passed away before our work together was finished, and also before I could extend my thanks to him for his contribution to this thesis.

Thank you to my thesis committee members, who helped guide me through this process and who read this thesis very carefully. Thank you for your insightful suggestions and comments. I know it was part of your job to be on my committee; thank you for doing it so well.

I could not have written this thesis without the love and support of my wife. Maria, thank you for being the glue that holds our family together and the engine that keeps us moving forward. Thank you for all of the sacrifices that you made so that this work could be completed. I am very lucky to be married to such a wonderful person.

To my son Maxwell, who is perhaps the youngest person to ever create an experimental plume in a laboratory, thank you for pointing out the differences between a plume and a "funny" plume. I will leave it up to the reader to determine what makes a plume funny.

Contents

List of Tables

List of Figures

Chapter 1

Introduction

From the eruption column of a volcano to the mushroom cloud of an atomic bomb, plumes of rising fluid form magnificent flow structures [1, 2]. It is therefore no wonder that plumes are a classic subject in fluid dynamics [3, 4]. In this thesis, we examine two novel types of buoyant plumes. The first is a forced plume, in which buoyant fluid is injected into a fluid filled tank. Such a plume is driven by an interesting combination of buoyancy and momentum. The second type is an autocatalytic plume, in which the source of buoyancy and the resulting flow is due entirely to an autocatalytic chemical reaction. This type is an especially simple example of a self-stirred reacting flow.

Hydrodynamic flows driven by chemical reactions have been studied since the discovery of fire, the oldest technology of humankind [5]. Exothermic combustion reactions produce buoyant flames in the form of rising, reacting plumes and thermals which are often highly turbulent [6]. In this thesis, we investigate laminar reacting plumes driven by the relatively gentle autocatalytic iodate-arsenous acid (IAA) reaction front. The behaviour of these autocatalytic plumes is very rich, and is studied for the first time in this thesis.

We begin with a discussion of relevant past work on plumes in Section 1.1, and follow this by reviewing the pertinent theory for buoyancy-driven flow in Section 1.2. This sets the context for our investigation of both forced and autocatalytic plumes. Following this, past research on the IAA reaction front, with a focus on combining reaction with buoyancy-driven flow, is reviewed in Section 1.3. In Section 1.4, we conclude the introduction with an overview of the thesis.

1.1 Plumes

Plumes and jets are flow structures of considerable interest [4, 7] due to their widespread occurrence in industrial and natural systems, from fuel injection [8] to mantle convection [9, 10, 11, 12]. Both jets and plumes occur when flow discharges from an isolated, submerged source. The distinction between jets and plumes is that a pure jet is driven only by momentum flux at the source, while a pure plume is driven only by buoyancy. If a discharge has a combination of both momentum and buoyancy, there is no sharp distinction between a jet and a plume, and flows span a continuum of possibilities between the two. Such a flow structure may equally well be referred to as a "buoyant jet" or a "forced plume"; the latter terminology is adopted in this thesis.

Not only do jets and plumes occur in a wide variety of phenomena at various scales, they are also studied in a vast array of geometric configurations and flow scenarios [13, 14]. The focus of this thesis is on relatively unconfined flows, not directly interacting with a boundary, and on flows taking place in a quiescent ambient medium of uniform density. By contrast, other important cases are jets and plumes in a crossflow or in a stratified fluid [14]. In addition, plumes can be effectively two-dimensional, as is the case for a plane jet or a line plume, which come from line sources. In this thesis, however, we focus in three-dimensional axisymmetric plumes or "round" jets from isolated sources. For a given set of experimental conditions, the most important factor determining jet or plume behaviour and evolution is whether the flow is laminar or turbulent, which is determined by the Reynolds number of the flow, discussed below in Section 1.2. In addition to being either laminar or turbulent, jets and plumes can be a mixture of both types of flow, with near-field laminar flow that gives way to a far-field turbulent flow [13]. The plumes described in this thesis are all of the laminar type.

Forced plumes can be positively buoyant, in the sense that buoyancy forces act in the same direction as the injected momentum. We performed the first detailed study of forced laminar plume heads. This work is discussed in Chapter 2 of this thesis. Plumes can also be negatively or neutrally buoyant, as in the pure jet limit. More complex forced plumes can have several sources of buoyancy, such as in double-diffusive salt fingers [15] or chemically reacting plumes [16, 17, 18]. We conducted the first investigation of autocatalytic chemical plumes, which is discussed in detail in Chapters 3– 5 of this thesis. In large scale plumes, reactions do not provide buoyancy but can still be of significant importance in the monitoring of environmental impact of chemical dispersal from industrial

effluent and smokestack emission [19].

The state of jet or plume evolution involves another important distinction: between a steady, well-developed flow and a *starting* plume or jet, the transient case for which the injected fluid is penetrating the ambient medium and growing in length. The majority of work on laminar jets and plumes has focused on the steady variety, since the persistence of the columnar conduit following behind the head plays a significant role in many geophysical processes. Long-lived plume conduits are believed to underlie the formation of mantle hot spots, such as the one responsible for the Hawaiian Island - Emperor Seamount chain [9], or the one that created the narrow band of thickened oceanic crust that runs along the Atlantic margin of North America [20]. Entrainment and flow in the conduit is important to the morphology and dynamics of all long-lived plumes, and this is investigated for forced and autocatalytic plumes in Chapter 4.

Before a laminar plume reaches a steady state, it develops its most visually striking feature as a starting plume: a well-defined, evolving head. A starting plume is shown in Fig. 1.1. Given the wide variety of types of jets and plumes, and the wide array of scientific contexts in which they are studied, it is no surprise that there is a lack of uniformity in the terminology used for jet and plume anatomy. We adopt the term *head* to describe the structure on top of the plume, and *conduit* to describe the fluid emanating from the source that connects and provides volume flux to the head. Some authors refer to a starting jet or plume head as a *cap*, and the conduit is sometimes called the *stem* or *corridor* in the literature. The conduit starts at the *outlet* of a small pipe, through which buoyant fluid is being pushed. Finally, we use the term *lobe* to describe the bottom, under-turning part of the head.

The most prominent feature of a laminar starting plume is the vortex ring that often forms in the plume head. The generation and evolution of vortex rings has been a subject of longstanding interest in fluid dynamics due to their natural beauty, their utility in engineering applications, and their rich history as simple solutions of the fluid equations [21]. Vortex rings can be produced experimentally by using a cylindrical piston to inject a finite volume of neutrally buoyant fluid into quiescent surroundings [22]. Continuously supplied, neutrally buoyant jets have also been used to study the velocity fields of evolving vortex rings [23]. In addition to neutral buoyancy scenarios, vortex ring formation and pinch-off has also been investigated in the context of buoyant starting plumes, where results suggest that dimensionless circulation of the ring is a universal quantity, regardless of whether it is produced by plume pinch-off or by a piston [24, 25].
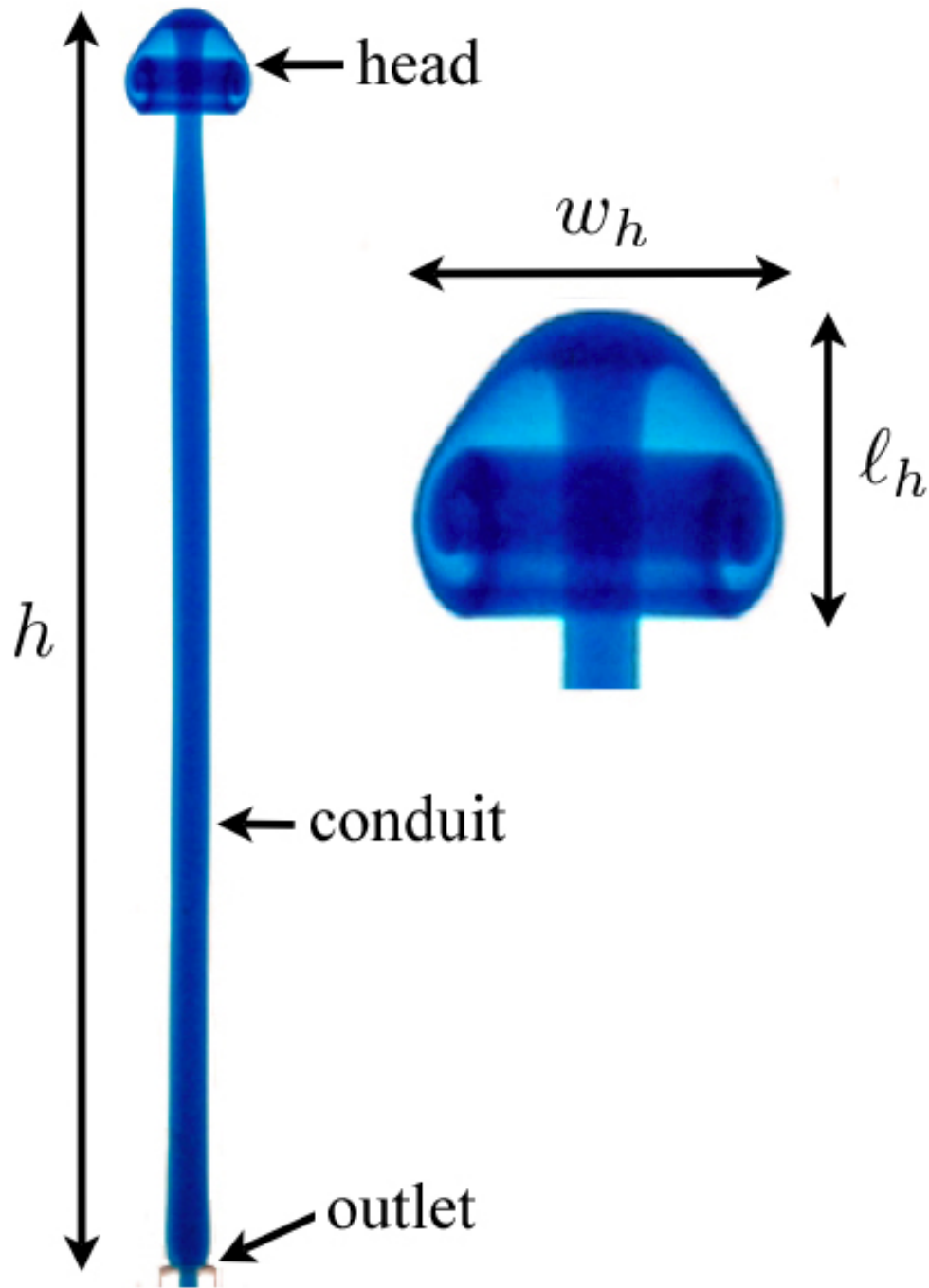
Figure 1.1: The anatomy of a laminar starting plume. The entire plume is shown on the left, while a magnified image of the head is shown on the right. h is the height of the plume from the outlet to the top of the head, w_h is the width of the head, and ℓ_h is the head length. The dyed plume shown is from set D5 (discussed in Chapter 2) and was created using an injected flow rate of $Q = 1.33 \times 10^{-1}$ mL/s. In this image, $h = 19.3$ cm, $w_h = 1.9$ cm, and $\ell_h = 1.6$ cm.

Buoyant vortex rings may also be created by the pinch-off of accelerating plumes driven by autocatalytic chemical reactions. We discovered this phenomenon, and it is discussed at length in Chapters 3 and 5.

Starting jets have attracted interest in studies of combustion [26], and starting plumes in the context of geophysical applications [9, 10, 11, 12]. Previous work on laminar starting plume heads has focused on ascent velocity [27, 28, 29], temperature and concentration measurements [30], velocity field measurements [31], and scaling laws for the head [28]. The dependence of thermally-driven plume flow on the Prandtl number Pr has been investigated [29]. The Prandtl number is defined and discussed further in Section 1.2.

Diverse plume experiments have yielded a number of plume head morphologies, such as *cavity* structures [11, 10], *umbrellas* [12], heads that encapsulate a vortex ring, like the one shown in Fig. 1.1, and heads that do not contain vortex motion in their lobe [28]. Some thermal plume heads become non-axisymmetric under sufficiently high forcing [32]. More recently, a numerical model of thermally driven 2D *line* plumes found four different dynamical regions of starting plume morphology [33].

While a variety of head structures are known, the nature of transitions in the type of head that forms as experimental parameters are varied has not been systematically explored. Moreover, the conditions under which a stable laminar head changes its morphology have received little attention. Similarly, the scaling of the ascent velocity of forced buoyant plumes has not been previously studied. The first systematic study of these issues is addressed in our experimental investigation of compositionally buoyant forced plumes discussed in Chapter 2.

1.2   Buoyancy-driven fluid flow

Autocatalytic and forced plumes are examples of buoyancy-driven fluid flow. Fluid flow is governed by the Navier-Stokes equations, which describe the motion of a fluid parcel located at any point in a flow field at any instant in time. For an incompressible fluid, the Navier-Stokes equations are

$$\frac{\partial \mathbf{u}}{\partial t} + (\mathbf{u} \cdot \boldsymbol{\nabla})\mathbf{u} = -\frac{1}{\rho}\boldsymbol{\nabla}p + \nu\nabla^2\mathbf{u} + \mathbf{g}, \qquad (1.1)$$

subject to the incompressibility constraint

$$\boldsymbol{\nabla} \cdot \mathbf{u} = 0. \tag{1.2}$$

Here $\mathbf{u}$ is the velocity vector, $\mathbf{g}$ is the gravitational acceleration, ρ is the fluid density, p is the pressure, and ν is the kinematic viscosity. The dimensions of each of the terms in this equation, in units of length L and time T, are L/T^2, the dimensions for acceleration.

The force of buoyancy arises in a gravitational field when there is a density difference $\Delta\rho = \rho - \rho_0$ between an object with density ρ_0 and the fluid with density ρ in which it is submerged. In this thesis, the "object" is the fluid comprising a plume, which is less dense than the fluid surrounding it. When the density difference responsible for buoyancy-driven flow involving two fluids is small, which is the case for all of the plumes examined in this thesis, the Boussinesq approximation can be made for the Navier-Stokes equations. Under the Boussinesq approximation, the difference in inertia between the two fluids is negligible and therefore density changes can be neglected in the Navier-Stokes equations for all terms with the exception of the gravity term. In this case, the magnitude of the gravity term g is expressed as the *reduced gravity*

$$g' = g\frac{\Delta\rho}{\rho_0}. \tag{1.3}$$

For a forced plume, the degree to which buoyancy affects flow emerging from a source with diameter d and velocity u is quantified by the dimensionless plume Richardson number

$$\mathrm{Ri} = \frac{g'd}{u^2} \tag{1.4}$$

which expresses the ratio of the buoyancy forces to the inertial terms in the Navier-Stokes equations. Thus, Ri can also be viewed as a measure of the extent to which convection is "forced", in the $\mathrm{Ri} \ll 1$ limit where inertial effects dominate, as opposed to "natural" or "free" convection which occurs in the purely buoyant, $\mathrm{Ri} \gg 1$ limit. An important morphological distinction between a plume produced by forced convection and one produced by free convection is discussed in Chapter 2.

In the source flow that produces a forced plume, the ratio of inertial forces to viscous forces in the Navier-Stokes equations is quantified by the dimensionless Reynolds number

$$\mathrm{Re} = \frac{ud}{\nu}. \tag{1.5}$$

To generalize Re for other flows, d is replaced by an appropriate horizontal or vertical length scale, L. For the flow of a plume head, for example, d can be replaced by the head width, w_h, or the head length, ℓ_h. The scaling of the plume head, and other parts of a plume are discussed further in Chapters 2 and 3. Roughly, the range of Re for the plume heads considered in this thesis is $10^{-1} < \mathrm{Re} < 10^2$. This range indicates that all of the plumes were laminar, as opposed to turbulent, which have higher Reynolds number flows.

In addition to injecting buoyant fluid by means of a source flow, buoyancy can also be driven by heating a fluid. In this scenario, the thermal expansion of a fluid is the mechanism behind buoyancy production. Thermal expansion is a thermodynamic property of a substance, and it is given by the thermal expansion coefficient

$$\alpha = -\frac{1}{\rho} \left(\frac{\partial \rho}{\partial T} \right)_p \tag{1.6}$$

where T is the temperature of the fluid, and the derivative is taken at constant pressure p. For small changes in density, density as function of temperature can therefore be written as

$$\rho(T) = \rho_i [1 - \alpha \Delta T] \tag{1.7}$$

where ΔT is the temperature difference caused by heating, and ρ_i is the initial density of the fluid.

When a fluid is heated, a dimensionless parameter that quantifies the forces driving fluid motion is the Rayleigh number

$$\mathrm{Ra} = \frac{g \alpha L^3}{\nu \kappa} \Delta T \ , \tag{1.8}$$

where κ is the thermal diffusivity. For large Ra in a fluid, heat transfer occurs predominantly by means of buoyancy-driven flow. For small Ra, however, heat transfer occurs primarily by conduction. While there is no temperature difference between the plume and its surrounding fluid in the forced plume experiments discussed in Chapter 2, heating of the fluid is relevant for the autocatalytic plumes discussed in Chapters 3–5.

Heat is produced in the reaction used to produce autocatalytic plumes (the IAA reaction), as it is slightly exothermic. In addition, there is also an isothermal density change due to the difference in partial molal volumes of the reactant and product solutions. For a reacting fluid with product concentration c, the compositional expansion coefficient is

analogous to the thermal expansion coefficient, and is written

$$\beta = -\frac{1}{\rho}\left(\frac{\partial \rho}{\partial c}\right)_T. \tag{1.9}$$

When both thermal and compositional effects contribute to the buoyancy of the product solution, the density dependence of the solution on T and c can be written as

$$\rho(T, c) = \rho_i[1 - \alpha \Delta T - \beta \Delta c]. \tag{1.10}$$

The contribution to buoyancy from each of these thermal and compositional effects may be characterized separately by two different Rayleigh numbers,

$$\text{Ra}_T \quad = \quad \frac{g\alpha L^3}{\nu D_c}\Delta T \quad \text{and} \quad \text{Ra}_c = \frac{g\beta L^3}{\nu D_c}\Delta c , \tag{1.11}$$

where D_c is the molecular diffusivity of species c and Δc is the concentration difference between the reacted and unreacted fluid. These Rayleigh numbers are discussed further in the context of autocatalytic plumes in Section 3.2.2, and are used as part of the formulation for a numerical model of autocatalytic plumes discussed in Section 5.1.1.

When thermal and compositional effects are present in a fluid flow, the relative importance of thermal and molecular diffusivities is quantified by the dimensionless Lewis number

$$\text{Le} = \kappa/D_c. \tag{1.12}$$

To quantify the relative effects of thermal and molecular diffusivity to momentum diffusivity (viscosity) on the fluid flow, two separate dimensionless quantities are used. These are the Schmidt number,

$$\text{Sc} = \nu/D_c, \tag{1.13}$$

for molecular diffusivity, and the ratio of Sc and Le, the Prandtl number,

$$\text{Pr} = \nu/\kappa, \tag{1.14}$$

for thermal diffusivity. Le is also the factor by which Ra_T is greater than Ra. These dimensionless numbers are used to characterize plumes throughout this thesis.

1.3 Chemical reaction fronts

The unique behaviour of autocatalytic plumes in comparison with other laminar plumes is discussed throughout Chapters 3–5. The mechanisms that create this unique behaviour arise because of the dynamic interplay between the reaction front and buoyancy-driven fluid flow. Buoyancy-driven plumes were introduced in the preceding Section; this Section discusses the formation of chemical reaction fronts.

In the absence of fluid flow, the reaction-diffusion equation for a chemical species with concentration c is

$$\frac{\partial c}{\partial t} = D_c \nabla^2 c + F(c), \tag{1.15}$$

where D_c is the diffusion constant for species c and $F(c)$ is the reaction term. If there is no reaction, $F(c) = 0$ and Eq. 1.15 becomes the diffusion equation. Traveling chemical waves can be the result of a reaction-diffusion process, provided that the reaction exhibits some form of kinetic feedback such as autocatalysis [34]. Chemical waves occur in two distinctly different forms: propagating pulses and propagating fronts. The most famous chemical waves are the propagating pulses found in the Belousov-Zhabotinsky (BZ) reaction. In the BZ reaction, as a pulse of reactivity passes through a point, the intermediates of the chemical reaction undergo a departure from their original concentration, and return to their original state as the pulse passes by. During this process only a small amount of the reactants are depleted; therefore the original state of the solution is effectively regenerated in the wake of the pulse [35].

Like a propagating pulse of chemical reactivity, a propagating front consists of a chemical reaction that causes the chemical species involved in the reaction to undergo a concentration excursion. However, unlike propagating pulses, the original state of the solution is not restored in the wake of the front. Instead, a new solution - a reaction product that cannot be changed back into the original reactant solution - is left behind. Such behaviour was first observed in the iodate - arsenous acid (IAA) reaction in 1955 by Epik and Shub [36]. However, interest in the propagating front behaviour of the IAA reaction did not begin to blossom until many years later, when the buoyancy-producing effects of the IAA reaction was first considered. In the following Section, we discuss the IAA chemical reaction, and follow this with a review of the literature involving the IAA reaction coupled with buoyancy driven fluid flow.

1.3.1 Iodate arsenous-acid reaction chemistry

The propagating front in the IAA reaction consumes reaction mixture that is in a state where very little reaction has occurred and leaves in its wake a nearly fully reacted solution. The IAA reaction is described by two coupled reaction steps, each of which consumes a product in the other reaction step. In the Dushman reaction (A) [37] iodide is oxidized by iodate

$$IO_3^- + 5I^- + 6H^+ \rightarrow 3I_2 + 3H_2O. \tag{A}$$
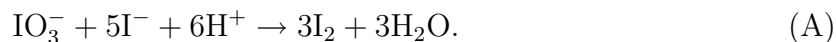
The Roebuck reaction (B) [38, 39, 34] involves the rapid reduction of iodine back to iodide by arsenous acid

$$AsO_3^{3-} + I_2 + H_2O \rightarrow 2I^- + AsO_4^{3-} + 2H^+. \tag{B}$$
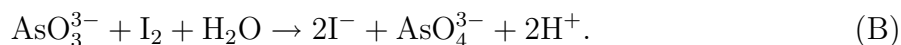
The result is a feedback mechanism where the autocatalysts I^- and H^+ are regenerated by reaction (B) for consumption in reaction (A). The rate laws of these reactions have been empirically determined to be

$$R_A = -\frac{1}{5}\frac{d[I^-]}{dt} = (k_1 + k_2[I^-])[IO_3^-][H^+]^2[I^-], \tag{1.16}$$

for reaction (A) [40] and

$$R_B = -\frac{d[I_2]}{dt} = \frac{k_3[I_2][H_3AsO_3]}{[I^-][H^+]}. \tag{1.17}$$

for reaction (B) [38, 41]. The rate constants k_1, k_2, and k_3 were found to be [34]

$$
\begin{aligned}
k_1 &= 4.5 \times 10^{-2} M^{-3} s^{-1} \\
k_2 &= 1.0 \times 10^{-8} M^{-4} s^{-1} \\
k_3 &= 3.2 \times 10^{-2} M s^{-1}.
\end{aligned}
\tag{1.18}
$$

In the IAA reaction, when the initial arsenous acid concentration is in stoichiometric excess to iodate ($[As(III)]_0 > 3[IO_3^-]_0$) the net reaction is (A) + 3(B), or

$$IO_3^- + 3H_3AsO_3 \rightarrow I^- + 3H_3AsO_4. \tag{1.19}$$

The rate of process (A) depends on iodide concentration, and the iodine product from

(A) is reduced by the faster process (B) to regenerate iodide. Thus, iodide concentration undergoes an autocatalytic increase until the iodate in solution is completely consumed. Starch indicates the presence of iodine in solution. When starch is present in excess arsenous acid solutions, the propagating front appears as a thin blue line, with clear solution both preceding and in the wake of the propagating front. When iodate is in stoichiometric excess to arsenous acid ($[\text{As(III)}]_0 < 5/2[\text{IO}_3]_0$) the net reaction is 2(A) + 5(B), or

$$2\text{IO}_3^- + 5\text{H}_3\text{AsO}_3 + 2\text{H}^+ \rightarrow \text{I}_2 + 5\text{H}_3\text{AsO}_4 + \text{H}_2\text{O} \tag{1.20}$$

Once again, an autocatalytic production of iodide according to (A) + 3(B) occurs, however for this case it is limited by the amount of arsenous acid present, rather than by the amount of iodate. The iodide that accumulates is then oxidized to iodine by process (A) and the result is the net reaction (1.20) [42]. Starch indicator in these solutions causes the front and all of the solution that it has consumed to appear blue. When the initial reaction mixture contains $\frac{5}{2}[\text{IO}_3^-]_0 < [\text{As(III)}]_0 < 3[\text{IO}_3^-]_0$, the net reaction is described by an appropriate linear combination of reactions (1.19) and (1.20).

The chemical composition of the solution we use in our experiments had an excess of arsenous acid, and therefore the overall reaction stoichiometry follows Eq. 1.19. Preparation of the IAA reactant solution for our experiments is discussed in Section 3.1.1. The net rate of iodate consumption in this reaction follows a cubic rate law [43, 44]

$$-\frac{\text{d}[\text{IO}_3^-]}{\text{dt}} = k_c[\text{I}^-]^2[\text{IO}_3^-], \tag{1.21}$$

where k_c is the rate constant. The generalized cubic autocatalytic chemical reaction for reactants A and B, where B is the autocatalyst, is

$$\text{A} + 2\text{B} \rightarrow 3\text{B}. \tag{1.22}$$

Denoting $a=[\text{A}]$ and $b=[\text{B}]$, the rate of reaction is

$$-\frac{da}{dt} = k_c ab^2 \tag{1.23}$$

which is the same form as Eq. 1.21. If we let the concentration $c = 1$ represent the state of the solution when all reactants have been consumed (only species B is present), $c = 0$ is the state of the solution when no reaction has occurred, and a is at maximum. In this

scenario, $b = c$, and $a = 1 - c$. The reaction rate term $F(c)$ of the IAA reaction can therefore be modeled using a single concentration variable c as

$$F(c) = k_c c^2 (1 - c), \qquad (1.24)$$

where c is bounded by $0 \leq c \leq 1$, with $c = 0$ is the concentration of unreacted solution, and $c = 1$ is the concentration of fully reacted solution. This reaction rate term is similar to the single variable cubic reaction term presented in Ref. [45]. For the IAA reaction, Eq. 1.24 can therefore be used as the reaction term $F(c)$ in Eq. 1.15, giving

$$\frac{\partial c}{\partial t} = D_c \nabla^2 c + k_c c^2 (1 - c) \qquad (1.25)$$

as the full reaction-diffusion equation for the IAA reaction. In the presence of fluid flow with velocity $\mathbf{u}$, the transport of the product species B (the autocatalyst) with concentration c is described by the advective reaction-diffusion equation

$$\frac{\partial c}{\partial t} + (\mathbf{u} \cdot \nabla)c = D_c \nabla^2 c + k_c c^2 (1 - c). \qquad (1.26)$$

This model for the IAA reaction is revisited in Section 5.1, where it will be used to help construct the autocatalytic plume simulation. Coupling of the IAA reaction front with fluid motion, using Eq. 1.26, is discussed in the following Section.

1.3.2 Autocatalytic reaction fronts and buoyancy driven flow

As the IAA reaction front travels, it leaves in its wake a product solution that is less dense than the reactant. Heat is produced during the reaction, as it is slightly exothermic. In addition, there is also an isothermal density change due to the difference in partial molal volumes of the reactant and product solutions. In a scenario where product solution is beneath reactant solution, these density changes create buoyancy driven flow.

Over the course of the last 30 years the interplay between buoyancy driven fluid flow and chemical reaction has enjoyed considerable theoretical and experimental attention. For the IAA reaction, it has been well-studied in thin tubes [46, 47], in thin slots [48, 49, 50, 51], and in the presence of a superposed flow [52, 53]. In all of these previous studies, convection effects were severely constrained by the viscous interaction with nearby solid boundaries. Our discovery of autocatalytic plumes resulted from our attempt to find

the reaction-driven flow phenomenology for a relatively *unbounded* solution. This was motivated in part by the rich behaviour already observed in thin tubes and slots. Here, the behaviour of the IAA front in these constraining geometries is reviewed.

In a sufficiently thin horizontal layer of solution, the change in the density between the reactant and product in the IAA system does little to aid in the transport of autocatalyst. However, deformation about the front does occur because of the density difference. Simulations in a covered layer of solution show that as the layer thickness is increased, so is the propagation speed and deformation of the front [54]. In simulations of uncovered solutions in contact with air, autocatalytic chemical fronts have been shown to induce capillary flows due to surface tension gradients across the front (Marangoni flows). Early experiments [34, 55, 56] on solutions in thin layers did not focus on the fluid dynamics involved with the front deformation, but instead investigated front speed of the reaction as a function of changes in solution acidity, and as a function of the ratio of the initial concentrations of arsenous acid and iodate.

The ratio of initial arsenous acid concentration to initial iodate concentration is defined as

$$R_{IAA} = \frac{[\text{H}_3\text{AsO}_3]_0}{[\text{IO}_3]_0}. \tag{1.27}$$

Experiments were performed in temperature controlled petri dishes in which negatively biased platinum electrodes at the center of the dish were used to initiate the reduction of iodate to iodide and thus initiate the front. It was found that the speed of fronts in the excess iodate regime ($R_{IAA} < 3$) and in the excess arsenous acid regime ($R_{IAA} \geq 3$) behave differently.

In the excess arsenous acid regime reaction front velocity was determined to be linearly dependent on concentrations of $[\text{IO}_3^-]$, $[\text{H}_3\text{AsO}_3]$, and $[\text{H}^+]$. In the excess iodate regime, plots of wave position as a function of time were found to be exponential, where the velocity is a linear function of distance. It was also found that in this regime the velocity increases at any particular distance with increasing $[\text{IO}_3^-]$, $[\text{H}_3\text{AsO}_3]$, or $[\text{H}^+]$. Simple reaction-diffusion models were used to explain the observed behaviour [34] and [55].

The IAA reaction is autocatalytic in both iodide and hydrogen ion. While the majority of experimental work done on the IAA reaction has used buffers to maintain the desired $[\text{H}^+]$ during the course of the reaction, there is one exception where it was studied in an unbuffered solution, allowing for an opportunity to investigate reaction-diffusion behaviour arising from two autocatalytic species [56]. It was found that for an initial *pH*

range of $3.5 < pH < 7.5$ the propagation velocity of the front is almost entirely insensitive to [H$^+$]. However, as pH is increased above 8.0, the front velocity depended highly on initial pH – it slowed as the pH was increased. This trend continued up to $pH = 9.6$, where above this value front propagation was not supported. For highly acidic initial conditions of $pH < 3.0$, velocities increased sharply as pH was decreased; at $pH < 1.9$ the reactant solution became too unstable to support front velocity measurements, as it was almost immediately converted to product. For the entire range of initial pH values, the pH of the product solution was always in the range $2.0 < pH < 3.0$.

An applied electric field can also change in the overall outcome of the IAA reaction [57, 58]. This phenomenon was investigated using reaction mixtures with various R_{IAA} values to test the electric field effects on net reaction stoichiometry. These experiments were performed in agar gel in order to prevent hydrodynamical flows in the reaction solution. The effect of starch concentration on front velocity in the IAA system was also investigated [58]. In previous experiments [34, 55, 59], it was assumed that the starch indicator played a passive role in the IAA system, influencing neither the reaction mechanism nor the front propagation velocity. It was found that as starch concentration was increased the front velocity slowed. In experiments involving the IAA front in a glycerol/water solvent in thin tubes, we found a similar result: as glycerol concentration is increased, the velocity of the front decreases. The results of these experiments are discussed in Section 3.1.2.

When a reaction front ascends along the entire length of a vertically oriented slot, the buoyancy-driven instability causes an initially flat front to break up into fingers [49, 50]. The shape of the fingers arises from the competition between convection, which acts to extend the fingers, and diffusion, which acts to smooth the front, and the finger spacing is determined by the width of the slot, and on the chemical reaction parameters [51]. Recently, experiments in vertically oriented slots with periodic non-uniform gaps matching the spacing of the fastest growing mode of the fingers have been shown to be able to amplify the pattern formation [60].

Theory explaining the pattern development in the vertical slot geometry has been well developed and agrees well with experimental observations [61, 62, 63, 64]. Linear stability analysis of a 2D flow model has shown the instability of a flat front. The theory predicts that the initial instability takes the form of a chain of convection rolls that turn the front into a series of rising fingers, and also that only low wave number perturbations will grow, damping out the higher wave numbers. The relative strength of the buoyancy

force in thin slots with thickness a can be described by a dimensionless parameter that comes from linear stability analysis [48, 65, 66] and is analogous to Ra_c

$$S = \frac{g'a^3}{\nu D_c} \tag{1.28}$$

where $g' = \delta g$ where $\delta = (\rho_u/\rho_r) - 1$ is the dimensionless density jump between the reacted and unreacted solutions. Ascending autocatalytic fronts in vertical slots are unstable to large-wavelength perturbations for all finite values of S [48]. Recently, numerical analysis of descending fronts in a vertical slot have been shown to be unstable with regard to buoyancy-driven convection [67, 45]. Even though the descending buoyant front is stably stratified, the difference between molecular and thermal diffusivities provides a mechanism that is able to initiate reaction driven convection around the front.

Eq. 1.28 can also be used to quantify the buoyancy contribution to front motion in vertically oriented thin tubes. In this case, a represents the tube radius, rather than the thickness of a slot. For descending fronts, no buoyancy-driven convection occurs since the fluid is bottom-heavy across the front. Ascending fronts, however, are top heavy across the front and free convection can result, provided that a critical value of S is reached. Linear stability calculations [47] using the dimensionless driving parameter S predict that planar ascending fronts are unstable to nonaxisymmetric convection for $S \geq 87.9$ and to axisymmetric convection for $S \geq 370.2$. Nonaxisymmetric convection is therefore predicted to appear at the onset of convection. The critical S values for the two convection modes have been verified experimentally [68, 69], and a sketch of their shape is shown in Fig. 1.2. Once convection is present, ascending reaction front velocity increases with an increase in S, while descent velocity for flat fronts is not affected by the driving parameter since convection does not occur.

Chemical composition also affects front velocity in thin vertically oriented tubes. In excess arsenous acid solutions, ascending and descending front velocities increase linearly as a function of initial iodate concentration [34]. In excess iodate solutions, descending front velocities are linear as a function of initial iodate concentration, however ascending velocities increase, but not with a directly proportional relationship to initial iodate concentration [69]. The velocity dependence on initial arsenous acid concentrations is linear for both ascending and descending fronts in either the excess iodate regime or the excess arsenous acid regime.

In this thesis, thin tube experiments were used to extract IAA front propagation
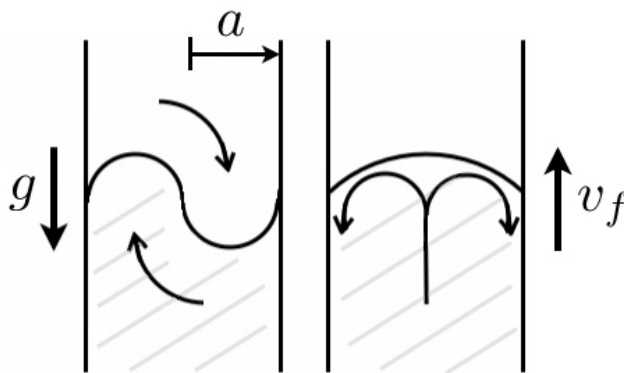
Figure 1.2: A sketch of the modes of convection for ascending buoyant reaction fronts with velocity v_f in thin tubes. Left: The nonaxisymmetric mode. Right: The axisymmetric mode. The direction of flow is indicated by the arrows, and product solution is shaded.

velocity for glycerol-water solvents used to make autocatalytic plumes. These measurements were necessary for analysis of autocatalytic plume behaviour, and the experimental results are discussed in Section 3.1.2. Thin tube simulations were used as a simple test of the parameters used for the autocatalytic plume simulations, and results from these tests are discussed in Section 5.3.

1.3.3 Spherical reaction fronts

In the absence of buoyancy-driven fluid flow, spherical autocatalytic reaction fronts have been studied theoretically and numerically. These studies are relevant to the initial conditions used for the simulation, discussed in Section 5.1.2. They are also relevant to the phenomenon of front death that we observed in our experimental system. Front death is mentioned as an experimental limitation in Section 3.1.3, and numerically it is investigated in detail in Section 5.5.1. Previous studies of spherical reaction fronts have focused on the existence and the stability of spherically symmetric solutions to the reaction-diffusion equations [70, 71], and on the effect of autocatalyst decay [72]. Threshold conditions needed to form spherical autocatalytic reaction front have also been calculated for both quadratic and cubic autocatalytic reaction fronts [73]. Autocatalytic reaction fronts under gravity are in some ways analogous to flame fronts [74, 75] where the feedback through temperature change in combustion systems is analogous to the feedback of autocatalyst in chemical reaction systems. In addition to being called "spherical reaction balls" [71], spherical autocatalytic reaction fronts have therefore also

been referred to as "isothermal flame balls" [70, 72].

Flame balls are steady, radially symmetric solutions of the reaction-diffusion-conduction equations for pre-mixed laminar flames. Originally proposed by Zel'dovich in 1944 [76], flame balls have since been observed when a spherical flame is formed during free fall [77, 78]. The combustive process which sustains flame balls is highly exothermic, and therefore free fall conditions are necessary to eliminate buoyancy driven flow. During flame ball experiments in microgravity, small local accelerations create gravitational like forces called "g-jitter". In the presence of these small, short lived gravity-like fluctuations, flame balls deform into "flame strings" [77, 78, 79], flame balls that have been stretched into a long, cylindrical shape.

In addition to being caused by undesirable gravity-like forces in microgravity experiments, the deformation of flame balls under gravity is particularly relevant to an explosion scenario for Type Ia supernovae [80]. The initial stages of the explosion scenario involves the formation of a "flame bubble" near the centre of a white dwarf, which is driven by buoyancy to the surface of the star. Simulations of flame bubbles in a gravitational field have investigated the mechanisms at play in the early stages of flame bubble evolution in a low viscosity fluid [80]. In Section 5.5.2 we discuss our simulations of flame balls in the same viscous parameters used to simulated autocatalytic plumes. The deformation of these flame balls from viscosity and buoyancy effects can produce behaviour similar to that of autocatalytic plumes.

1.4   Thesis overview

A survey of the plume literature shows an extensive variety of laminar and turbulent plumes. As a prelude to the discussion of autocatalytic plumes presented in later Chapters, in this thesis we first present an experimental investigation on the fundamental behaviour of compositionally-buoyant, forced laminar starting plumes. While a large variety of laminar plume head structures are known, as outlined in Section 1.1, the nature of transitions in the type of head that forms as experimental parameters are varied has not previously been systematically explored. Moreover, the conditions under which a stable laminar head changes its morphology have received little attention. Similarly, the scaling of the ascent velocity of forced buoyant plumes has not been previously studied. These issues are addressed in our experimental investigation of compositionally buoyant forced plumes, and are presented in Chapter 2.

A considerable amount of work has been done on the buoyancy-enhanced propagation of the IAA front in various geometries. In narrow tubes fronts take on a constant shape dictated by parameter S, and the study of the front is essentially reduced to a one-dimensional problem. In the limit of thin vertical slots and horizontal layers a convecting reaction front takes on an essentially two-dimensional pattern. In both of these scenarios, motion of the front is severely limited by the boundary of the reaction geometry. Naturally, this leads one to question how the IAA reaction front would behave in three dimensions, when the limitations on the flow imposed by the boundary are much less of a constraint. The results of our inquiry into this question is the central topic of this thesis: autocatalytic plumes.

Following the experimental study of forced starting plumes in Chapter 2, the subject of Chapter 3 is the experimental investigation of autocatalytic starting plumes produced by the iodate-arsenous acid reaction (IAA). Starting plumes produced by the IAA reaction have well-defined heads and conduits, much like the laminar starting plumes in non-reacting systems. However, unlike more conventional laminar starting plumes, reaction-driven flow in laminar autocatalytic plumes is much more complex. This complexity is highlighted by the pinch-off of the head from the conduit. This results in a free, reacting vortex ring and trailing conduit that produces a second generation plume head. We also performed numerical simulations of autocatalytic starting plumes. These simulations have extended our understanding of the rich dynamics of autocatalytic plumes, and are discussed in Chapter 5.

A closely related phenomena to autocatalytic starting plumes was also simulated; "autocatalytic flame balls". Like all other types of plumes, autocatalytic plumes remain attached to an isolated source which is at the base of a conduit. Autocatalytic flame balls, on the other hand, do not have a fixed location to which they attach. The same computational formulation was used to simulate both autocatalytic plumes and autocatalytic flame balls, with the only difference between the two being the set of initial conditions needed to simulate these closely related phenomena. Autocatalytic plumes are initiated at the bottom boundary of the spatial domain in which the simulation was performed, whereas autocatalytic flame balls were initiated as spheres of product solution far from any of the boundaries of the domain. Previous simulations of autocatalytic flame balls did not investigate the interplay between buoyancy-driven flow and reaction-diffusion. In Chapter 5, simulation results detailing the evolution of buoyant autocatalytic flame balls in a viscous solution are presented.

While autocatalytic starting plumes are the focus of Chapters 3 and 5, the steady conduits of autocatalytic plumes are the central topic of Chapter 4. As a control, and for comparison, non-reacting forced plume conduits were also examined. To probe the internal velocity structure of the plumes, a magnetic resonance imaging velocimetric technique known as the Gradient Echo Rapid Velocity and Acceleration Imaging Sequence (GERVAIS) [81] was used. This technique was employed to measure the axial velocity field at various locations along plume conduits.

The work detailed in this thesis provides an experimental and numerical investigation of a new type of plume that is produced by an autocatalytic chemical reaction. It has also helped to develop a deeper understanding of mechanisms involved with forced plume head morphology and velocity. The behaviour of autocatalytic plumes is unique when compared to other types of plumes, and where possible this is highlighted by comparison with parallel experiments on compositionally buoyant forced plumes throughout the thesis.

1.5 Contributions

Some of the results from this thesis are currently published in three papers [16, 17, 82]. Chapter 2 is an adaptation of Ref. [82]. Parts of Chapter 3 are adapted from Refs. [16, 17], and Chapter 4 is adapted from [17]. Two of these papers [16, 17] were co-authored by S. W. Morris, my Ph.D. supervisor. The other publication [17] has four authors, including myself. In addition to SWM, the other authors are Mick D. Mantle and Andrew J. Sederman, from the University of Cambridge. Co-authors MDM and AJS contribution to this work was to operate the nuclear magnetic resonance spectrometer used to acquire plume velocities and perform some of the data processing associated with these experiments, which are detailed in Chapter 4 and in Ref. [17]. In addition to these contributions, the source code for the numerical model of autocatalytic plumes detailed in Chapter 5 was written by A. Zebib from Rutgers University. The numerical model was formulated by AZ and A. De Wit, from the Université Libre de Bruxelles.

1.6 Dimensionless numbers

A summary of the dimensionless numbers used in this thesis and where they first appear is given in Table 1.1.

Dimensionless number	Name	Page introduced
$\mathrm{Re} = \frac{ud}{\nu}$	Reynolds number	6
$\mathrm{Ri} = \frac{g'd}{u^2}$	plume Richardson number	6
$\mathrm{Ra} = \frac{g\alpha L^3 \Delta T}{\nu \kappa}$	Rayleigh number	7
$\mathrm{Ra}_c = \frac{g\alpha L^3 \Delta c}{\nu D_c}$	concentration component Rayleigh number	8
$\mathrm{Ra}_T = \frac{g\alpha L^3 \Delta T}{\nu D_c}$	thermal component Rayleigh number	8
$\mathrm{Le} = \frac{\kappa}{D_c}$	Lewis number	8
$\mathrm{Sc} = \frac{\nu}{D_c}$	Schmidt number	8
$\mathrm{Pr} = \frac{\nu}{\kappa}$	Prandtl number	8
$R_{IAA} = \frac{[\mathrm{H_3AsO_3}]_0}{[\mathrm{IO_3}]_0}$	IAA reaction ratio	13
$S = \frac{g'a^3}{\nu D_c}$	convection mode parameter	15
$\mathrm{Re}_{hw} = \frac{uw_h}{\nu}$	head width Reynolds number	30
$\mathrm{Re}_{h\ell} = \frac{u\ell_h}{\nu}$	head length Reynolds number	30
$\mathrm{Ra}_p = \frac{g'd^4}{\nu LD}$	pipe Rayleigh number	65
$\sigma = \frac{\ell}{\Delta r}$	Resolution factor	87

Table 1.1: Dimensionless numbers used in this thesis. Variables used in the above equations are: u, velocity; d, pipe diameter; ν, kinematic viscosity; $g' = g(\rho/\rho_0 - 1)$ is the reduced gravity, where g is the gravitational acceleration and ρ_0 is the density of an object in a fluid with density ρ; α, thermal expansion coefficient; L_p, pipe length; T, temperature; κ, thermal diffusivity; D, molecular diffusivity; D_c, molecular diffusivity of catalyst; a, slot thickness; w_h, plume head width; ℓ_h, plume head length; ℓ, reaction length scale; Δr ; pixel spacing. Note that for compositional plumes $g' = g(\rho_a - \rho_i)/\rho_a$, where ρ_a is the ambient fluid density and ρ_i indicates injected fluid density. For autocatalytic chemical plumes, $g' = g(\rho_u - \rho_r)/\rho_u$, where ρ_u is the unreacted fluid density and ρ_i is the density of the reacted fluid.

Chapter 2

Compositionally Buoyant Starting Plumes

A starting plume or jet has a well-defined, evolving head that is driven through the surrounding quiescent fluid by a localized flux of either buoyancy or momentum, or both. We studied the scaling and morphology of starting plumes produced by a constant flux of buoyant fluid from a small, submerged outlet. The plumes were laminar and spanned a wide range of plume Richardson numbers Ri. Ri is the dimensionless ratio of the buoyancy forces to inertial effects, and thus our measurements crossed over the transition between buoyancy-driven plumes and momentum-driven jets. We found that the ascent velocity of the plume, nondimensionalized by Ri, exhibits a power law relationship with Re, the Reynolds number of the injected fluid in the outlet pipe. We also found that as the threshold between buoyancy-driven and momentum-driven flow was crossed, two distinct types of plume head morphologies exist: confined heads, produced in the Ri > 1 regime, and dispersed heads, which are found in the Ri < 1 regime. Head dispersal is caused by a breakdown of overturning motion in the head, and a local Kelvin-Helmholtz instability on the exterior of the plume.

Prior to the work presented in this Chapter, the nature of transitions in the type of plume head that forms as experimental parameters are varied has not been systematically explored. Moreover, the conditions under which a stable laminar head changes its morphology have received little attention. Similarly, the scaling of the ascent velocity of forced buoyant plumes has not been previously studied. In Section 2.1, the experimental apparatus and protocols are described, and in Section 2.2 results for the velocity scaling and head morphologies are presented. A brief summary of the experimental findings is

given in Section 2.3.

2.1 Experimental design

The apparatus used for our forced plume experiments was a plexiglass tank with a vertical glass capillary tube built into the centre of the tank floor. The inner diameter of the capillary tube, which served as the outlet for fluid injected into the tank, was 3.0 mm, and the inner dimensions of the square tank were 13.4 cm between walls that were 50.2 cm high. A second, smaller square tank was also used which had 9.8 cm between its inner walls and a height of 33.7 cm. A syringe pump was connected to the bottom end of the outlet pipe, allowing fluid to be injected at a controlled, steady rate. The syringe was filled with glycerol-water solutions slightly less dense than the ambient glycerol-water solution into which they were injected. Ambient solutions used in this experiment ranged from a 20% to an 80% volumetric ratio of glycerol/water. The densities ρ_a and ρ_i of the ambient and injected solutions were measured using an Anton-Paar densitometer. Density measurements were made at the temperature that had been recorded in the room during the respective experiments. The room temperature was measured to $\pm 0.5°$ C, implying a possible systematic error in the absolute densities ρ_a and ρ_i of less than ± 0.0003 g cm^{-3}. However, the difference in densities, $\Delta\rho = \rho_a - \rho_i$, is rather insensitive to the temperature, because of the very small difference in the thermal expansion coefficients of the two fluids. Since the ambient and injected fluids were nearly identical, the dimensionless ratio of their kinematic viscosities, ν_i/ν_a, was typically close to unity. The relevant dimensionless density difference $\Delta\rho/\rho_a$, along with other properties of the experimental fluids, are given in Table 2.1. Densities were measured with a densitometer at the same temperature at which a set of experimental runs were performed. Viscosities were interpolated from data given in Ref. [83].

Two methods of visualization were employed to observe the plumes. In the smaller of the two tanks, shadowgraphy was used. This technique requires a constant light source to be directed horizontally at the tank. By virtue of the difference in the refractive index of the injected and ambient fluids, the less dense (injected) fluid projects a dark image onto translucent white tracing paper attached to the tank at the opposite side to the light source. A digital CCD camera was used to capture the shadowgram images of the ascending plume. The sets of experiments for which shadowgraphy was used to observe plume behaviour are specified in Table 2.1 by set names beginning with "S". In the

Set	ρ_i (g/cm^3)	ρ_a (g/cm^3)	$\Delta\rho/\rho_a \times 10^2$	$\nu_i \times 10^{-6}$ (m^2/s)	$\nu_a \times 10^{-6}$ (m^2/s)	ν_i/ν_a
S1	1.0590	1.0599	0.0849	1.80	1.86	0.968
S2	1.1151	1.1166	0.134	3.95	4.17	0.947
D1	1.1745	1.1775	0.255	16.5	17.8	0.927
D2	1.1752	1.1797	0.381	16.5	19.1	0.864
D3	1.1897	1.1920	0.193	24.3	26.3	0.924
D4	1.2045	1.2160	0.946	40.7	66.2	0.615
D5	1.2135	1.2161	0.214	59.9	66.2	0.905

Table 2.1: Fluid properties of the various injected (subscript i) and ambient (subscript a) glycerol-water mixtures.

larger tank, blue dye was added to the injected fluid for visualization purposes. As fluid was being injected and a growing plume was formed, a digital CCD camera was used to capture images of its evolution. These experiments are given in Table 2.1 by set names beginning with "D". For both the dye and the shadowgraphy experiments, the injected flow rate Q was varied in the range of 3.3×10^{-2}mL/s to 6.67×10^{-1}mL/s. Altogether, 34 plumes were analyzed.

2.2   Results and discussion

2.2.1   Ascent velocity and scaling

After a short transient, plume heads ascend at a constant velocity. Linear fits of h values extracted from time lapse images were used to determine head velocities, v_h, as shown in Fig. 2.1. These fits excluded data in the immediate vicinity of the outlet, which was selected to be $h < 4$ cm. Typically, in the very early stages of plume head formation, the ascent of the head is slower than in the linear regime. In these stages, the head accelerates towards the constant velocity that it eventually achieves.

As is apparent from Fig. 2.1, for the D4 set of experimental runs, the ascent velocity of the plume head, v_h, increases with the injection flow rate Q. This trend is consistent for all data sets. To establish the scaling of v_h for all experimental runs, we applied dimensional analysis. We assumed that the flow in the system was dependent on five physical variables: v_h, d, ν_i, Q, and g'. Here, d is the diameter of the outlet tube, ν_i is the kinematic viscosity of the injected fluid, Q is the injected volume flux, and $g' = g\Delta\rho/\rho_a$ is the reduced gravity, where g is the acceleration due to gravity. Since
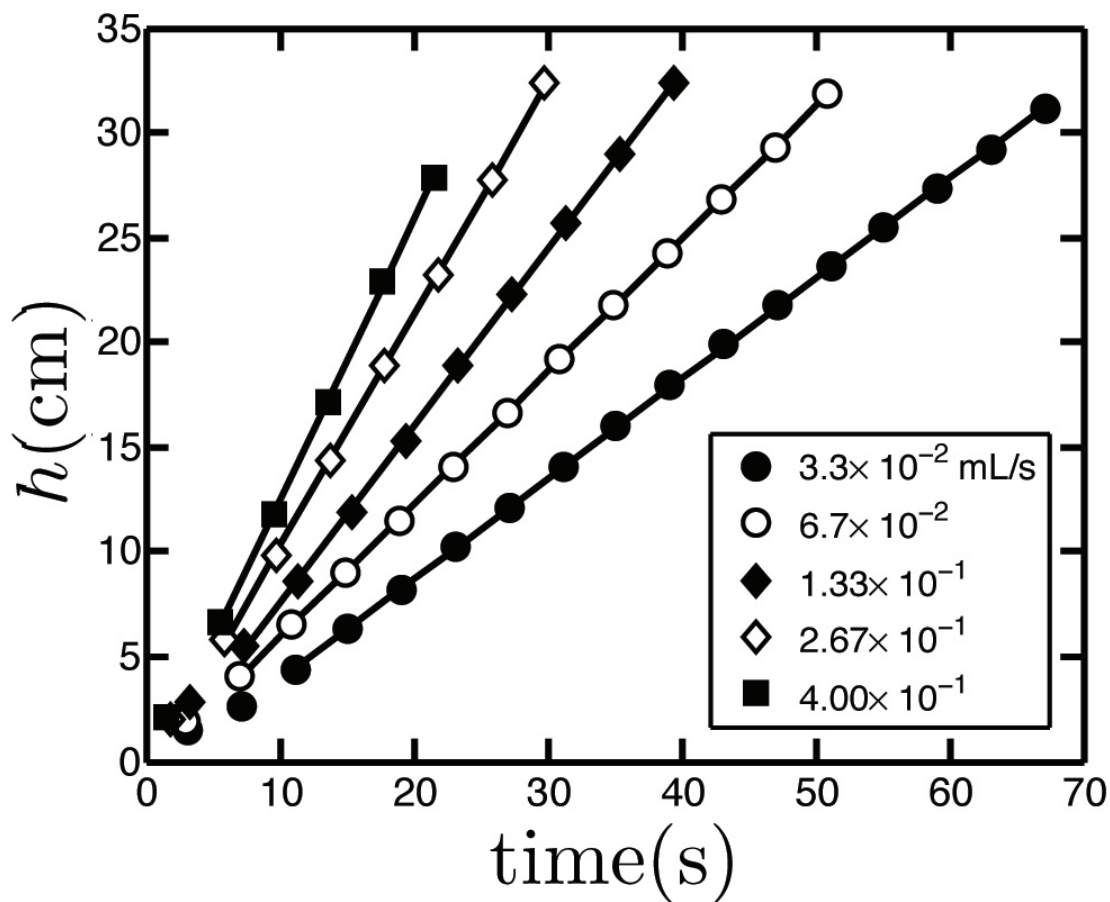
Figure 2.1: The vertical position of the plume head as a function of time for the D4 experimental runs at five injection flow rates. The solid lines show the linear best fit for plume heights above 4 cm. The slopes of these lines are the constant ascent velocity v_h of each plume.

there are five variables and three fundamental dimensions, a straightforward application of the Buckingham Π theorem [84] implies that two dimensionless groups describe the system. They are

$$\Pi_1 = \frac{v_h^2}{g'd} \quad \text{and} \quad \Pi_2 = \frac{Q_m}{\mu_i d} \; . \tag{2.1}$$

Π_1 is the inverse of the Richardson number, discussed below, and since $Q_m = Q\rho_i$ and $\mu_i = \rho_i \nu_i$, Π_2 can be written as

$$\Pi_2 = \frac{Q}{\nu_i d}. \tag{2.2}$$

Since $Q = Av_{avg}$, where A is the cross sectional area of the outlet pipe and v_{avg} is the average velocity of the fluid in the pipe, Π_2 can be further rewritten as

$$\Pi_2 = \frac{\pi}{4} \frac{v_{avg} d}{\nu_i}, \tag{2.3}$$

which is the standard expression for the Reynolds number, Re, multiplied by $\pi/4$. We can therefore recast the question of v_h dependence on Q as one that instead involves the relationship between two well-known dimensionless parameters, which are

$$\text{Ri} = \frac{g'd}{v_h^2} \quad \text{and} \quad \text{Re} = \frac{4}{\pi} \frac{Q}{\nu_i d} = \frac{v_{avg} d}{\nu_i}. \tag{2.4}$$

Here, Ri is the plume Richardson number, the ratio of the buoyancy forces driving the plume to the inertial terms in the Navier-Stokes equations. Re is the standard Reynolds number for the flow in the outlet pipe based on its diameter d and average flow velocity v_{avg}. We have $Q = Av_{avg}$ in a pipe with the cross sectional area $A = (\pi/4)d^2$.

Plotting Ri vs. Re on logarithmic axes, as shown in Fig. 2.2, we find that all the experimental data collapse on a single curve. The dependence is well described by a power-law that spans almost three decades in Re and more than two decades in Ri. Re covers a range from Re ~ 0.1 to Re ~ 100, and remains small enough so that the flow in the outlet pipe is never turbulent. The range of Ri straddles Ri ~ 1, so that we observe both flow regimes that are dominated by injected momentum (Ri $\ll 1$, for large Re), and plumes in which buoyancy forces dominate (Ri $\gg 1$, for small Re). The power law is of the form

$$\text{Ri} = a\,\text{Re}^k. \tag{2.5}$$

From a least squares fit of all of the experimental data on Fig. 2.2, it was determined that $a = 4.3 \pm 0.2$ and $k = -0.96 \pm 0.05$. Thus, we arrive empirically at the remarkably
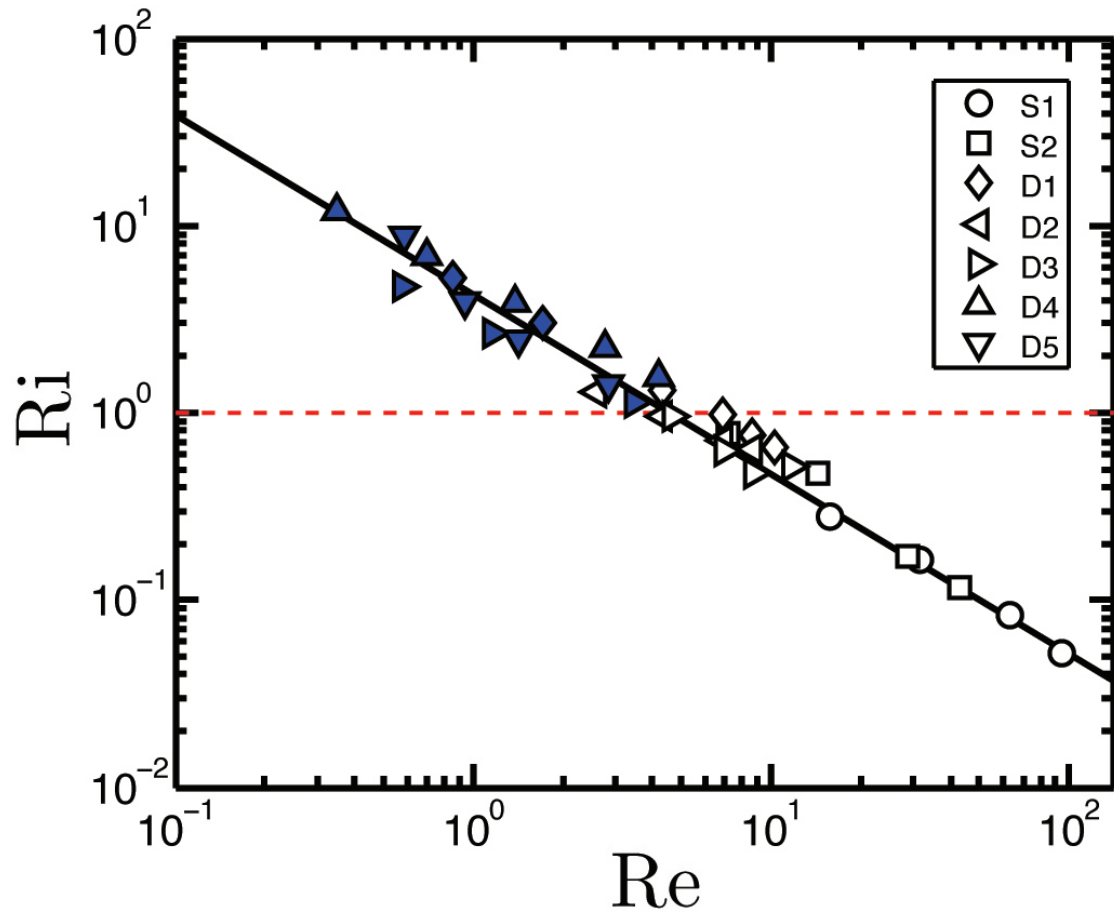
Figure 2.2: The dependence of the plume Richardson number on the Reynolds number of the injected fluid flow in the outlet pipe. The solid curve is a power law fit to the data, which gives $Ri = 4.3\,Re^{-0.96}$. The dashed red line indicates Ri=1. The symbol shading indicates the plume head morphology; shaded symbols indicate confined heads, while open symbols denote dispersed heads.

simple result that Ri is approximately proportional to Re^{-1}, or equivalently that Ri Re $=$ const. From Eqn. 2.4, this implies

$$\mathrm{Ri\ Re} = \frac{4}{\pi}\frac{g'Q}{v_h^2\nu_i} = 4.3 \pm 0.2 \ , \tag{2.6}$$

i.e. that all forced compositional plumes are described by a *single* dimensionless group that is independent of d, the diameter of the outlet pipe. Isolating v_h in eq. 3, we find

$$v_h = (0.54 \pm 0.01)\left(\frac{g'Q}{\nu_i}\right)^{1/2}. \tag{2.7}$$

The above expression for the head ascent velocity v_h may be regarded as a generalization for *forced compositional* plumes of the classic scaling proposed by Batchelor [3] for the velocity v_c of purely *thermal* plume conduits given by

$$v_c \propto \left(\frac{g\alpha P}{\nu\rho C_P}\right)^{1/2}. \tag{2.8}$$

Here, the thermal buoyancy flux $g\alpha P/\rho C_P$ replaces the densimetric compositional buoyancy flux $g'Q$ in Eqn. 2.7, where α is the thermal expansion coefficient, P is the power input by the heater, ν is the kinematic viscosity of the isoviscous solution, ρ is the density of the ambient solution, and C_P is the specific heat of the fluid. For the centreline velocity of a steady thermal plume, v_{cl}, the proportionality constant in Eqn. 2.8 is a known function of the Prandtl number [85],

$$v_{cl} = \left[\frac{1}{2\pi}\log\epsilon^{-2}\right]^{1/2}\left(\frac{g\alpha P}{\nu\rho C_P}\right)^{1/2}, \tag{2.9}$$

where ϵ is a solution of $\epsilon^4\log\epsilon^{-2} = \mathrm{Pr}^{-1}$. This result could presumably be generalized to the forced compositional case for which the Schmidt number Sc would replace Pr.

Experiments [28, 29] on thermal starting plumes in fluids with various Prandtl numbers found that the head rise velocity v_h was related to the conduit centerline velocity given in Eqn. 2.9 by

$$v_h = (0.57 \pm 0.02)v_{cl}. \tag{2.10}$$

Within error, the prefactor in Eqn. 2.10 is the same as the prefactor in Eqn. 2.7. The prefactor is less than one for the obvious reason that the growing plume head must be
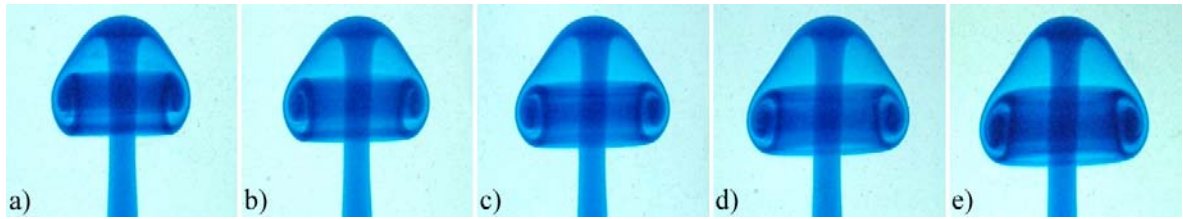
Figure 2.3: The nearly self-similar evolution of a typical confined plume head. Each image is 5s apart. The plume is from set D5 and the injection rate was $Q = 2.00 \times 10^{-1}$ mL/s. From the first to the last image in the sequence, h increases from 20.5 cm to 35.2 cm, and the size of the head increases from 1.9 cm× 2.3 cm ($\ell_h \times w_h$) to 2.4 cm× 3.1 cm.

supplied by a higher speed conduit.

The physical reason for the scaling of the ascent velocity in each case is clearly the fact that the morphology of the plume eventually becomes independent of conditions near the isolated source of buoyancy flux. In our case, this implies that v_h should become independent of the diameter of the outlet pipe d. Since d is the only length scale in the problem, only a single dimensionless group is required in the overall scaling of v_h, as in Eqn. 2.7.

2.2.2 Morphology of the plume head

The simplicity we found in the previous section for the scaling of the ascent velocity does not extend to the scaling of the plume head morphology. While the ascent velocity shows the same power-law scaling across a wide range of Re, the head morphology cannot be described by a single characteristic scaling over the same range. We found instead that there were two distinct types of plume head that exist on either side of Ri ≈ 1. For lack of an established taxonomy, we classify these head morphologies simply as *confined* for Ri > 1 and *dispersed* for Ri < 1. The distinguishing feature is the presence or absence of a stable vortex ring in the lobe of the plume head as it grows during its ascent. Confined heads, which are observed for larger Ri, exhibit such stable overturning structures, while for unconfined heads, observed for smaller Ri, the vortex ring exists for only a short time before it collapses and disperses. The domain of each type nicely meet at Ri ≈ 1, as indicated in Fig. 2.2, which forms a reasonably sharp boundary between the two morphologies. In addition to the stability and size of the vortex ring generated in the lobe, the two types of head have other distinguishing characteristics which are described below.
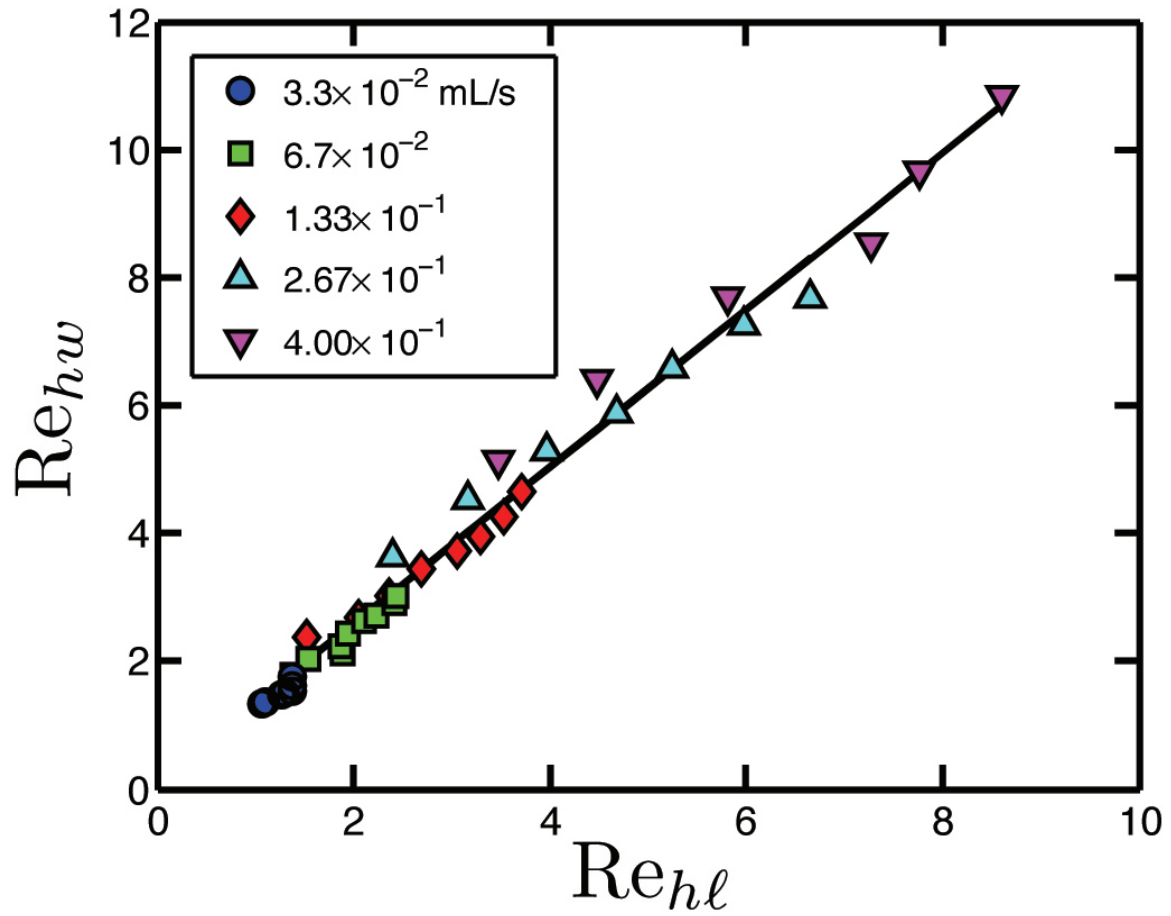
Figure 2.4: Head width as a function of head length for the D4 set of experiments. All of the plume heads in this set were confined. The head scales w_h and ℓ_h have been nondimensionalized as Reynolds numbers Re_{hw} and $\mathrm{Re}_{h\ell}$, respectively.
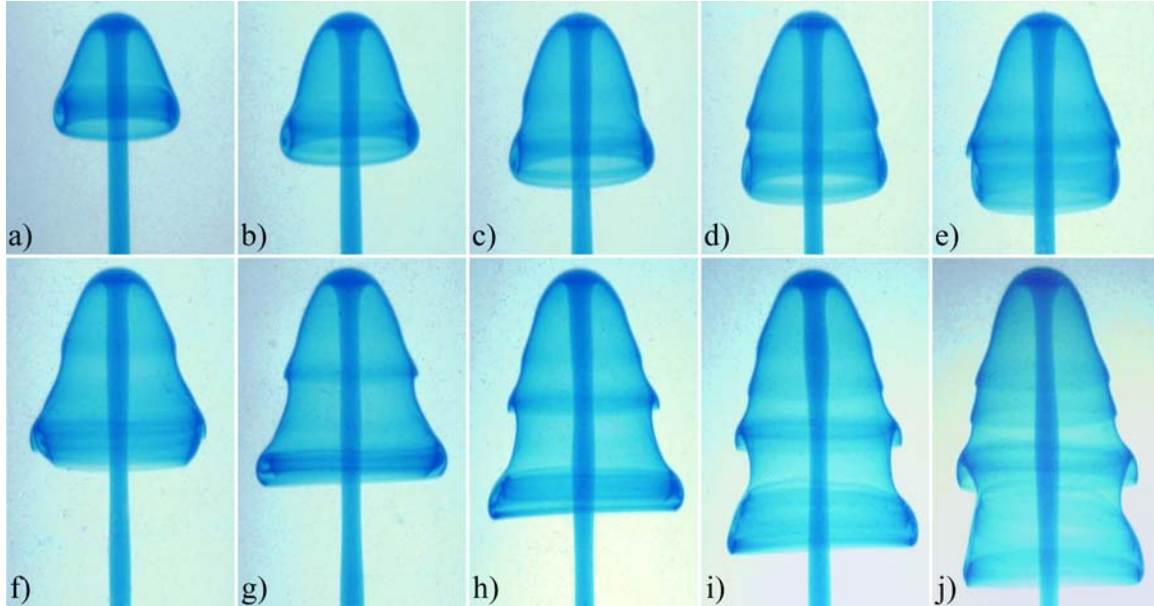
Figure 2.5: A sequence of images of a dispersed plume head during the evolution of a D2 starting plume with $Q = 2.67 \times 10^{-1}$ mL/s. Each image is 2s apart. From the first to the last image in the sequence, h increases from 10.4 cm to 31.0 cm. The dimensions of the plume head in a) are $l_h = 1.6$ cm and $w_h = 2.1$ cm.

A confined head is the classic mushroom-shaped laminar plume head. This type of head is shown in Fig. 1.1, and in a sequence of images in Fig. 2.3. We use the term "confined" to describe this type of head because the fluid that comprises it remains within a compact structure. This structure is preserved for the duration of the life of the starting plume, which ends when the head collides with the top of the tank. The fluid in the head circulates around an axisymmetric vortex ring that remains localized near the top of the plume. As shown in the sequence in Fig. 2.3, in order to accommodate the influx of new fluid delivered to the head through the conduit, over time, a confined plume head grows and its vortex ring increases in size. We studied the growth of the head by measuring the width of the head w_h, and the length of the head ℓ_h, as defined in Fig. 1.1, at various times. These two lengths were nondimensionalized by their associated Reynolds numbers,

$$\mathrm{Re}_{hw} = \frac{v_h w_h}{\nu_i} \quad \text{and} \quad \mathrm{Re}_{h\ell} = \frac{v_h \ell_h}{\nu_i}. \tag{2.11}$$

Figure 2.4 shows how the Re_{hw} scales with $\mathrm{Re}_{h\ell}$, for all of the confined D4 plumes. We find that Re_{hw} is simply proportional to $\mathrm{Re}_{h\ell}$, independent of Q. In all cases, $\mathrm{Re}_{hw} \sim$

C Re$_{h\ell}$, with $C = 1.24 \pm 0.04$, and hence the aspect ratio of the head is constant, with $w_h/\ell_h = 1.24 \pm 0.04$. This behaviour is typical for plume heads in the confined regime.

This simple scaling is not found in dispersed plume heads. The evolution of a dispersed head is shown in Fig. 2.5. In contrast to confined heads, dispersed heads do not remain compact and do not contain a stable vortex ring structure. Instead, the height of a dispersed head elongates faster than its width, as shown in Fig. 2.6 for D1 plumes. The head dimensions w_h and ℓ_h are only clearly defined in the early stages of growth, after which instabilities in the lobe take over, as shown in Fig. 2.5.

A vortex ring structure forms early in the evolution of a dispersed plume head, but subsequently becomes unstable by an interesting mechanism. The vortex in the lobe fails to draw in all of the fluid being delivered to it from the outer layer of the head. Instead, the flow diverges and some of the fluid is directed upward and eventually escapes the vortex ring. At the moment when this vortex entrainment breaks down, a *hammer* shaped structure, unique to dispersed heads, is observed. This structure is barely discernible in Fig. 2.5a,b, and is shown in detail in Fig. 2.7. At the site of the hammer structure, the plume head protrudes outwards, forming a bell shape. Above the protrusion, an instability, which looks like a Kelvin-Helmholtz instability, develops in the outer fluid layers, and the vortex ring becomes cut off from the influx of new fluid. Thereafter, the remnants of the vortex ring near the lobe dissipate, and an elongating fluid skirt that trails below the advancing head is formed. The evolving skirt exhibits further instabilities, while the overall flow remains axisymmetric, as seen in Fig. 2.5. A contributing factor to the development of these instabilities are small amplitude bulges of fluid that develop in the plume conduit. The bulges develop well above the outlet, and move upward at a higher velocity than v_h, causing fluctuations in the volume flux feeding the head. Bulges are visible in the portion of the conduit shown in Fig. 2.5 f-j.

The scenario for dispersed head evolution we have described above is typical of heads that form near Ri ≈ 1. For Ri $\ll 1$, the head forms Kelvin-Helmholtz like instabilities relatively quickly, before the hammer and bell shapes have time to develop. It should be noted that a Kelvin-Helmholtz instability will develop when the *local* shear reaches Ri $< 1/4$ [4], where the shear velocity and thickness of the shear layer are the important parameters. It is known from simulations [33] that below this critical value of Ri, Kelvin-Helmholtz instabilities appear in a starting plume head. The *global* Richardson number we have defined for the whole plume, Eqn. 2.4, is not identical to the *local* Richardson number that governs the Kelvin-Helmholtz instabilities of the plume head.
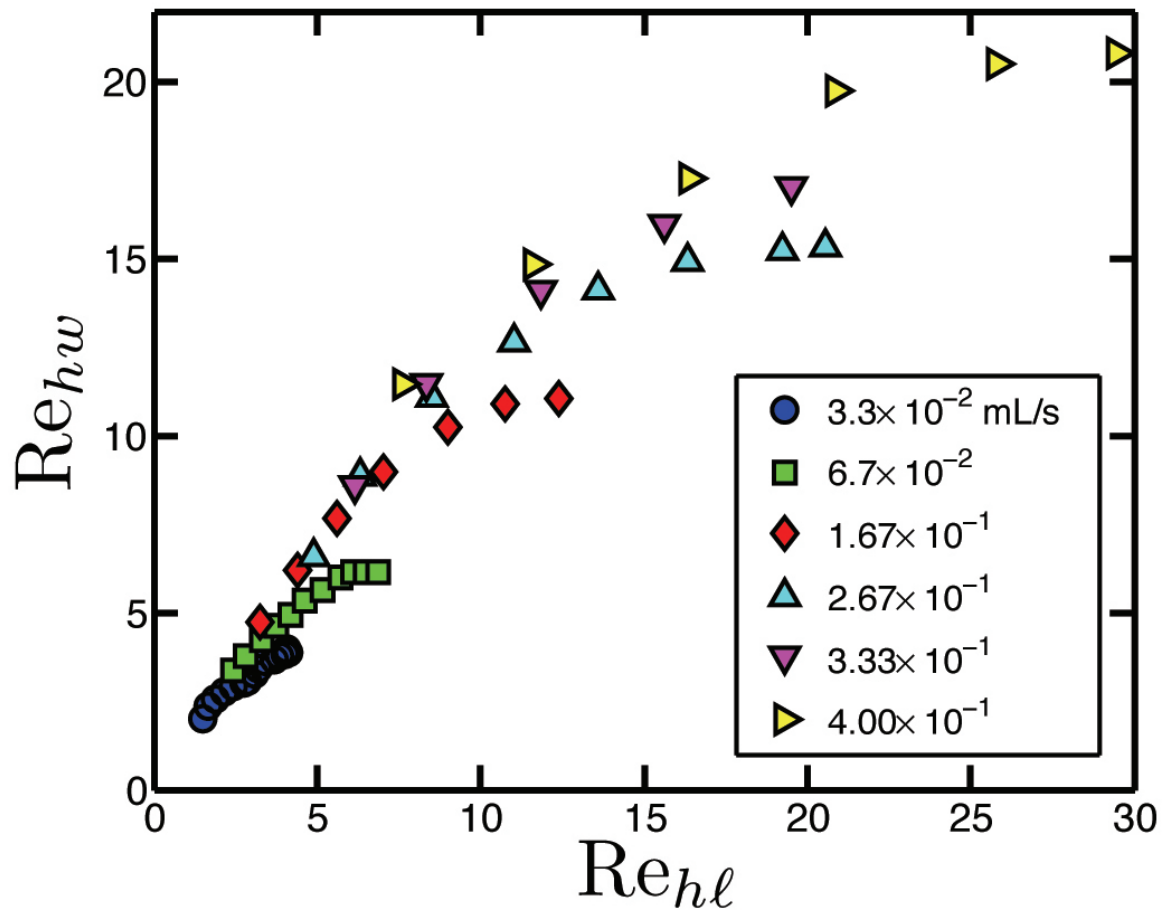
Figure 2.6: Head width as a function of head length for the D1 set of experiments, nondimensionalized as Reynolds numbers. With the exception of the plume with the lowest value of Q, all these plumes are dispersed. For all dispersed plumes, the head length grows faster than the width as the lobe becomes unstable.
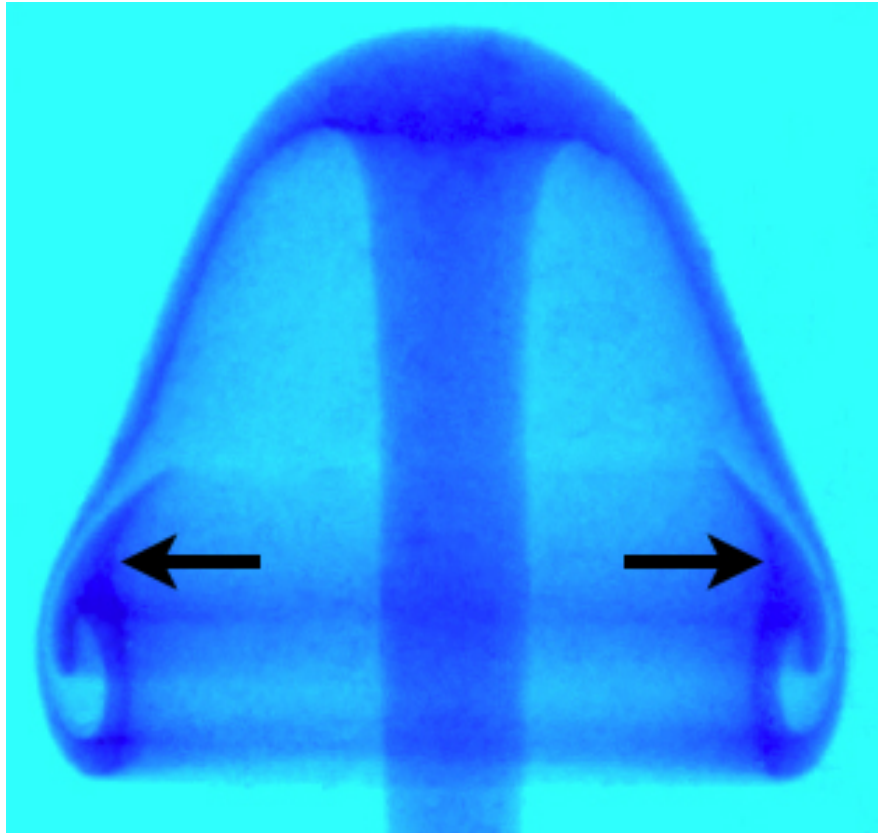
Figure 2.7: An image of the axisymmetric hammer-shaped structure (indicated by the arrows) that results from the onset of a divergent flow structure beneath the underbelly of the head. This structure is not observed in confined heads. The head is from a D3 plume with injection rate $Q = 6.67 \times 10^{-1}$ mL/s. The dimensions of the plume are $h = 21.9$ cm, $w_h = 3.7$ cm, and $\ell_h = 3.3$ cm.

2.3 Summary

In summary, we have experimentally explored the scaling and morphology of forced compositional plumes, which could also be called buoyant jets, in the laminar regime. We focused on starting plumes, for which a well-defined, ascending head exists. From dimensional analysis, we found that the system is described by the Richardson number of the plume and the Reynolds number of the injected buoyant fluid in the outlet pipe. We experimentally determined that the Richardson number, which scales with the inverse square of the head ascent velocity, had a simple power law relationship with the Reynolds number, which scales with the volumetric flux of the injected fluid. This scaling is exactly such that the diameter of the outlet pipe d drops out. This reflects the physical fact that the ascending compositional plume's morphology and speed eventually become independent of the details of the localized source of buoyancy and momentum that produced it. This result generalizes some previous observations and theory for thermal plumes to the case of forced compositional plumes. Our results are specific to the case of large Schmidt number and nearly isoviscous plumes.

The morphology of the advancing plume head exhibits two clear forms, depending on the Richardson number. For large Richardson numbers, we observe confined plume heads which contain a stable vortex ring and retain their mushroom shape throughout their evolution. These plume heads show a simple self-similar scaling. For small Richardson numbers, the plume heads become unconfined when the flow feeding the vortex ring fails to close and a thin, trailing skirt is formed. This skirt undergoes subsequent local instabilities that appear to be of the Kelvin-Helmholtz type.

It would be interesting to extend this study to the case of forced plumes with both thermal and compositional effects, to non-isoviscous cases and to forced plumes ascending in a density stratified medium.

Chapter 3

Autocatalytic Chemical Starting Plumes

As we have shown in Chapter 2, buoyant starting plumes may develop well-defined mushroom shaped heads. In conventional starting plumes, overturning flow in the head entrains less buoyant fluid from the surroundings as the head rises, robbing the plume of its driving force. We consider here a new type of plume in which the source of buoyancy is an autocatalytic chemical reaction. The reaction occurs at a sharp front which separates reactants from less dense products. In this type of autocatalytic plume, entrainment assists the reaction, producing new buoyancy which fuels an accelerating plume head. In some cases, as the plume evolves, the head detaches from the upwelling conduit, forming an accelerating, buoyant vortex ring. A second-generation head then develops at the point of detachment. Multiple generations of autocatalytic vortex rings can detach from a single triggering event.

This Chapter is organized as follows. In Section 3.1 we will discuss the details of the fluids and apparatus used for our experiments. Section 3.2 gives a comprehensive account of the behaviour of autocatalytic chemical starting plumes. This will be followed by the development of two simple models of autocatalytic chemical plumes in 3.3, and then a summary in Section 3.4.

3.1 Experimental design

3.1.1 Reactant preparation and fluid properties

Reactant solutions were prepared using reagent grade chemicals and distilled water. In addition, most reactant solutions also contained glycerol, the purpose of which was to adjust the viscosity of the reactant mixture. Solutions with as much as 50% by volume glycerol were used, and properties of these solutions are given in table 3.1. Densities were measured with a densitometer, viscosities were interpolated from data given in Ref. [83]. Values for the diffusion constant were calculated by using the known iodate diffusion constant in water [34] and using the Stokes-Einstein relation [86]. Unless otherwise stated, the percentage of glycerol in solution refers to the volume percent, rather than the mass percent. Iodate stock solutions were prepared by dissolving KIO_3 powder in distilled water. Arsenous acid stock solutions were prepared by dissolving As_2O_3 powder in hot, stirred water. These stock solutions were diluted so that the working solution contained $[IO_3^-]$=0.005M and $[As(III)]$=0.020M. Given that $[As(III)]_0/[IO_3^-]_0 = 4$, the reaction mechanism is described by Eq. 1.19. These concentrations were not varied in the experiments we report here. Congo Red indicator was used to visualize the reaction fronts. It was present in solution at a concentration of 2×10^{-5}M. Congo Red has a pH range of 3.0 to 5.0, where the acid form is blue and the base form is red. The reaction front leaves in its wake a product solution with pH of ~ 2.7, so that the upwelling blue products are easily visible within the red unreacted solution. The solution temperature was constant at $24.0 \pm 1.0°$ C.

The IAA reaction can be initiated locally at the negatively biased part of a platinum electrode. This method, however, was not used for the autocatalytic plume experiments. When a voltage was applied across an electrode in IAA solution, it triggered a reaction front and also introduced heat and bubbles into the solution. Since we required that the reactant solution remain quiescent during front initiation, we did not use this method to initiate a front. We therefore settled on another method for initiating the reaction front; the injection of a small amount product solution into the solution via syringe. The product solution was typically produced on a petri dish by adding a drop of hydrochloric acid to leftover reactant solution prepared for an experimental run. The initiation of the front in the autocatalytic plume apparatus is discussed further in Section 3.1.3.

$\%_V$	$\%_M$	ρ_u (g/cm^3)	$\nu_u \times 10^{-6}$ (m^2/s)	$D_c \times 10^{-9}$ (m^2/s)
0	0	0.99745	0.91	2.0
10	12.7	1.02787	1.25	1.4
20	24.6	1.05784	1.75	0.98
25	30.0	1.06936	2.07	0.82
30	35.8	1.08705	2.52	0.66
40	46.3	1.11483	3.86	0.42
50	56.3	1.14046	6.37	0.25

Table 3.1: Fluid properties of the reactant fluids for various glycerol-water concentrations at 24.0°C.

3.1.2   Reaction front velocities

To our knowledge, the IAA reaction has not been studied in a glycerol-water mixture before. To acquire basic information about the effect of glycerol concentration on propagation of the reaction front, we studied the ascent and descent of the IAA reaction front in a vertically oriented capillary tube. In a thin tube, descending fronts are hydrodynamically stable, and therefore propagate by reaction-diffusion only, thereby allowing for the velocity of the front to be measured independent of buoyancy effects.

All capillary tube experiments were performed inside a fluid jacket with a constant temperature of 25.0±0.1°C. The jacketed capillary tube apparatus was constructed by drilling two holes in each of two rubber stoppers; one hole in the center to hold the capillary tube and the other hole through which a small pipe was fitted. The piping was used to connect the apparatus to a Neslab RTE-111 fluid bath capable of controlling the temperature of the fluid in the jacket to the nearest tenth of a degree. The apparatus was connected to a sturdy frame attached to an optical table and held in a vertical position.

The capillary tube used for this experiment has an inner diameter of 3.0 mm. The tube diameter was determined by finding the difference between the weight of the tubes with water in them and without. The diameter could then be calculated using the density of water at room temperature. The reaction fronts were initiated at the bottom of the capillary tube. Between each run the capillary tube was flushed with distilled water and then with reactant solution before it was refilled. Front speeds were determined by tracking the position of the front as it propagated. This was done by viewing the front through a cathetometer that moves vertically on an attached Vernier scale. The position of the front at specific times was recorded to the nearest second over intervals of 5-10

minutes for at least an hour. Once the ascending motion was tracked, the tube was turned upside down in order to track descending front motion. Front velocity, v_f, was constant for all experimental runs, and was calculated from the slope of the position-time data.

The shape of descending fronts were always flat across the diameter of the capillary tube. Front motion in this case is purely an effect of reaction-diffusion. This is in contrast to the majority of ascending fronts observed, where the front shape was a convex curve spanning the diameter of the tube. The curvature of the front is due to the reaction-diffusion-convection nature of the front [46, 87]. As shown in Fig. 3.1, which shows the velocities of the fronts as a function of glycerol concentration, the velocities of the ascending fronts above concentrations of 40% glycerol were effectively the same as the velocities of the descending fronts. In these cases, no convection aided in the transport of product fluid, and these ascending fronts were also flat.

Velocities of descending pure reaction-diffusion fronts decrease linearly with the percentage of glycerol present in the solution. The decrease is due to the effect that increased viscosity has on the speed with which the catalyst molecules diffuse. This effect is shown by the decreasing values of the molecular diffusion constant with glycerol concentration shown in Table 3.1. The velocity of ascending fronts, however, has a more complicated dependence on glycerol concentration. The difference between the ascending and descending front velocities for any given concentration is at its maximum for the 10% glycerol solution, which is slightly larger than the difference measured for solution free of glycerol. Beyond 10% glycerol, the difference between ascending and descending front velocities decreases steadily towards zero. Clearly, as the viscosity of the solution increases, the effects of convection are increasingly quenched, up to the point where they disappear entirely for the 40% solution. The parameters involved with quenching of convection for ascending reaction fronts in capillary tubes has been found to depend on the dimensionless parameter S defined in Eq. 1.28 [47, 87].

The front velocity data from this Section is used in Sections 3.3 and 4.2.2 to construct simple models of autocatalytic starting plumes, and steady plumes, respectively. It is also used to calculate parameters used for our simulation of autocatalytic plumes, which is the subject of Chapter 5.
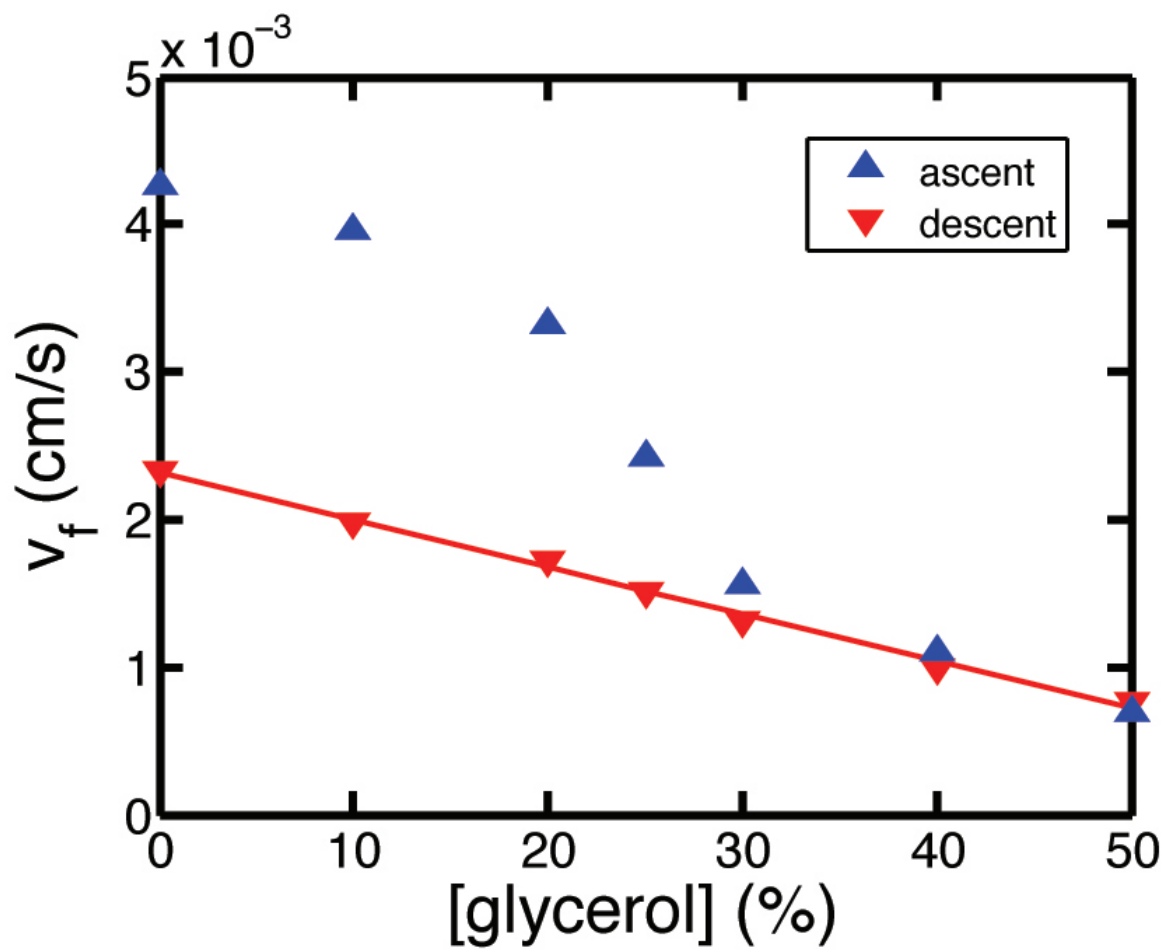
Figure 3.1: The velocity of ascent and descent for the IAA front in solutions with various concentrations of glycerol (by volume percentage).

3.1.3   Starting plume apparatus

The apparatus used for producing IAA starting plumes is shown in Fig. 3.2. The reaction tank was a large glass cylinder sealed at each end by large rubber stoppers. A capillary tube entered through a hole in the lower stopper. The outside end of the capillary tube was sealed with a short plastic tube clamped at one end which formed the initiation volume. The plastic tube was filled by a porous plug made of loosely packed cotton. Reactions were initiated by inserting a thin hypodermic needle into the plastic tube and then injecting a very small amount of product solution into the porous plug. The plug served to quench any hydrodynamic disturbance of the reactant solution during reaction initiation. As it ascends, a reaction front first must make its way through the plug, and then into the capillary tube. Upon reaching the end of the submerged portion of the capillary tube, a front is then able to escape into the larger tank, initiating a plume. The apparatus was illuminated from behind and still images of the evolving front were captured using a digital camera.

When the front was released from a very narrow capillary tube with diameter 0.9 mm into the larger tank, we found that the front did not propagate. This "front death" phenomenon is due to the requirement of a minimum critical concentration of autocatalyst near the initiation region, which therefore cannot be too small. Such a threshold effect is predicted [73, 70] for cubic autocatalysis in three dimensions. A similar scenario called the Allee effect is observed in population dynamics [88], where plant and animal species suffer a decrease in their per capita rate of increase when their population density is not above a critical threshold. To our knowledge, front death has not been experimentally investigated for the IAA reaction. This constraint was easily overcome by using a large enough capillary tube to launch the reaction into the large tank. A diameter of 2.7 mm proved to be sufficient.

3.2   Results and discussion

3.2.1   Starting plume characteristics

The various stages in the evolution of a free autocatalytic plume are shown in Fig. 3.3, which shows an experimental run in 40% glycerol solution. Initially, the plume rises out of the capillary tube and its head remains roughly spherical. This stage of growth is shown in Fig. 3.3a. In this initial stage, there is essentially no entrainment of reactant
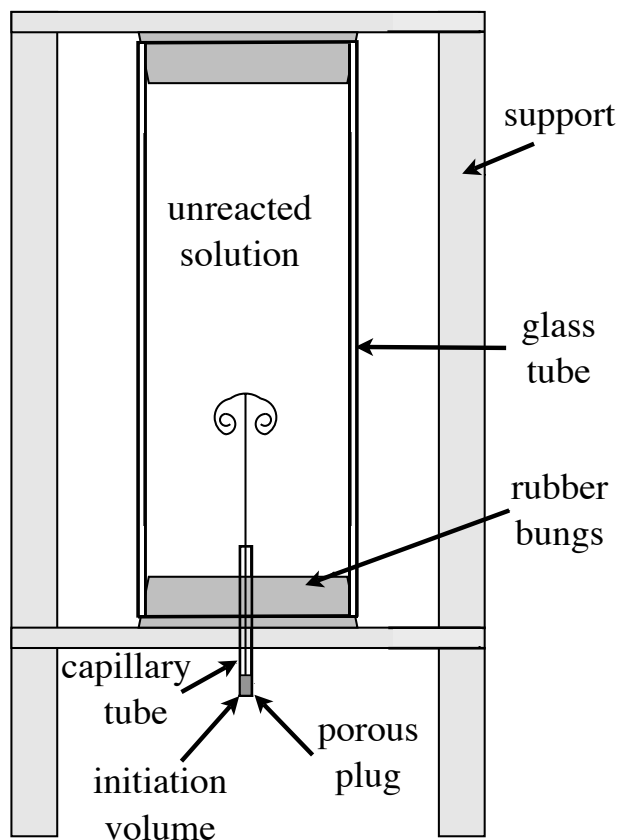
Figure 3.2: A schematic of the apparatus. The main volume is a cylinder 32 cm long with an inner diameter of 8.9 cm. The capillary tube has an inner diameter of 2.7 mm.

solution into the plume head, which grows slowly. In this stage, the head grows primarily from product fluid entering the head from the upwelling conduit. Later, vortical motion in the head leading to entrainment of unreacted fluid sets in. Fig. 3.3b shows a plume head well past the onset of entrainment. This shows the familiar mushroom-shaped head for a plume in which the surrounding fluid is being drawn into the head by a single overturning vortex ring.

As the entraining autocatalytic plume continues to ascend and enlarge, the plume head begins to pinch-off from the upwelling conduit. The pinch creates a bottleneck in the conduit which swells as it fills with rising product solution. During the swelling below the bottleneck, what was formerly the head of a starting plume becomes an essentially free vortex ring. As shown in Fig. 3.3c, the vortex ring detaches from the conduit, and is eventually connected only by a very thin filament of product solution. The swelling
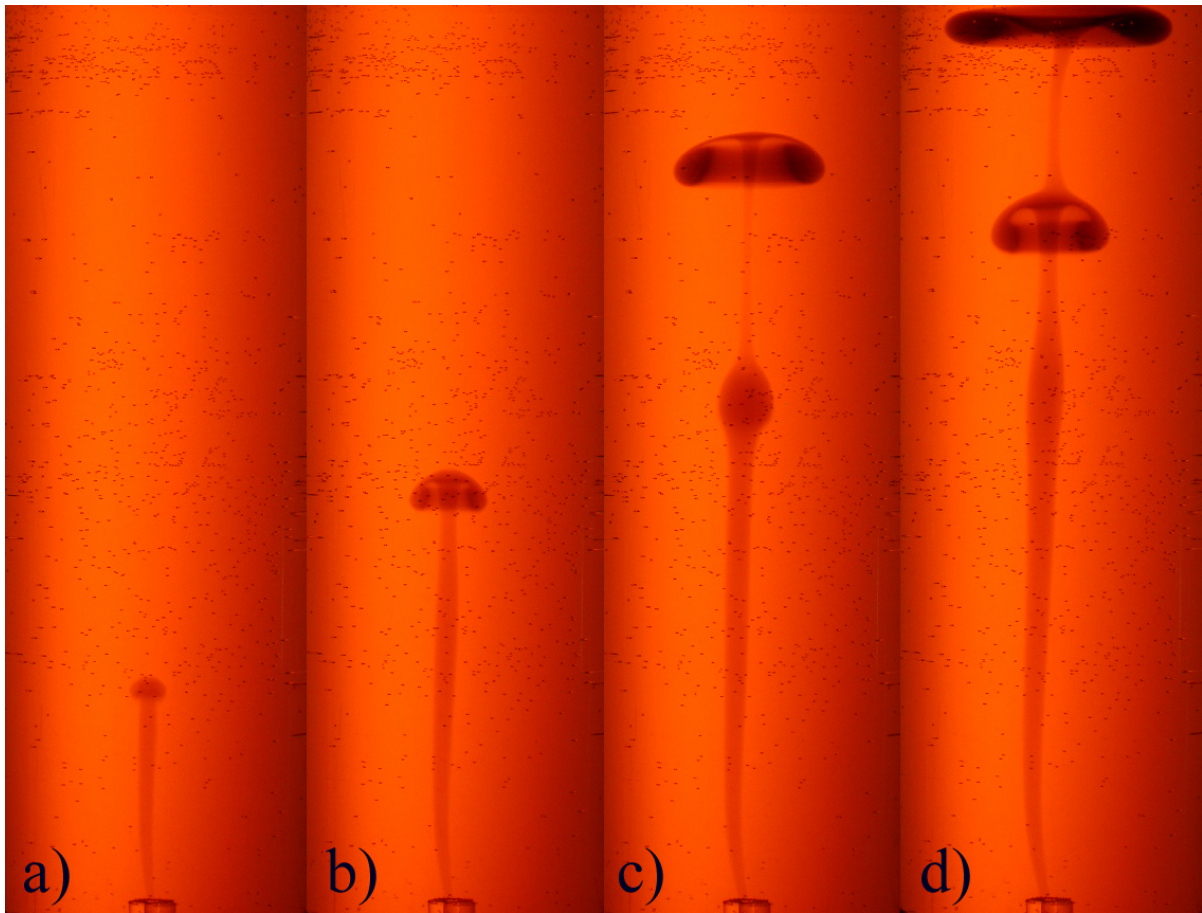
Figure 3.3: A sequence of images showing the evolution of the plume structure. (a) 202 s, (b) 328 s, (c) 458 s and (d) 554 s after exiting the capillary tube.

in the conduit develops into a new, second generation plume head. In Fig. 3.3d, a new pinch-off process has started again below the second generation plume head. Yet another bottleneck is formed when the second generation head pinches-off and becomes a vortex ring. The new bottleneck swells and the process is repeated. In the plume apparatus discussed in Section 3.1.3, we have observed as many as four generations of pinch-off and subsequent vortex ring formation in autocatalytic plumes. The fourth generation plume head eventually reaches the top boundary of the reaction vessel, closing the possibility of further pinch-off. Some experiments were performed in a cylinder longer than in the standard apparatus, and these will be discussed further in Section 3.2.3.

From the digital images of plume evolution, we determined the height and width of the ascending buoyant plume as a function of time. Height was measured from the top of the front to where it exited the capillary tube, and the width refers to the maximum width across the head or free vortex ring. In this Section, only the first generation head and vortex ring are considered in the analysis. A discussion of subsequent generation plume heads will be presented separately in Section 3.2.3. Typical width and height data for first generation head formation of an autocatalytic plume is shown in Fig. 3.4. This data is from the 40% glycerol plume shown in Fig. 3.3. Fig. 3.4a shows that the width of the plume goes through three distinct regions of approximately linear growth. The initial, and slowest, growth rate occurs in the initial stages of head development, when there is no obvious entrainment into the plume head maintains a roughly spherical shape. A transition to a second, increased growth regime occurs once a vortex ring develops in the head. The vortical motion entrains surrounding reactant solution into the head, which in turn reacts and increases the head buoyancy. Finally, the third and fastest growth regime occurs when the plume head detaches and becomes a thermal. Fig. 3.4b shows that the head accelerates during its ascent. The acceleration of the plume head continues after it has pinched-off, even though it is almost entirely disconnected from the conduit. The acceleration continues until the plume head, which is now a free thermal in the form of a vortex ring, reaches a maximum velocity. Boundary effects then cause it to decelerate as it nears the top of the tank.

The free vortex ring reaches a maximum velocity because of spatial limitations on its growth. As the ring widens, the cylindrical wall of the tank constrains head growth. Relative to past experiments involving IAA reaction-driven flow in thin cells and thin tubes, the wall boundary in the reaction vessel has much less influence on the flow. However, it should be noted that the IAA autocatalytic plumes we have produced are
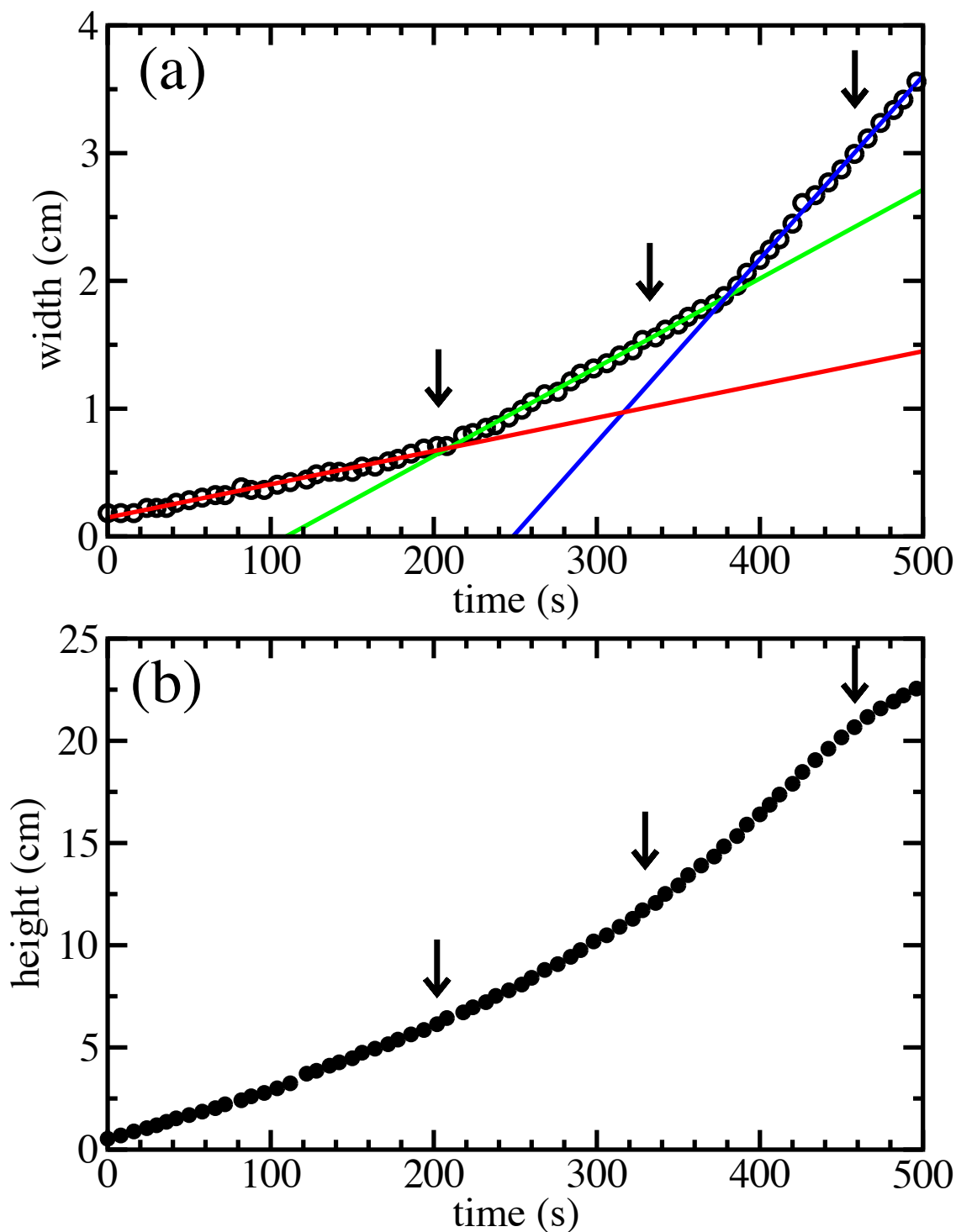
Figure 3.4: The growth of the plume as a function of time, up to the completion of the first pinch-off, showing (a) the width of the head, and (b) its height. Colored lines in (a) show the nearly linear evolution of the width in the three regimes indicated. Vertical arrows indicate the positions of images (a), (b) and (c) from the previous figure.

by no means free of wall effects. Wall effects on flowing bodies have been extensively analyzed in the literature regarding the problem of calculating the drag coefficient for flow around a sphere at low Reynolds number. The rich history of this problem is reviewed in Ref. [89]. In experimental efforts to measure the drag coefficient, it has been noted that finite geometries cause the most significant experimental errors [90, 91, 92]. For the error to be less than 2%, it has been noted that the experimental tank must have a diameter more than 100 times the sphere diameter [91], and it has been estimated that a ratio of 50 between the inner diameter of the tank and the sphere will result in a 4% change in drag force [92]. In one set of experiments, it took a container diameter of over 700 times the sphere diameter to reduce the experimental error to better than 2% [90]. In the autocatalytic plume experiments detailed in this Chapter, the ratio of the inner diameter of the cylindrical container to the width of the plume head ranges from ~ 30 for small heads to as low as ~ 2 when the plume head or free vortex ring is well developed.

Given the finite dimensions of the plume apparatus, viscous interaction with the walls is present even in the earliest stages of plume growth. However, wall effects are increasingly a factor in the motion of the plume head as its width increases to values closer to the diameter of the cylinder. As the ring reaches such values, vortical motion in the head quenches because of the restriction on flow imposed by the wall. This constraint causes the vortex ring to decelerate after it reaches a maximum velocity. As vortical motion becomes constrained by the wall boundary, it is no longer able to effectively entrain fresh reactant solution. Therefore, because of wall effects, the role that vortex motion plays in buoyancy enhancement of the thermal significantly decreases. Further experiments in different diameter containers could elucidate how the influence of wall effects can alter vortex motion in the plume head.

In addition to wall effects, free surface effects also decrease the velocity of the thermal close to the top of the tank. While the apparatus is closed on the top, the top of the fluid is still exposed to some air inside the container. Since glycerol is highly hygroscopic, it will absorb moisture from the air, which will slightly decrease the density of a layer of reactant fluid at the top of the tank.

Another feature of autocatalytic plume head morphology is the spherical shape of the top of the head, which we refer to as the head *crest*. This characteristic is shown in Fig. 3.5, which shows an image of a 40% plume head along with a circle fitted to data points indicating the crest shape. The shape data for the crest was extracted by using edge detection analysis of plume head images, and then fitting a circle to this data to
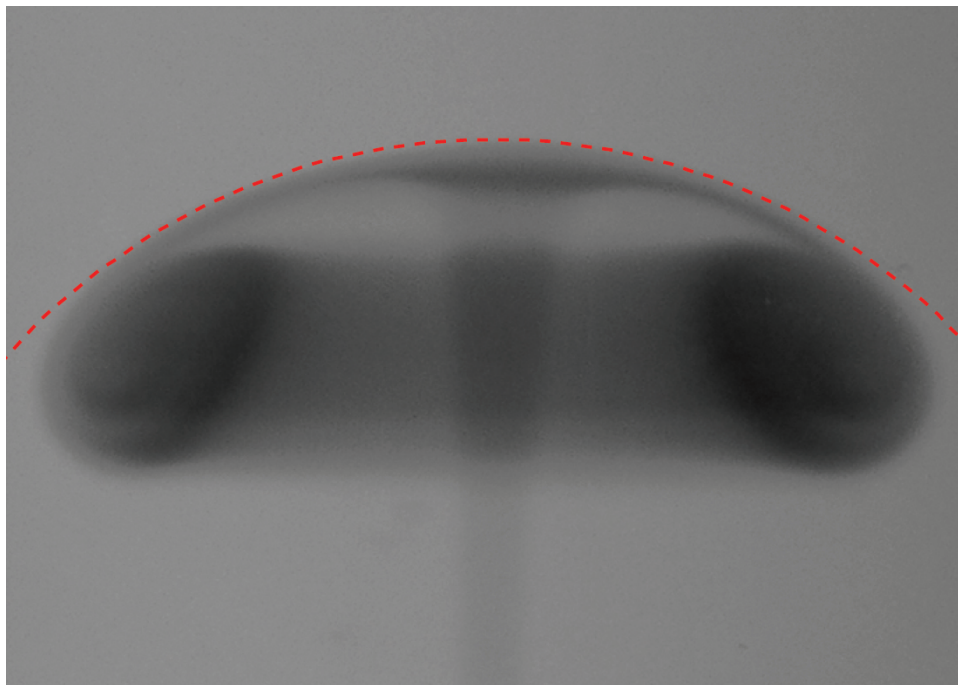
Figure 3.5: An image of an autocatalytic plume head and the circle fit (the red dashed curve) of its crest. The head was captured at a height of 16.7 cm above the outlet, 448 s after the front emerged from the outlet.

extract the radius of curvature, R_c. This procedure is similar to the method employed in a classic study by G. I. Taylor of the shape of bubbles rising in a cylinder [93]. The growth of R_c over time for the plume head displayed in Fig. 3.5 is shown in Fig. 3.6, which shows that R_c goes through two distinct periods of linear growth. This is in contrast to the previously discussed growth in head width, which has three distinct growth rates. While the transition from a small head without vortical motion to one with a vortex ring marks a change in growth rate of the width, it does not cause a change in the growth rate of R_c. Instead, the only transition observed in the growth of crest curvature is when the head pinches-off from the conduit. This transition coincides with the second growth rate change in width.

The same method used to calculate the spherical shape of the top of autocatalytic plume heads was also used to test whether or not the confined forced plume heads discussed in Chapter 2 have spherical crests. In the very early stages of confined head growth that occur while a vortex ring is forming in the head, the crest images fit a circle well, indicating that the crests are spherical. However, as the flow of buoyant fluid in the head underturns and forms a vortex ring, the plume heads assume the shape shown
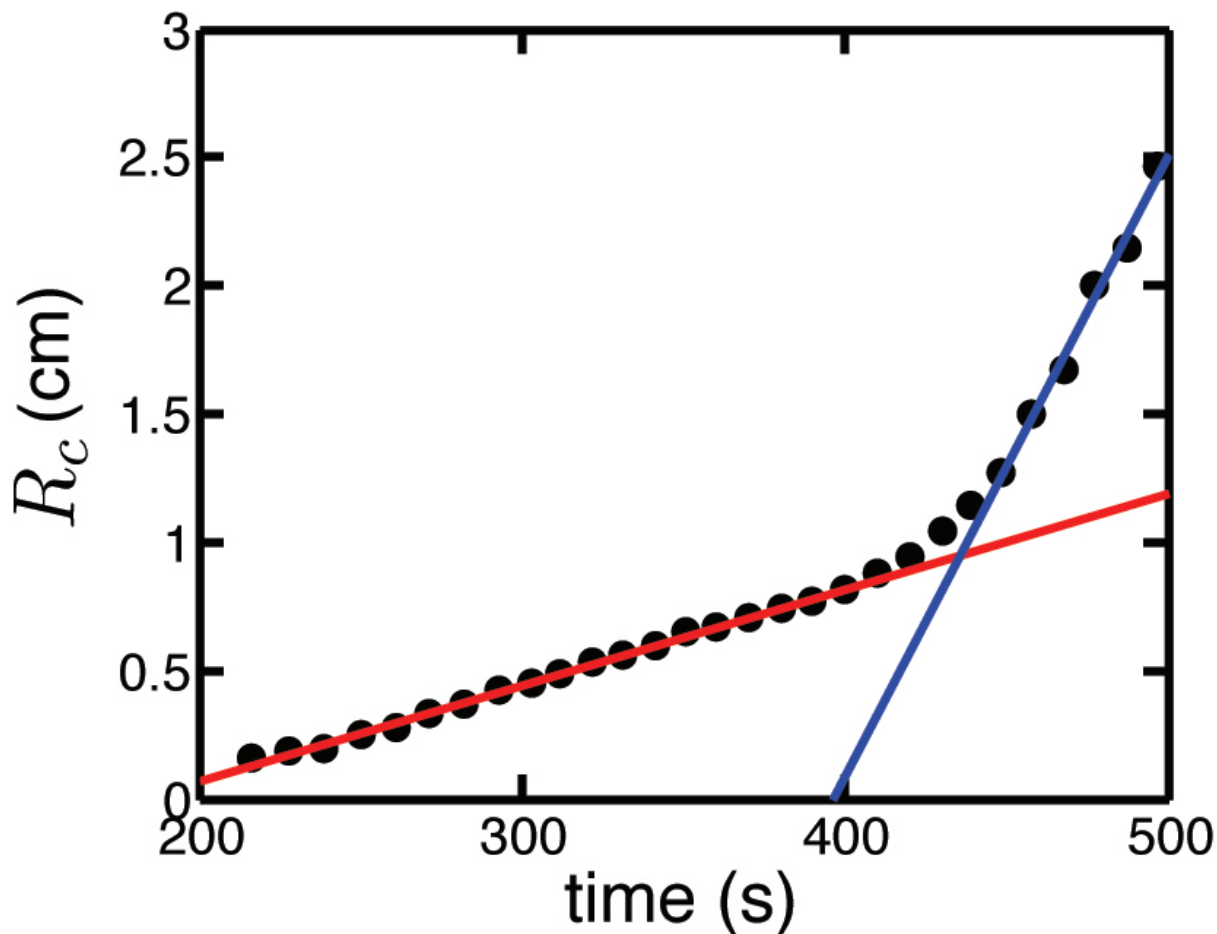
Figure 3.6: The radius of curvature as a function of time for the crest of an autocatalytic chemical plume head. The red line is the line of best fit for head curvature measurements prior to pinch-off, the blue line is fit to curvature data following pinch-off.

in Fig 2.3, in which the top of the heads deviate from a spherical form. As discussed previously in Section 2.2.2, they instead form a self-similar shape where the ratio between the head width and head length is held constant at $w_h/\ell_h = 1.24 \pm 0.04$. This ratio was also examined for autocatalytic plume heads, and it was found that they do not maintain a self-similar morphology, as shown in Fig. 3.7. Instead, w_h/ℓ_h has a nonlinear, generally increasing trend with considerable fluctuation as the plume head evolves. A steep increase in the rate of change of w_h/ℓ_h over time occurs after pinch-off has taken place.
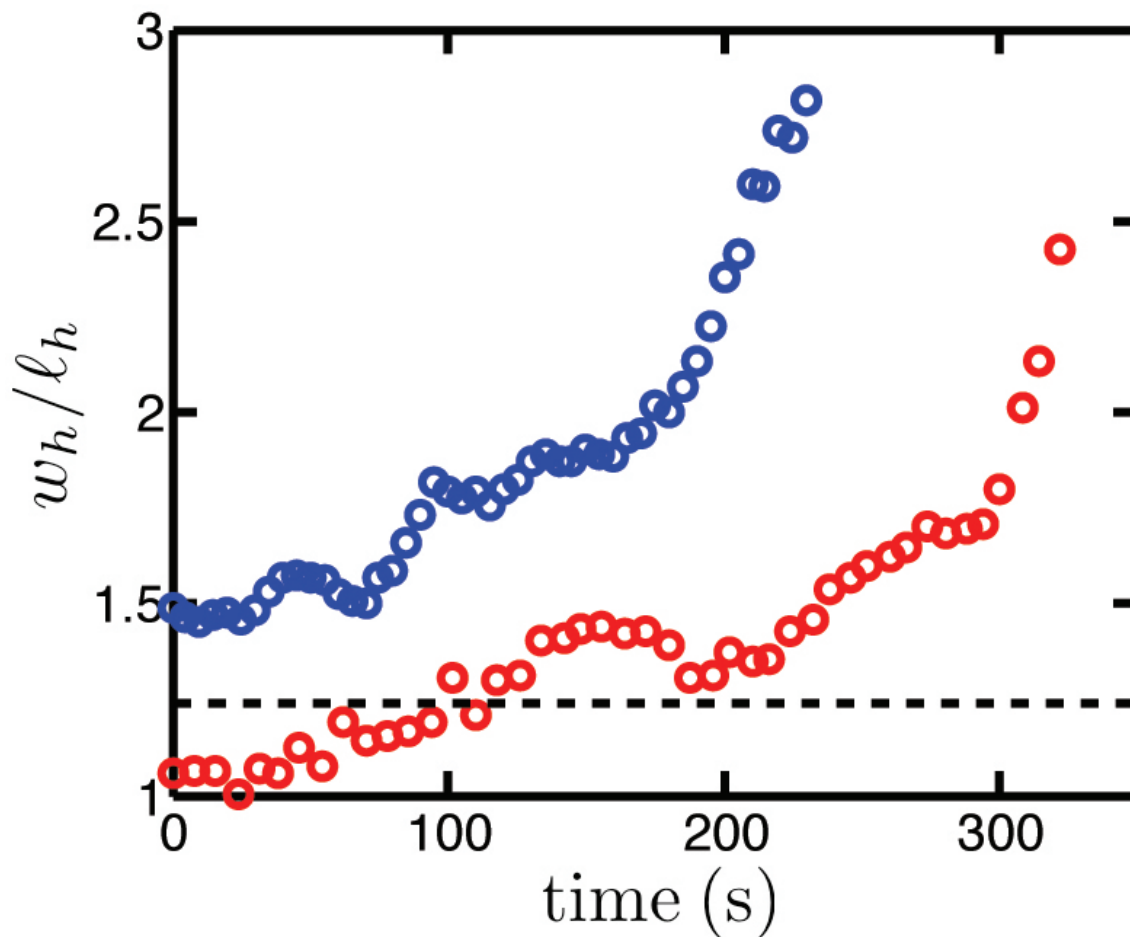
Figure 3.7: The ratio of w_h/ℓ_h for autocatalytic plumes in a 30% (blue circles) and 40% (red circles) glycerol solution. The dashed line indicates the constant value of w_h/ℓ_h observed for forced plumes. At time = 0 is approximately when a vortex ring forms in the head, not the moment when the reaction front first emerges from the capillary tube.

3.2.2   Dimensionless scaling

It is useful to characterize autocatalytic starting plumes by various dimensionless numbers. This allows us to characterize the effects of concentration and temperature on flow fields in a general way, and it forms the foundation of the numerical plume model presented in Chapter 5. The dimensionless numbers discussed in this Section were introduced in a general way in Sections 1.2 and 1.3.2; they are revisited here and applied specifically to autocatalytic plumes.

The Reynolds number achieved by the autocatalytic starting plumes varied depending on the viscosity of solution. For all viscosities, the Reynolds number of the head never

exceeded

$$\text{Re} = v w_h / \nu \sim 20. \tag{3.1}$$

This value for Re was reached in a 20% by volume glycerol run where $w_h \sim 2.9$ cm was the diameter of the plume head, $v \sim 0.12$ cm/s was the ascent velocity and $\nu = 1.75 \times 10^{-2}$ cm^2/s was the kinematic viscosity of the solution. While the flow is certainly laminar, it is not so slow as to be considered Stokes or creeping flow, for which Re $\ll 1$. Further discussion about the Reynolds number achieved by autocatalytic plume heads in solutions with different glycerol concentrations follows below in Section 3.2.3.

As discussed in Section 3.1.2, sufficiently viscous fluid in vertically oriented capillary tubes will suppress convection and the sharp IAA reaction front is observed to propagate at constant speed in either direction. The same effect is observed in sufficiently narrow capillary tubes in which the water is the only component of the solvent [46]. If the tube radius a is increased beyond a critical size, the front deforms and upward propagation is accompanied by convection [87]. Within a simple thin front approximation [87, 47], the relative importance of buoyancy is described by a dimensionless quantity

$$S = \frac{g' a^3}{\nu D_c}, \tag{3.2}$$

where ν is the kinematic viscosity, D_c is the diffusion constant of the autocatalyst, and $g' = g\delta = (\rho_u/\rho_r) - 1$ is the reduced gravity which quantifies the dimensionless density jump between the reacted (ρ_r) and unreacted (ρ_u) solutions. The critical value for the onset of convection in round tubes is $S_c \sim 90$. At slightly larger values $S > S_c$, a transition to an axisymmetric mode of convection can be identified [46]. In the plume experiments described below, a very large tube was used, corresponding to $S \approx 10^8$.

While δ combines the effects of both thermal expansion due to the heat of reaction and the solutal density decrease of the product solution, more recent work considers these effects separately. Following the formulation in Refs. [45, 67, 94], the two separate Rayleigh numbers given in Eq. 1.11 may be used to characterize the contribution to buoyancy from thermal and solutal effects. Restated here, these Rayleigh numbers are

$$\text{Ra}_T = \frac{g\alpha L^3}{\nu D_c} \Delta T \quad \text{and} \quad \text{Ra}_c = \frac{g\beta L^3}{\nu D_c} \Delta c \,, \tag{3.3}$$

where ΔT and Δc are the temperature and concentration differences across the reaction front. Here, α and β are the thermal and compositional expansion coefficients, the

dimensional response of the fluid to changes in temperature and concentration of product, respectively. L is a length scale for which there are several possible choices, as discussed below. Ra_T and Ra_c are the thermal and concentration Rayleigh numbers; replacing a in Eq. 3.2 with L, the length scale, the sum of Ra_T and Ra_c is equivalent to the driving parameter S. Ra_T and Ra_c differ from the conventional definition of Rayleigh number, given in Eq. 1.8, by the replacement of κ, the thermal diffusivity, with D_c, the diffusivity of the catalyst.

Other dimensionless numbers that may be used to characterize autocatalytic chemical plumes are the Lewis number, $\mathrm{Le} = \kappa/D_c$, the Schmidt number, $\mathrm{Sc} = \nu/D_c$, and the Prandtl number, $\mathrm{Pr} = \nu/\kappa$, previously discussed in Section 1.2. For the 40% glycerol solution, using $\kappa = 1.2 \times 10^{-3}$ cm^2/s and values from table 3.1, we find $\mathrm{Sc} \approx 9 \times 10^3$ and $\mathrm{Le} \approx 3 \times 10^2$. The large value of Le indicates that heat diffuses much faster than concentration, so we expect the reaction front to be very sharp compared to the smoother temperature field that will surround the plume. Similarly, $\mathrm{Pr} \approx 32$ indicates that the flow field due to the viscous response of the surrounding fluid will still be smoother than the thermal field.

One choice for L is the small length scale ℓ which emerges from the chemical rate constants. The thickness of the reaction front scales with ℓ, which is by far the shortest length scale in the problem. ℓ can be estimated by introducing a reaction timescale $\tau = 1/(\gamma \Delta c^2)$, where γ is a kinetic constant $\gamma = k_c[\mathrm{H^+}]^2$ [67, 45, 94], and k_c is the rate constant from Eq. 1.21. Then $\ell = \sqrt{D_c \tau}$. For a 40% glycerol plume, using $\gamma = 1800$ M^{-2}s^{-1}, $\tau = 22$ s, and $\ell = 1 \times 10^{-2}$ cm, the Ra numbers are $\mathrm{Ra}_T \approx 1.2$ and $\mathrm{Ra}_c \approx 2.0$.[1]

The characteristic velocity, $U = \ell/\tau = 4.5 \times 10^{-3}$ cm/s, is on the order of the velocity measured for traveling fronts in the absence of convection, which were measured to travel downward in a capillary tube at 9.9×10^{-4} cm/s. In this scaling, then, we find that the plumes are rather weakly driven because $\mathrm{Ra}_T + \mathrm{Ra}_c$ is of order 1. In the plume configuration, however, there is no threshold, or critical value of the driving parameter below which the front is hydrodynamically stable. In vertical tubes, where the length scale L is taken to be a, the radius of the tube, fronts are stable against convection for $S = \mathrm{Ra}_T + \mathrm{Ra}_c < 87.9$ [47]. In our plume experiment, if L is taken to be the radius of

---

[1]The following parameter values were used for calculations: $g = 981$ cm/s^2, $\Delta T = 0.5$°C, $\nu = 3.81 \times 10^{-2}$ cm^2/s, $\alpha = 4.3 \times 10^{-4}$ °C^{-1}, $k_b = 4.5 \times 10^8$M^{-4}s^{-1}, $\Delta c = [\mathrm{IO_3^-}]_0 = 0.005$ M, and $[\mathrm{H^+}] = 0.002$ M. $\beta \Delta c$ was found by measuring ρ_u and ρ_r in a U-tube densitometer. It was found that $\rho_r = 1.1124$ g/cm^3 and the isothermal density difference was found to be $\rho_r - \rho_u = 4 \times 10^{-4}$ g/cm^3. This gives a solutal dimensionless density jump of $\beta \Delta c = (\rho_u/\rho_r) - 1 = 3.6 \times 10^{-4}$.

the tube, $\mathrm{Ra}_T + \mathrm{Ra}_c$ becomes very large, of order 10^7. Another sensible scale to adopt for comparing plumes to tube and slot experiments is $L \sim R$, the radius of the plume itself. In this scaling, $\mathrm{Ra}_T + \mathrm{Ra}_c \sim 10^6$, still very large.

It should be noted that the above formulation for the reaction timescale is for an IAA system that is buffered to have a constant pH. In our unbuffered system, we make use of the pH change that occurs across the reacting front to visualize the location of the front. However, as shown in Ref. [56], the front propagation velocity changes very little within the pH change that we measure for our reacted and unreacted solutions. The unreacted solution has a pH of ~ 5.9, while the reacted solution has a pH of ~ 2.7.

From these scaling considerations, it is clear that the plumes are much more strongly driven by buoyancy than any convecting IAA reaction previously considered, yet they still occur at very moderate Reynolds numbers, and hence fall well within the laminar flow regime.

3.2.3   Subsequent generation plume heads

Analysis of autocatalytic chemical plumes in the previous Sections was restricted to the the first generation plume head. As mentioned in Section 3.2.1, however, following pinch-off of a head, a subsequent generation head is produced below the progenitor preceding it. This process can repeat itself as the flow of upwelling product solution makes its way further up the tank. The possibility of pinch-off ends when a newly developing plume head does not have time to pinch-off before it reaches the top of the tank. In this Section, we extend our analysis to include all subsequent generation plume heads.

In the 32 cm high cylindrical tank, the maximum number of fully developed plume heads produced was four. This occurred for a run in a 30% glycerol solution. Typically, plume runs at concentrations of 30% glycerol and greater produced heads that pinched-off, while for 20% glycerol pinch-off seldom occurred. Experiments without glycerol did not produce pinch-off. To test whether or not the number of pinch-offs could be increased by giving plumes more vertical space to develop, a few runs were performed in an apparatus with equivalent dimensions to those given for Fig. 3.2, but with a cylinder height of 40.6 cm. These runs were only performed for glycerol concentrations of 20, 40, and 50%. For 50% glycerol plumes, no additional plume heads were generated. However, for 20% glycerol plumes, extending the length allowed for a single pinch-off to occur, as opposed to no pinch-offs for runs in the shorter cylinder. The maximum number of
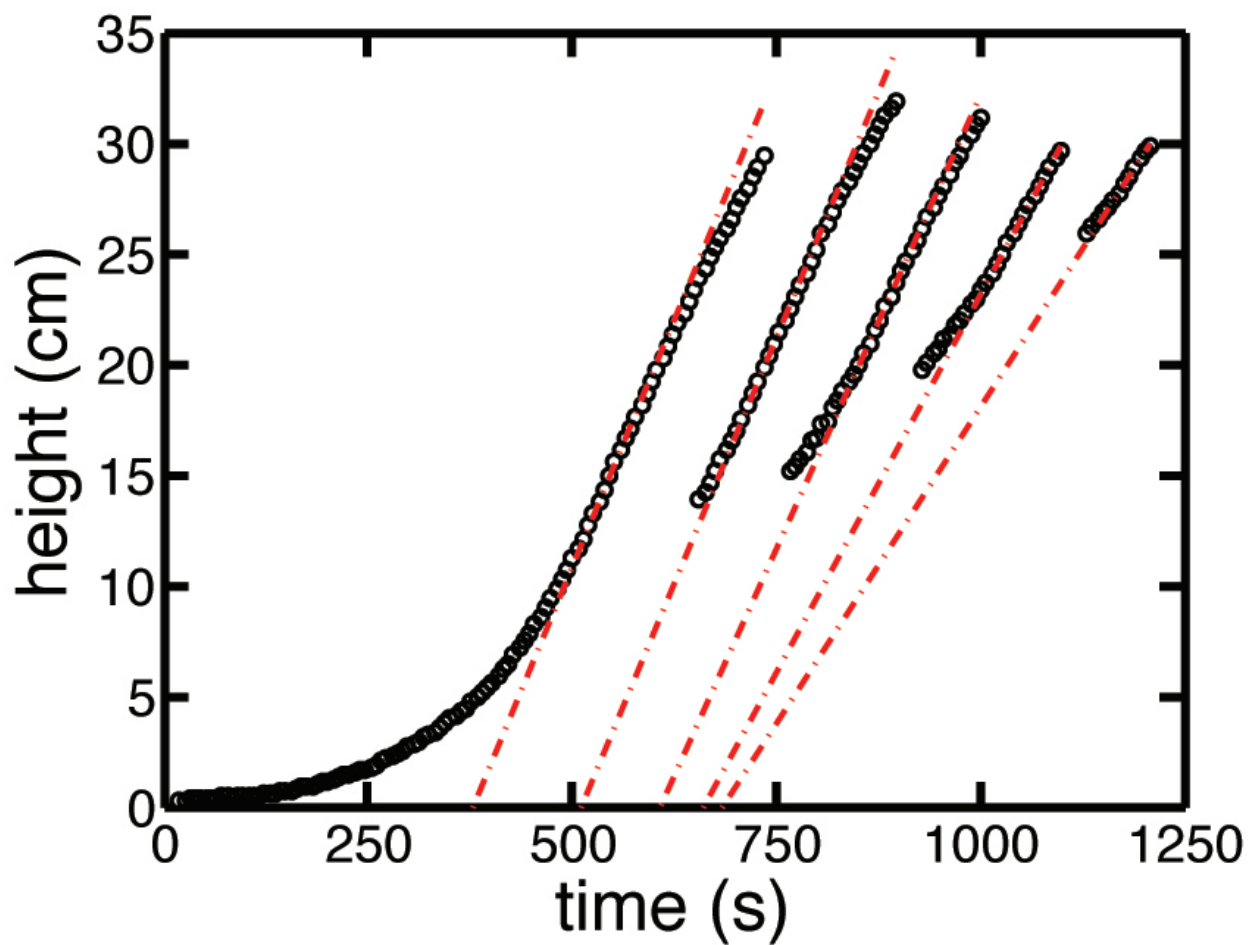
Figure 3.8: The height as a function of time for five plume heads produced by a 40% glycerol ($Sc = 9.2 \times 10^3$) run in the long cylinder version of the apparatus.

fully developed heads for a 40% glycerol run in the longer cylinder was five, compared to three heads for the shorter cylinder. The ascent data for all five plume heads is shown in Fig. 3.8. For each of these heads, velocities were calculated for all sets of five consecutive height measurements, which occured over a span of 30 seconds. This analysis was carried out for all plume runs. From the maximum velocity calculated for each plume head, v_{max}, a head Reynolds number, $\text{Re}_h = v_{max} w_h / \nu$ was calculated. Consistently, Re_h for each plume head in a given run is approximately the same, with the exception of the final plume head. The value of Re_h for the last head was always less than the others, mainly due to the smaller value of its v_{max}. This is because the last head develops closest to the top of the tank, which means that it has less time to accelerate than any of the other plume heads. In addition, by the time the final head is produced, the amount of space the final head has to develop is further decreased by the growing mass of product solution at the top of the tank.

For all plume runs, the head Reynolds number Re_h was calculated and averaged for the all plume heads, with the exception of the final head if there was more than one. An average value of Re_h was calculated for experiments that took place in fluids with same glycerol concentration, and these values are shown as a function of Schmidt number, $\text{Sc} = \nu / D_c$, in Fig. 3.9. Plumes produced for each of the Schmidt numbers displayed in Fig. 3.9 are shown in Fig. 3.10. The Schmidt number was used to characterize each fluid because it quantifies the effect of glycerol concentration on viscosity and on diffusion of the catalyst. For the two lowest Schmidt numbers, corresponding to runs in 0 and 20% glycerol, Re_h is approximately the same. This is mainly due to the typical size of the head produced in these runs. As Fig. 3.10 shows, plumes in water produce very small heads, so while they rise faster than plumes in solution containing glycerol, Re_h will always be limited by smaller w_h values. For plumes in solutions containing glycerol, as Sc increases, v_{max} decreases for solutions with increasing viscosity. Meanwhile, across this domain of Sc, w_h values at v_{max} do not show significant variance. The general trend is that as glycerol concentration is increased (corresponding to an increase in Sc), there is a decrease in Re_h. Generally, in the range of viscosities we studied, all plumes that exhibit pinch-off, such as those shown in Fig. 3.10c-e, have similar morphologies, regardless of the number of times in that pinch-off occurs. These plumes all go through a similar process of growth outlined in Section 3.2.1, regardless of the variation in fluid parameters.
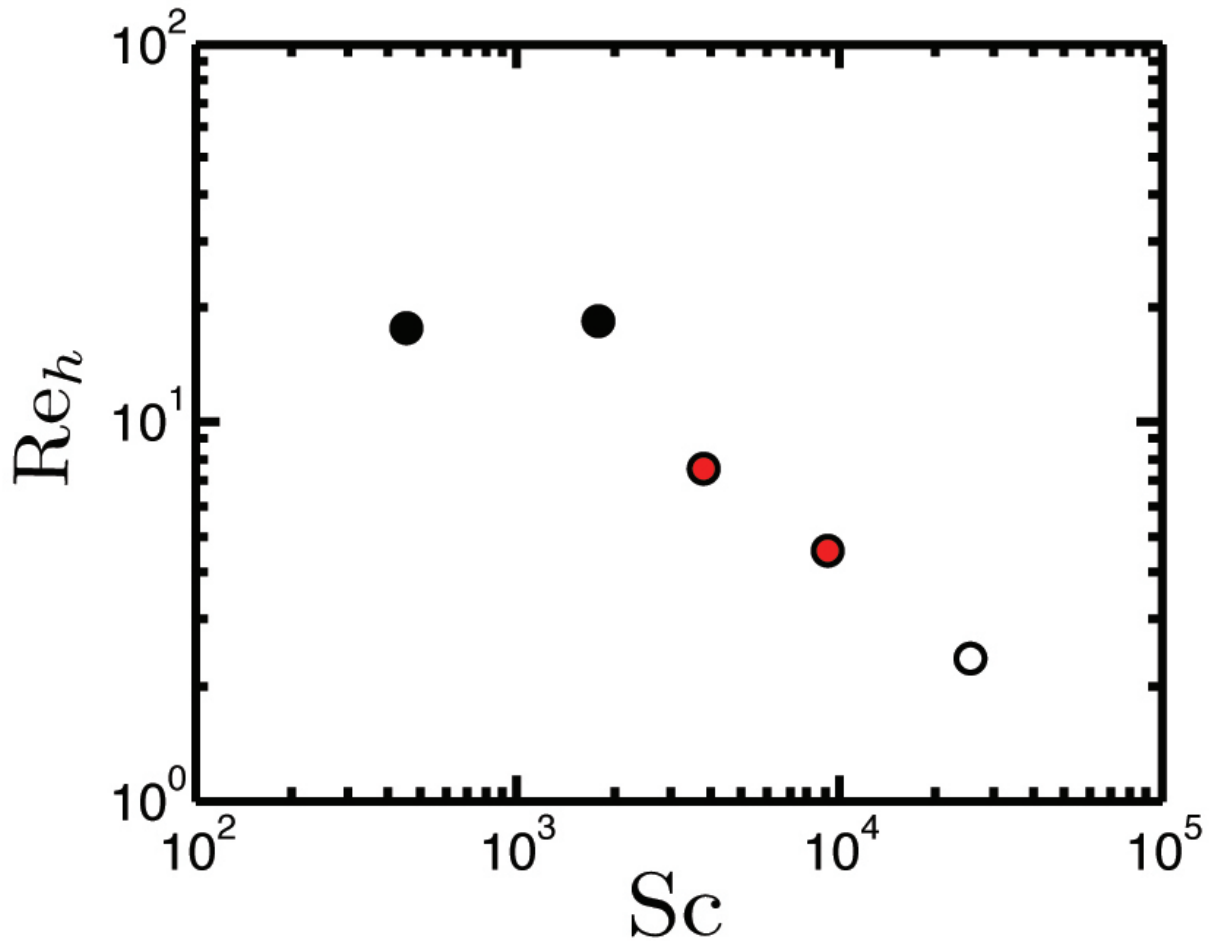
Figure 3.9: Head Reynolds number Re_h averaged for multiple plume runs as a function of Schmidt number, Sc. The Schmidt numbers, in increasing order, are for glycerol concentrations of 0, 20, 30, 40, and 50%. Black shading of the data points indicates runs that do not pinch-off in the standard (shorter cylinder) apparatus, white shading indicates runs where at most one pinch-off occurred, and red shading indicates runs where two or more pinch-offs were observed.
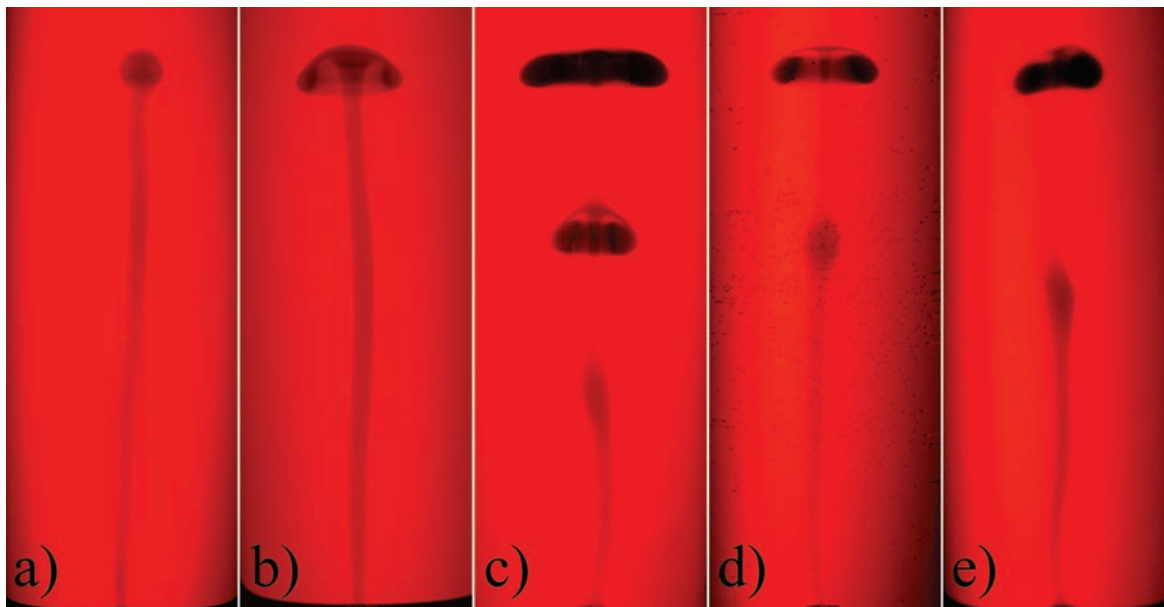
Figure 3.10: The morphology of autocatalytic chemical starting plumes in a) water, and in glycerol concentrations of b) 20, c) 30, d) 40, and e) 50%. The images are all of plumes at a height of ∼20 cm from the outlet. It took each plume a) 255 , b) 555, c) 425, d) 449, and e) 681 s to ascend the final ∼19.5 cm before these images were captured.

3.2.4 Outlook on experimental autocatalytic chemical plumes

The plume experiments discussed in Section 3.2 mark the first study of buoyant, three-dimensional plumes that are directly driven by an autocatalytic reaction. However, two-dimensional plumes have been observed in other, more energetic reactions [95, 96]. Of course, conventional buoyant plumes [4, 28, 97, 98] and vortex rings [4, 99, 100] have been the subjects of extensive previous study.

There is great diversity in past experiments on conventional starting plumes. In typical experiments, conventional starting plumes are formed from a buoyancy flux at a point source. The buoyancy may be due to an isolated heat source, or a small inlet by which buoyant fluid is injected. The injected fluid will either be hotter than the surrounding medium, or compositionally buoyant, or both. In these cases, all the buoyancy is derived from processes external to the experiment and arrives with the volume of injected fluid. Subsequent stirring and entrainment of less buoyant surrounding fluid can only dilute and reduce this buoyancy. In the case of autocatalytic plumes, the volume of buoyant fluid injected to initiate the reaction is negligible, and all of the buoyancy is generated by the conversion of dense fluid into buoyant fluid at the thin reaction front.

Symmetrical plume heads similar to those observed in our experiment can be found in conventional starting plumes, such as those presented in Chapter 2 or in Ref. [98]. Moreover, the heads of these starting plumes can be observed to pinch-off to form buoyant thermals in the form of vortex rings. The formation of thermals by pinch-off has been the subject of theoretical and of experimental interest in conventional systems [22, 24, 101, 102]. Despite the fact that discrete thermals form in both conventional and autocatalytic systems, there is a critical difference in their respective behaviour. This difference is due entirely to the autocatalytic reaction used to drive buoyancy in our system. As a plume head or vortex ring rises, whether or not it is conventional or autocatalytic, it entrains surrounding fluid, stirring it into the structure. In the case of autocatalytic plumes, the surrounding fluid is reactant solution. The delivery of fresh reactant solution feeds the rising vortical structure as it becomes mixed into its interior, and causes it to accelerate both before and after pinch-off has occured. This stirring is laminar, and presumably involves the extreme stretching of the thin reaction front within the vortex ring. The acceleration of autocatalytic plume heads is in contrast to the constant velocity rise behaviour previously observed in conventional plumes as discussed in Chapter 2. The continued acceleration of the head once it pinches-off and becomes a thermal is also unique to our autocatalytic system; conventional vortex rings expand and slow down after they have pinched-off [99].

3.3 Simple plume models

3.3.1 Model formulation

The early stages of growth of an autocatalytic chemical plume resemble a small sphere (the head) on top of a cylinder (the conduit). Moreover, even as the plume head develops a vortex ring in its underbelly, the top of the head maintains a spherical shape as it ascends, as shown previously in Fig. 3.5. We use these first approximations of plume shape to develop two simple dynamical models for plume velocity. In doing so, the question we seek to answer is: can the velocity of a chemical plume be modeled as a reacting sphere or cylinder? The cylinder model is an extension of a model of compositionally buoyant *creeping* plumes [11], where the terminal velocity of a cylinder in very low Reynolds number "Stokes" flow ($Re \ll 1$) was used to model starting plumes as buoyant, growing cylinders. Similar to the cylinder model, the sphere model we develop makes use of
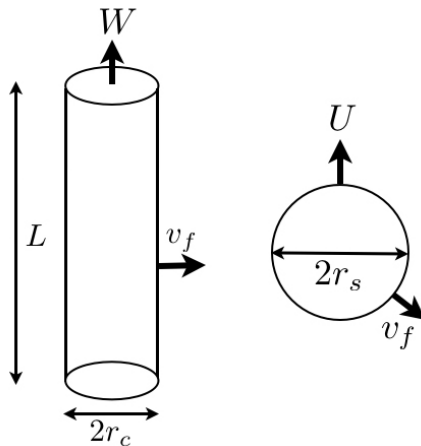
Figure 3.11: A schematic showing the relevant dimensions of the cylinder (left) and sphere (right).

the terminal velocity of a sphere in Stokes flow to model the ascent of the plume head. While our experimental system only produces plumes in the Stokes flow regime for viscous fluids (40% glycerol and above) when plumes are in their early stages of development, it is nonetheless useful to extend the model from Ref. [11] to incorporate reaction into the model, and to compare reacting cylinders with reacting spheres in the Stokes regime.

The formulation of each of the models is very similar. Beginning first with the development of the cylinder model, we start with the terminal velocity, W, of a vertically oriented cylinder moving in low Re number flow [11, 103],

$$W = \frac{bg'r_c^2}{\nu}\log(L/r_c) \tag{3.4}$$

where L is the length of a cylinder of radius r_c, as shown in Fig. 3.11, b is the proportionality factor, ν is the kinematic viscosity of the fluid, and $g' = g(\rho_u - \rho_r)/\rho_u$ is the buoyancy of the cylinder, with g the gravitational acceleration, and ρ_r and ρ_u being the densities of the cylinder (reacted fluid) and the surrounding unreacted fluid, respectively. The cylinder stays attached to the outlet, and therefore the change in length of the cylinder is simply

$$\frac{dL}{dt} = W. \tag{3.5}$$

The change in volume of the cylinder is equal to the volume flux from the reaction, which

is the surface area of the cylinder multiplied by the velocity, v_f, of the reacting front, or

$$\frac{d}{dt}(\pi r_c^2 L) = 2\pi r_c L v_f. \tag{3.6}$$

In this formulation, we have ignored the relatively small buoyancy flux contribution from the top of the cylinder, and only consider the contribution from the curved surface. Differentiating the above equation, we are left with

$$\frac{dr_c}{dt} = v_f - \frac{r_c}{2L}\frac{dL}{dt}. \tag{3.7}$$

Finally, substituting Eq. 3.4 into Eq. 3.7, our model for a reacting buoyant cylinder becomes a set of coupled first-order differential equations for r_c and L,

$$\frac{dr_c}{dt} = v_f - \frac{g'r_c^3}{2\nu L}\log(L/r_c) \tag{3.8}$$

and

$$\frac{dL}{dt} = b\frac{g'r_c^2}{\nu L}\log(L/r_c). \tag{3.9}$$

The derivation of the ascent velocity of a buoyant reacting sphere is simplified by the fact that only one dimension of the sphere can change as it grows, as opposed to two for the cylinder. As we did for the cylinder case, we start with the terminal velocity for a sphere of radius r_s in Stokes flow, which is

$$U = \frac{2}{9}k\frac{g'}{\nu}(r_s)^2, \tag{3.10}$$

where k is the proportionality factor. The relevant dimensions for the sphere are shown in Fig. 3.11. Similar to the cylinder, the change in volume of the sphere is equal to the volume flux from the reaction, which is the surface area of the sphere multiplied by the front velocity, or

$$\frac{d}{dt}(\frac{4}{3}\pi r_s^3) = 4\pi r_s^2 v_f \tag{3.11}$$

which leads to the simple result that

$$\frac{dr_s}{dt} = v_f \tag{3.12}$$

and therefore

$$r_s(t) = v_f t + r_{s0} \tag{3.13}$$

Substituting this result into Eq. 3.10 gives an expression for the velocity of the sphere as a function of time

$$U(t) = \frac{2}{9} \frac{g'}{\nu} (v_f t + r_{s0})^2. \tag{3.14}$$

Integrating $U(t)$ therefore gives us the location of the sphere as a function of time.

3.3.2 Model results and discussion

To determine whether or not the ascent of viscous autocatalytic chemical plumes can be approximated as either reacting cylinders or spheres, or neither, we compared the height as a function of time produced by each model with experimental data. Eqs. 3.8 and 3.9 were integrated numerically using an ordinary differential equation solver based on an explicit Runge-Kutta (4,5) formula. Eq. 3.14 was integrated analytically to determine the position-time relationship of the sphere. The initial conditions for the integrations were taken directly from experimental data of plumes in the range of 1-1.5 cm above the outlet. A picture of such an " initial" condition is shown in Fig. 3.12. The exact height served as the initial position, x_0, of the sphere, or equivalently, the initial length, L_0, of the cylinder. The width of the small sphere of product solution was measured to determine the initial sphere radius, r_{s0}, and the width of the conduit below the sphere was used to determine r_{c0}. In the analysis of experimental data, $t = 0$ is considered to be the initial emergence of the front from the outlet, however since the model equations require a cylinder and a sphere to exist, the time t_0 at which the initial conditions were extracted is artificially set to the time $t = 0$ for convenience. The fluid parameters used were taken from Table 3.1, and values for v_f were taken from front velocity measurements shown in Fig. 3.1.

The coefficients b for the reacting cylinder and k for the reacting sphere determined by varying these parameters to find the best fit for each data set. Interestingly, the model which best matched the experimental data was not always the cylinder or the sphere. The best fit varied for different data sets. The sets that fit the cylinder model used a coefficient of $b \sim 0.21$, and those for which the sphere model fit best used a coefficient of $k \sim 0.13$. The cylinder and sphere model data are shown along with experimental data in Fig. 3.13, which also shows an image of the plume from this data set. Clearly, for
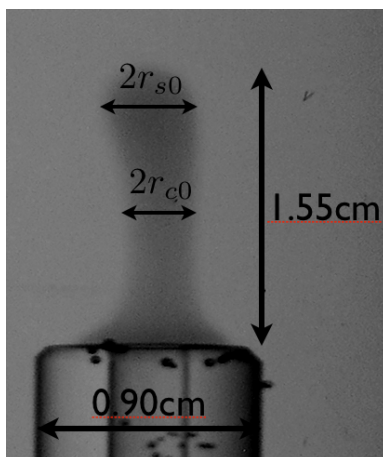
Figure 3.12: An image of an autocatalytic chemical plume in its earliest stage of development. Measurements of plumes at this size were used as the initial conditions for the cylinder and sphere models.

this data set, the cylinder model fits the experimental data very well. A different 40% glycerol run in which the sphere model better suits the experimental data is shown in Fig. 3.14, which once again also shows a picture of the plume from this data set. The reason why these different experimental runs (using the same fluid parameters) require different models to fit their behaviour has to do with the time (or equivalently, the height) at which the plume head pinches-off from the conduit. Plume heads that pinch relatively early are best described by the growing sphere model, whereas plumes where the heads stay attached to the conduit for a longer period of time are better described by the cylinder model. In either case, the fits only work up to the point where the experimental data shows a deceleration. The reasons why a plume head would decrease velocity in its later stages of development were described previously in Section 3.2.1.

Despite the simplicity of the two models we have presented, they both reproduce experimental data in different cases. In the case where one model of the two models fails to reflect the physical data, the other works much better. Different models work for different scenarios; the cylinder model works best for runs where the head stays attached to the conduit for a relatively long time, the sphere model works best for runs where the plume head makes an relatively early departure from the conduit. Ideally, for experimental data for plume runs in the same fluids, the experimental results would be reproduced to within a reasonable degree for each new run. While many of the same general characteristics of autocatalytic plumes were observed in effectively equivalent
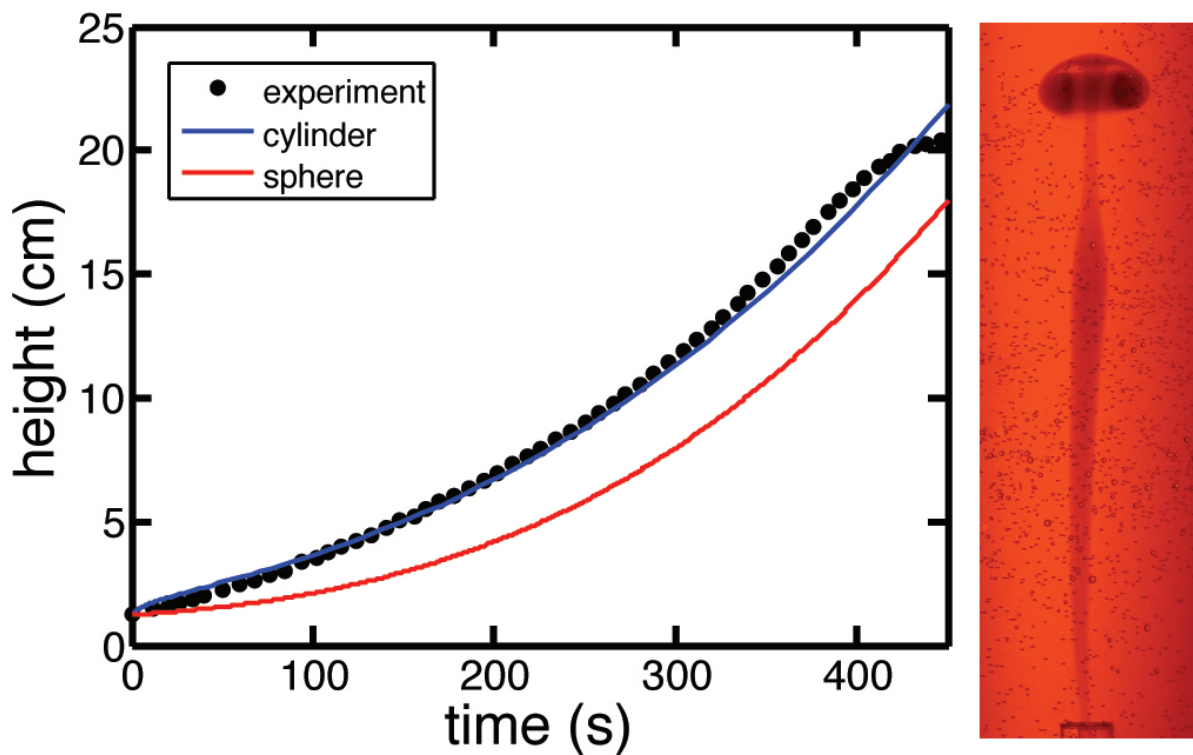
Figure 3.13: Left: Ascent data from an autocatalytic chemical plume best described by the cylinder model. The curves are solutions for the cylinder and sphere models. Right: A picture of the plume that produced this data set at a height of 15.3 cm above the outlet.
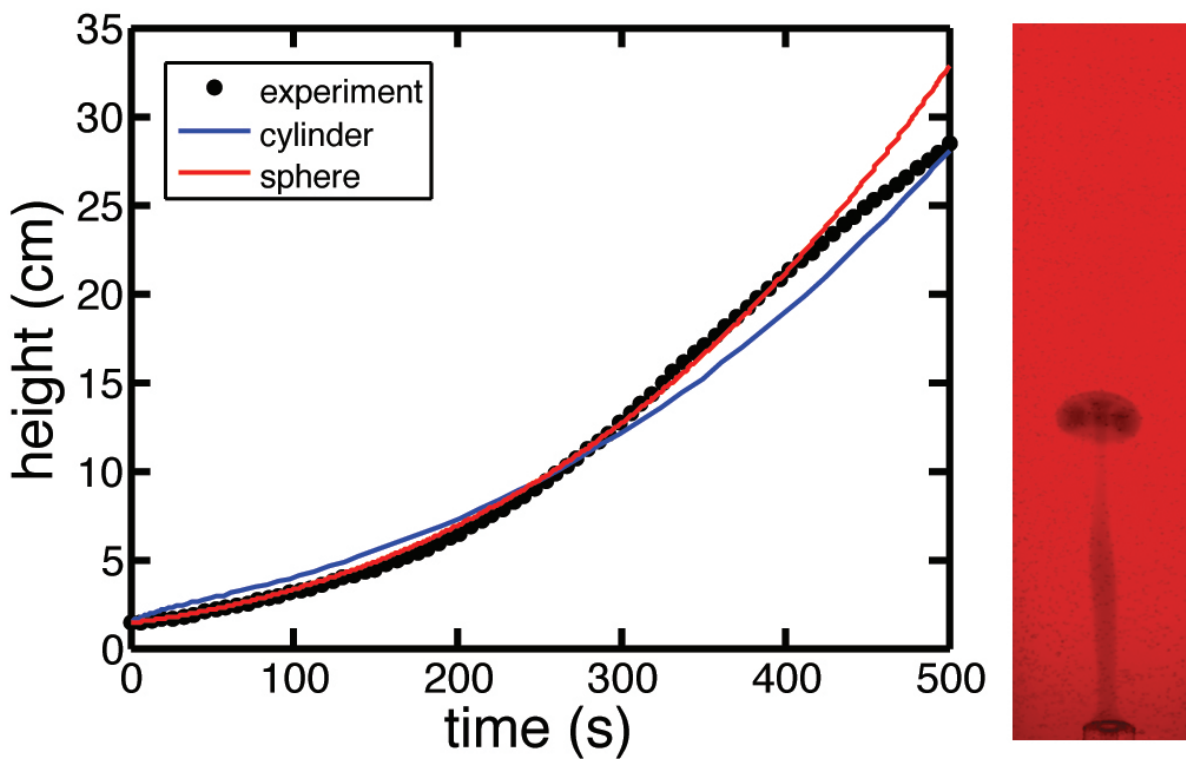
Figure 3.14: Left: Ascent data from an autocatalytic chemical plume best described by the sphere model. The curves are solutions for the cylinder and sphere models. Right: A picture of the plume that produced this data set at a height of 8.6 cm above the outlet.

experimental runs, such as acceleration of the plume head and subsequent pinch-off, other characteristics of the runs varied, such as the height where pinch-off takes place and the number of pinch-offs observed. This variation suggests that there is an inherent reason for the element of unpredictability observed in this system. One of the most useful aspects of the model is that it helps provide an explanation as to why this is the case.

In evaluating the initial conditions needed to execute the integrations needed for the model, it was clear that in the earliest stages of plume development there was some slight variation in the parameters measured at t_0, even for plumes at nearly exactly the same height. The largest variation was in the size of the approximately spherical head. In some cases it was barely distinguishable from the conduit, whereas in other it was large enough to be clearly distinguished from the conduit. To investigate the sensitivity of the initial conditions, the cylinder and sphere models were compared for different values initial sphere radius r_{s0}. The value $\beta = r_{s0}/r_{c0}$ is used to express the ratio of the initial sphere and cylinder radii. The results of this comparison for initial conditions $x_0 = L_0 = 1.0$ cm, and $r_{c0} = 0.1$ cm, and fluid parameters $(\rho_u - \rho_r)/\rho_u = 3.6 \times 10^{-4}$, $\nu = 3.81 \times 10^{-2} \text{cm}^2/\text{s}$, and $v_f = 1 \times 10^{-3}$ cm/s, along with proportionality constants $k_w = 0.125$ and $b = 0.205$ are shown in Fig. 3.15. For these conditions, it is clear that for $\beta = 1$ the plume will behave very much like the one pictured in Fig. 3.12, where pinch-off will occur later in the development of the plume. The height of the sphere in this simulation does not reach the height of the cylinder at any point during the course of the run. For $\beta = 1.5$, the sphere height overtakes the cylinder height at a height of approximately 17 cm. This indicates that pinch-off a plume at this $\beta = 1.5$ would occur earlier than for the $\beta = 1.0$ case. Finally, for $\beta = 2.0$, the sphere velocity overtakes the cylinder velocity much earlier than the $\beta = 1.5$ case. A plume with this initial condition would behave much like the plume shown in Fig. 3.14, in which pinch-off occurs relatively early. The initial conditions for the Fig. 3.13 plume are $x_0 = L_0 = 1.2$ cm, and $\beta = 1.0$ with $r_{s0} = 0.13$ cm, while for the Fig. 3.14 plume they are $x_0 = L_0 = 1.4$ cm, and $\beta = 1.6$ with $r_{s0} = 0.22$ cm.

Taking into account the limitations of comparing our experimental results to models developed for flow in the Stokes regime, it is nonetheless useful to use these models as a guide for helping to understand the behaviour of autocatalytic plumes, even though their flow is only in the Stokes regime during the earliest stages of their development. The model results suggest that the evolution of an autocatalytic plume is sensitively dependent on the dimensions it takes in the very earliest stages after it emerges from the
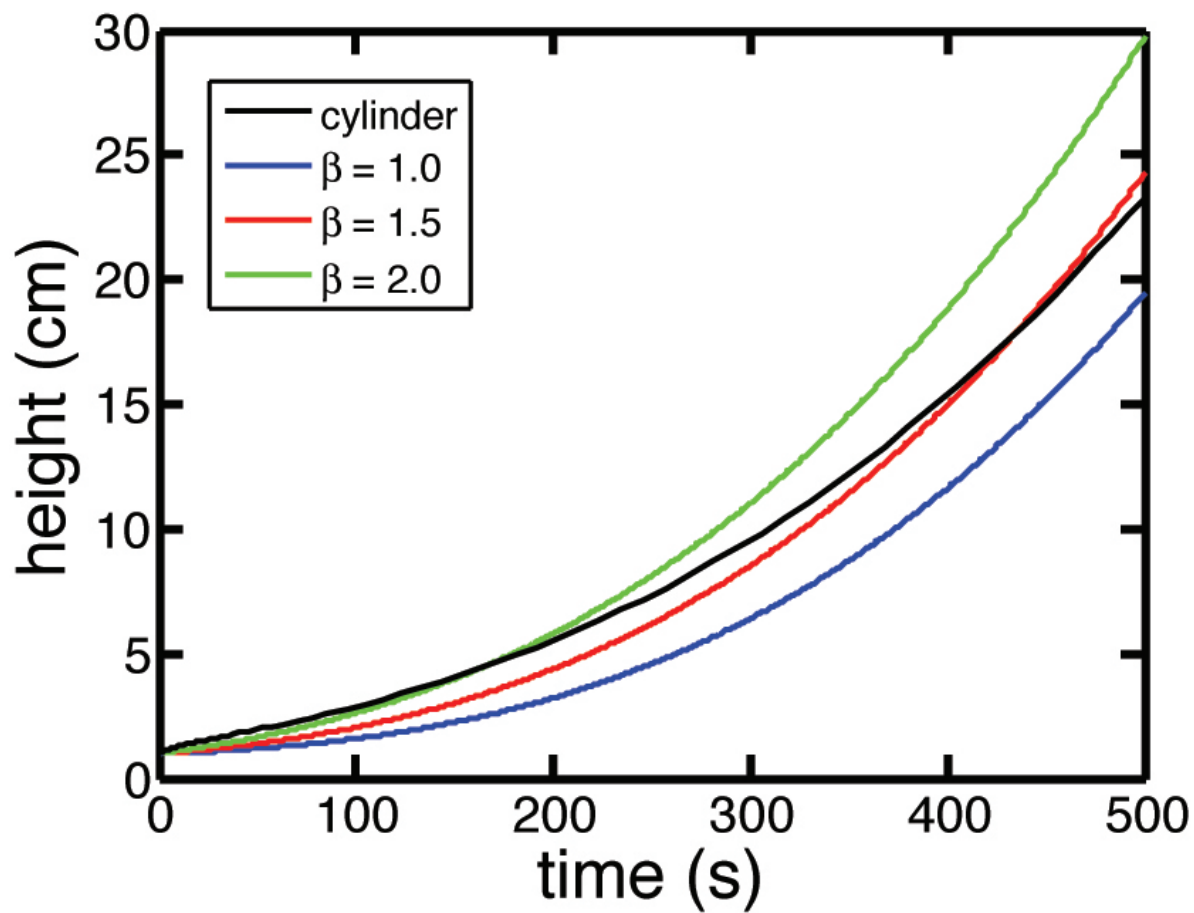
Figure 3.15: Cylinder and sphere model solutions at three different values of $\beta = r_{s0}/r_{c0}$.

outlet. Small differences in these dimensions play a critical role in the amount of time it takes for the initial head to pinch-off. Since an earlier pinch-off will result in more time for multiple pinch-offs to occur, slight differences in "initial" plume dimensions also account for the variability observed in the number of pinch-offs observed for plume runs in the same fluids. We can therefore consider pinch-off to be a type of convective instability where small scale variations in conditions at the outlet grow as the plume rises downstream and result in large scale variations in the pinch-off process. The physical effect that is the most likely source of these small scale variations is exchange flow in the capillary tube. As the reaction front approaches the end of the capillary tube outlet, there is an unstable density difference between the fluid in the capillary tube and in the cylinder full of unreacted fluid above it. This instability can create flow by forcing a small amount of reacted solution out of the the capillary tube as the overlying fluid forces its way in. The Rayleigh number used to quantify the buoyancy effects due to density differences in a pipe is

$$\mathrm{Ra}_p = \frac{g'd^4}{\nu LD} \tag{3.15}$$

where L is the length of the pipe, d is the pipe diameter, and D is the diffusion constant for the species producing the density difference. For the autocatalytic plume experiment in 40% glycerol $\mathrm{Ra}_p = 4$. As a comparison, typical values of Ra_p used to study turbulent exchange flow in a pipe are $\mathrm{Ra}_p > 10^8$ [104]. Although the small scale exchange flow at the outlet driven by a buoyant instability with $\mathrm{Ra}_p = 4$ is relatively small, it is likely enough to account for the nonuniformity in the initial stages of the emerging plumes that we have observed.

3.4   Summary

We have described a study of buoyant, three-dimensional plumes driven by the iodate-arsenous acid reaction. In a water solution that was made more viscous with the addition of glycerol, we found that a rising plume with a well-defined head was formed. The plume head grew to a critical size and subsequently detached from the upwelling conduit to form a buoyant vortex ring. The entrainment of reactant solution into the autocatalytic chemical plume head and vortex ring produced additional buoyancy by assisting the chemical reaction, leading to an acceleration of the vortex ring. This behaviour reverses the usual role of entrainment, which normally acts to reduce buoyancy in conventional

plumes and thermals.

During an experimental run, pinch-off of a plume head resulted in the generation of at least one additional plume head, and often led to even more. With the exception of the final plume head produced, these subsequent generation plume heads yielded the same value of the head Reynolds number Re_h as was determined for the initial plume head.

While Re_h was nearly the same for all experimental runs using the same fluids, the location of the initial pinch-off of a plume head and the number of pinch-offs observed during an experimental run varied. Using two simple models of chemical plumes, a reacting cylinder and a reacting sphere, it was shown that the behaviour of an autocatalytic plume could conform to the flow predicted by either model. The factor that determined which model was relevant to a particular experiment was the "initial" size of the plume head (a sphere in its early "initially" stage of growth) and conduit (a cylinder). In general, the larger the size of the spherical head in relation to size of the cylindrical conduit, the more likely the ascent of an autocatalytic plume head would compare favourably to the ascent of a reacting sphere. Moreover, plume heads that conformed to the spherical ascent prediction always pinched-off earlier (at a lower height) than plumes that conformed to the cylindrical ascent prediction. In addition, early pinch-off meant that more subsequent generation plume heads could be produced.

Based on these findings, we conclude that the evolution of an autocatalytic plume is sensitively dependent on the dimensions it takes in the very earliest stages after it emerges from the outlet. Small fluctuations in flow near the outlet from exchange flow or other factors lead to large variations in the later stages of autocatalytic plume evolution.

Chapter 4

Steady Plumes

Plumes are typically formed when a continuous source of buoyancy is supplied at a localized source. In Chapter 2, we studied laminar plumes produced by injecting compositionally buoyant fluid into ambient fluid. In Chapter 3 we analyzed starting plumes where buoyancy is supplied by an autocatalytic chemical reaction: the iodate - arsenous acid (IAA) reaction. In both Chapters 2 and 3, we focused only on the life of the plume up until the head (or heads) reached the top of the fluid in the tank. For the case of compositionally buoyant plumes, it is well known that after this transient, or "starting" period, a steady flowing conduit persists as long as the source of buoyancy remains steady. For the case of autocatalytic chemical plumes, after the initial transient during the ascent of the head, we observed the emergence of a steady state in the conduit morphology and flow. In this Chapter, autocatalytic plumes are compared to non-reacting, compositionally buoyant steady plumes using GERVAIS, an MRI velocimetric technique. We have found that autocatalytic conduits have axisymmetric bimodal velocity profiles and cone-shaped morphologies, in contrast to the Gaussian profiles and cylindrical shapes of non-reacting conduits. The bimodal distribution for autocatalytic plumes is a consequence of the unique effect of entrainment (for a plume) in this system. Rather than the usual effect of entrainment in non-reacting plumes, where less buoyant fluid is incorporated into the plumes, entrainment in autocatalytic plumes provides a buoyancy flux along the entire conduit by means of chemical reaction, thereby delocalizing the buoyancy source.

This Chapter is organized as follows. In Section 4.1 we will discuss the details of the experimental design and dynamic magnetic resonance imaging. The velocity profiles of plume conduits and plume conduit morphology are discussed in Section 4.2, followed by a brief summary in Section 4.3.

4.1   Experimental design

The experimental apparatus consists of a cylindrical glass pipe (the reaction vessel) inserted into the bore of an MRI spectrometer, as shown in Fig. 4.1. The MRI spectrometer used in our experiments is a Bruker Biospin DMX 200 with a vertical 149 mm bore 4.7 Tesla superconducting magnet operating at a ^{1}H frequency of 199.7 MHz with a 64 mm birdcage radio frequency probe. A Bruker water-cooled 3-axis shielded gradient system used with BAFPA 40A amplifiers was used to achieve spatial resolution. The bottom end of the glass pipe has a glass floor with a vertical glass capillary tube built into its centre. The top end of the pipe was left open. The capillary tube was sealed at the outside (bottom) end with rubber tubing. The pipe used in the experiment is 1.25 m in length, with an inner diameter of 55 mm. The inner diameter of the capillary tube is 3.0 mm. For all experimental runs in which an autocatalytic chemical plume was produced, the glass pipe was filled with 700 mL of reactant solution consisting of $[IO_3^-]$=0.005M, $[As(III)]$=0.020M, 2×10^{-5}M congo red indicator, and 40% glycerol by volume in water. The preparation of this solution and the measurement of some of its physical properties were previously described in Section 3.1.1. Reactions were initiated by injecting a small amount (less than 0.1 mL) of catalyst solution into the rubber tubing at the bottom end of the capillary tube using a hypodermic syringe. Once initiated, a reaction front would ascend vertically into the capillary tube, where it would proceed upward at a speed of $\sim 1 \times 10^{-3}$ cm/s. Upon reaching the top of the capillary tube, which was immersed in reactant solution, the reaction front continued to move slowly upwards. Eventually, the reaction front formed a plume of product solution rising into the ambient reactant solution.

For comparison, non-reacting, compositional plumes were studied in the same glass pipe used for autocatalytic plume experiments. Since compositional plumes must be created by continuous injection of buoyant fluid into the pipe, a syringe pump was connected to the bottom end of the capillary tube, allowing fluid to be injected at a desired rate. The syringe was filled with 38% glycerol solution by volume, and the cylindrical vessel was filled with 40% glycerol solution, giving it the same glycerol-water composition as was used for autocatalytic plume experiments. Using an Anton Paar DMA 5000 density meter, the density of each of these solutions at 20.0°C were measured to be 1.1160±0.0003 g/cm^3 for the 40% solution and 1.1097±0.0003 g/cm^3 for the 38% solution. Experimental runs were made for injection flow rates from 0.5 mL/min to 2.0 mL/min. All experiments

were performed at room temperature, which was approximately 20°C.

Once the IAA reaction front moves into the reaction vessel, the system enters a period where quiescent fluid is driven into motion by the conversion of reactant to product. During this time, there is an initial transient period of fluid flow followed by a much longer lasting steady state period. During the transient period, initially a slow creeping plume of product solution is formed. From this creeping plume, a starting plume with a well-defined head eventually develops, and later the plume head pinches-off from the plume conduit, forming a free vortex ring. The location of pinch-off nucleates another plume head, and the process of pinch off is repeated. The evolution of the plume during the transient period was described in detail in Section 3.2.1. Once the series of pinch-offs stops and the transient period ends, a steady stream of reacted solution forms a conduit that delivers product solution to the top of the vessel. Here, at the top of the vessel, the product solution accumulates, forcing its way downwards as its volume increases, eventually engulfing all of the upwelling conduit. Using the plume apparatus described in Section 3.1.3, and shown in Fig. 3.2, digital images showing the evolution of an autocatalytic plume and subsequent formation of a long-lived conduit are shown in Fig. 4.2. If we consider a horizontal cross section of the flow at a given height intermediate to the outlet and the surface of the fluid, we initially see transient behaviour when the plume first penetrates the cross section, but soon after the flow of the plume conduit reaches a steady state. This state was found to persist until the growing volume of product solution made its way downward and moved through the cross section. Here we consider only flow across a given cross section during the time in which the conduit is in steady state flow.

4.1.1 Dynamic MRI

Flow was measured in our experiments using dynamic magnetic resonance imaging (MRI) [105]. MRI technology utilizes the nuclear magnetic resonance (NMR) of protons with magnetic moments, such as ^{1}H, to extract images of the location of those protons. The magnetic moments of the protons are aligned in the magnetic field created by a large magnet, and then are deflected by a radio-frequency (RF) pulse. As they return to their original alignment, the atoms emit a signal at a resonant frequency dependent on the strength of the magnetic field. The spatial location of the protons is resolved by additional gradients in the magnetic field. Gradient coils produce these gradients
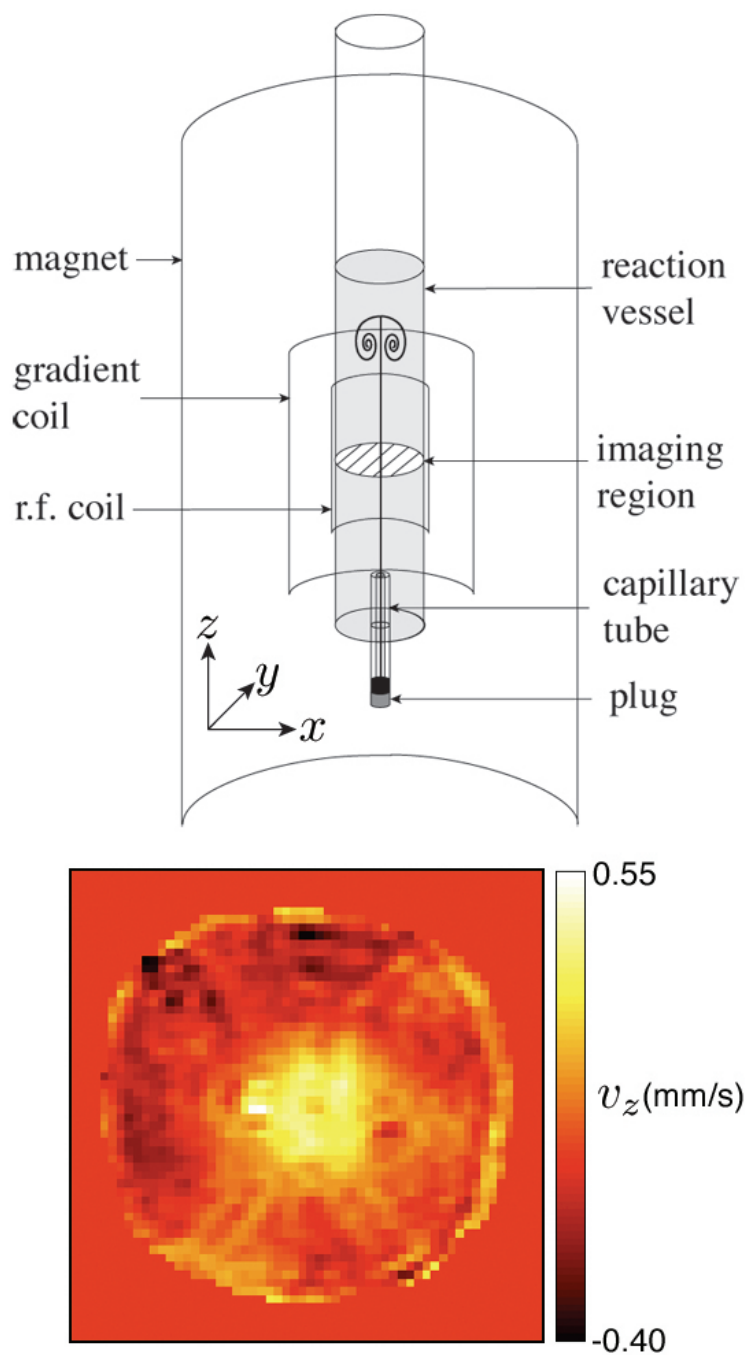
Figure 4.1: Top: Schematic diagram of the cylindrical reaction vessel placed inside the bore of the MRI spectrometer (shown in cross section). Bottom: A typical MRI velocity image of an autocatalytic chemical plume when the imaging region is 15 cm above the outlet of the capillary tube. The size of the imaging region in view is 64×64 mm, and $v_z = 0$ is indicated by the color of the imaging region surrounding the pipe.
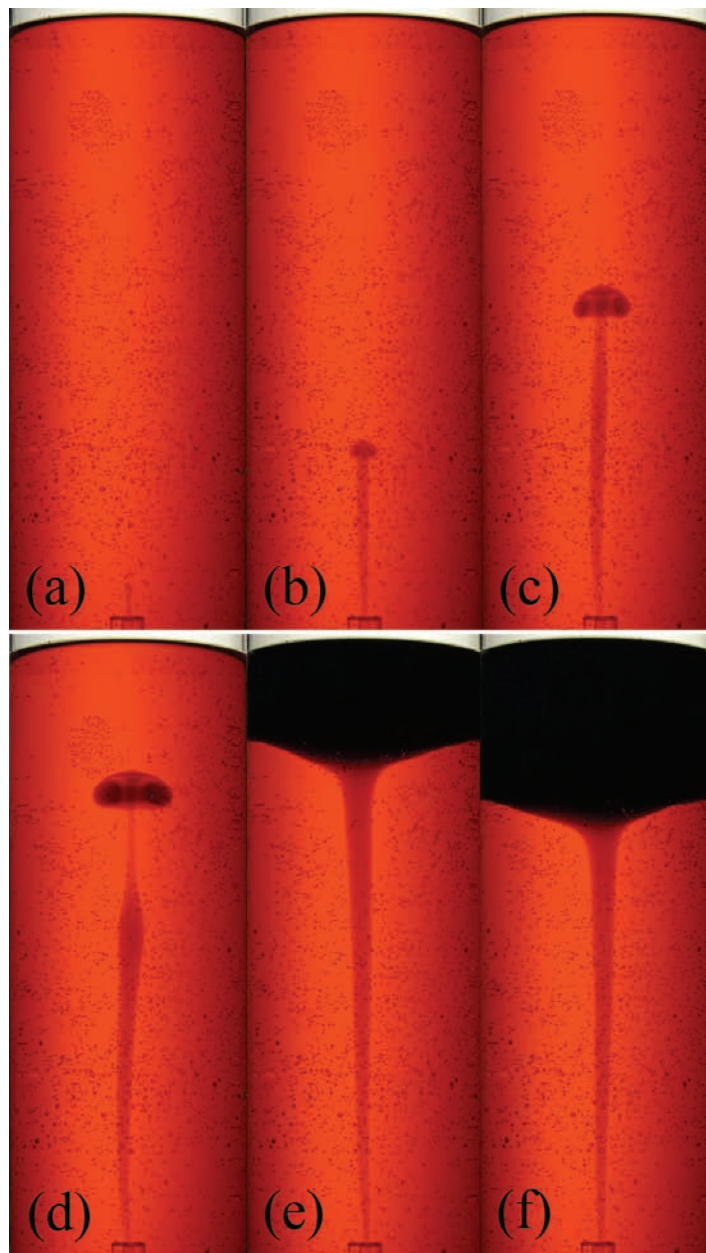
Figure 4.2: A sequence of images during the evolution of an autocatalytic chemical plume. During the ascent of the plume head towards the top of the container, as shown in (a) through (c), the plume head grows, and in (d) it pinches-off, forming a free vortex ring. The point of pinch-off proceeds to swell, nucleating a new plume head. As the steady flow of product solution moves upwards by means of the conduit, a growing volume of product solution accumulates at the top of the vessel, as shown in (e) and (f). Using $t = 0$ as the time at which the front first emerged from the capillary tube, the times at which the pictures were taken in (a) through (f) are $t = 67, 253, 371, 443, 1492$, and 2302 seconds respectively. The distance from the capillary tube to the top surface of the fluid is 21.6 cm, the inner diameter of the cylinder containing the plume is 8.9 cm.

by producing a difference in the resonant frequency signal from the protons based on their location. The term *dynamic* MRI simply refers to multiple MR images viewed in succession, thereby constituting a MRI movie. In addition to measuring location of a specific proton, magnetic resonance velocity images can be obtained for coherent molecular motion, thus allowing for the determination of a velocity field for a flow.

Velocity images of our plume flows were obtained by utilizing the GERVAIS pulse sequence [81], which is used commonly in phase shift velocity imaging [105]. In this technique, velocities are extracted from phase shifts in the MR images produced from a pair of magnetic field gradient pulses. The pulse pair imparts a phase shift that is proportional to the velocity in the direction of the gradient. In our experiments, gradients in the axial z-direction, *i.e.* the direction of plume ascent, were used for encoding the vertical (v_z) motion of fluid passing through a horizontal cross section of the vessel. In different experimental runs, the position of this cross section could be selected to be various distances from the end of the capillary tube, thereby allowing for the examination of conduits at different locations. However, during an experimental run, the location of the horizontal cross section of interest remained stationary. Each image was acquired in 20 ms and images were acquired every 3 seconds. While data collection at a much higher rate was possible, image acquisition produces heat in the r.f. coil. It was therefore necessary to find a compromise between the image collection rate and the amount of residual heating of the reaction vessel by the r.f. coil. It was determined that 3 seconds was a sufficiently long interval to avoid such heating effects. The field of view of a velocity image was 70 mm × 70 mm with a slice thickness of 2.5 mm. The velocity encoding was done over a duration of 5.1 ms and the velocity field of view was 13.2 mm/s.

4.2 Results and discussion

In this section, we describe the flow profiles we observed, how a conical shape of the conduit emerges for the autocatalytic steady plumes, and how the morphology and velocity profiles of autocatalytic steady plumes compare to those found in non-reacting compositional plumes.
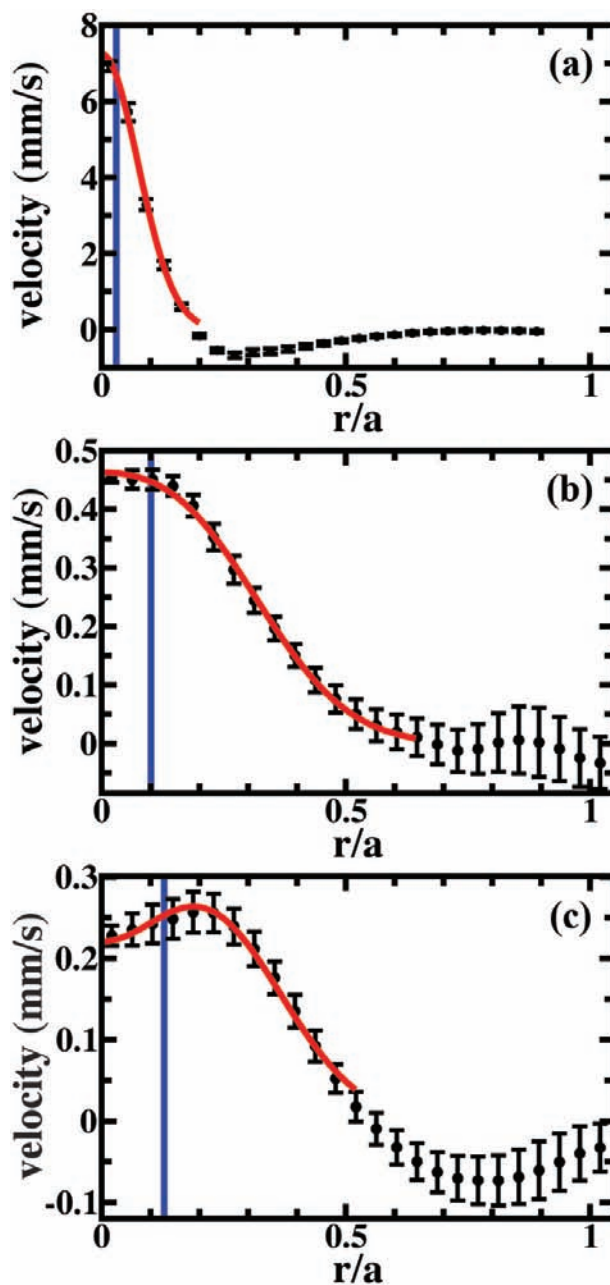
Figure 4.3: Averaged axial velocity profiles derived from MRI velocity images for a) a compositionally buoyant plume 10 cm from the capillary tube outlet produced by an injection flow rate of 2.0 mL/min, and an autocatalytic plume b) 10 cm from the outlet, and c) 15 cm from the outlet. r indicates the distance from the plume axis, and a is the radius of the glass tube. Vertical (blue) lines represent the location of the reaction front, or plume edge. The (red) curve in a) shows a Gaussian fit of the velocity data, and the (red) curves in b) and c) show axisymmetric bimodal Gaussian fits. Gaussian fits were performed only for positive velocity values. Negative velocities are due to the broad downwards return flow generated by the plume. The number of consecutive velocity images averaged for each profile were a) 36, b) 91, and c) 128, where each velocity image was 3 seconds apart.

4.2.1   Velocity profiles of plume conduits

Fluid velocities in the vertical direction were measured across horizontal cross sections of the reaction vessel at distances of 10 cm and 15 cm from the outlet of the capillary tube. A typical MRI velocity image of the vertical velocity profile for the conduit of a plume at 10 cm from the outlet is shown in Fig. 4.1. Each velocity pixel, or *voxel*, in the 64×64 data matrix represents a separate velocity measurement.

Using data obtained during the period of time in which the conduit maintained steady state flow, we radially averaged velocity images to obtain a characteristic velocity profile for a given height above the outlet. This was done by grouping voxels into annuli at various radii from the centroid of the positive components of the velocity distribution. Using the centroid of the plume velocity distribution to define the axis of symmetry of the plume rather than the centre of the pipe was necessary to account for the slow drift of the conduit in the x-y plane. This was caused by small drifts in the orientation of the down-going return flow in the unreacted fluid. Each annulus had a width of 1 voxel, which corresponds to ~ 1.1 mm, and all velocities found in a given annulus contribute toward the overall average for that annulus. Error bars were calculated from the standard deviations in these values. The velocity values for each annulus were averaged over time (*i.e.* over several successive velocity images) to obtain the velocity profile as a function of radius from the center of the plume. Using this method, typical velocity profiles obtained for autocatalytic and compositionally buoyant plumes are shown in Fig. 4.3. For comparison of the velocity profiles with composition profiles, conduits were produced in the standard plume apparatus used in Chapter 3 (Fig. 3.2) under the same conditions as in the MRI spectrometer, in which the concentration profile was captured with a CCD camera. Since a buffer was not used to control the concentration of hydrogen, congo red indicator could be used to visualize the location of the front of the hydrogen catalyst, which appear as shown in Fig. 4.2. Fig. 4.3bc shows the radius of the reaction front at each z position. These radii values were found by averaging the radius at each position for five experimental runs, and were found to be 2.9 ± 0.2 mm at $z = 10$ cm and 3.6 ± 0.1 mm at $z = 15$ cm.

It should be noted that in addition to measuring velocities, attempts were also made to make high resolution MRI measurements of the concentration profiles of reaction fronts. These measurements would have given simultaneous concentration profiles in addition to the velocity profiles that we obtained. Attempts to resolve concentration,

however, were unsuccessful, and therefore the location of the concentration fronts shown in Fig. 4.3bc were determined from additional experiments that occurred outside the MRI spectrometer.

Compositionally buoyant plumes were driven by continuously injecting 38% by volume glycerol solution into 40% glycerol solution, using injection flow rates in the range of 0.5 mL/min to 2.0 mL/min. In this range, the compositionally buoyant plumes were found to have Gaussian velocity distributions where the maximum velocity occurs along the axis of the plume, as shown in Fig. 4.3a. Such a velocity profile may be phenomenologically described by

$$u_z(r) = u_0 e^{-r^2/R^2}, \tag{4.1}$$

where u_0 is the maximum z component of the velocity above the origin at $z = 0$, r is the distance from the axis of symmetry of the plume, and R is the radial length scale of the velocity distribution [7]. By use of shadowgraphy, we also determined the edge of the concentration profile of the compositional plumes, which remains quite sharp compared to the velocity profile because of the large Schmidt number, Sc ~ 9000. In both compositional and autocatalytic plumes, the velocity profiles extend well beyond the plume edge because of the laminar shear created by the viscous entrainment between rising plume material and ambient fluid. Since the tube diameter is not infinite, continuity requires a $u_z < 0$ return flow, which the MRI velocimetry identifies near the outer edge of the tube. Only velocity values above zero were used in the Gaussian fits shown in Fig. 4.3.

For the compositional plumes, the velocity profile length scale R remained independent of z, and the plume conduit maintained its cylindrical shape. Consistent with this, the diameter of the concentration profile also remained constant. In such a plume, one would expect essentially no entrainment of the surrounding fluid into the plume conduit.

These simple features are different in autocatalytic conduits. Fig. 4.3b shows the velocity profile for an autocatalytic conduit at $z = 10$ cm from the capillary tube outlet. Here, velocities measured across the radius of the conduit remain almost as high as they do along the plume axis, significantly flattening its velocity profile. Farther up the pipe, at $z = 15$ cm, the velocity profile within the plume is no longer maximum near the conduit centerline, as shown in Fig. 4.3c. The velocity maximum is localized in the vicinity of the reacting front.

These new features are due to the continuous flux of buoyancy occurring along the

entire length of the conduit. The buoyancy flux comes from both the production of heat occurring at the reaction front located at the composition edge, and from the radial entrainment of reactant solution into the plume. This inward flux of reactant, which becomes product as it crosses the sharp reaction front, also creates a buoyancy flux due to its solutal composition change. This flux of buoyancy into an autocatalytic plume is in stark contrast to the role of entrainment of outer fluid into many types of non-reacting plumes, where entrainment modifies plume behaviour by enlarging them through the incorporation of denser fluid into their structure [12]. An example of a type of flow in Nature with positive feedback between entrainment and flow velocity (much like that in an autocatalytic plume) is a turbidity current. A turbidity current is a downhill flow of sediment in the ocean caused by gravity. When the turbidity current causes significant erosion as it flows, it can offset its dilution from the entrainment of water. In this scenario, positive feedback leads to more erosion and further acceleration [106].

The advance of the front combines with the upward fluid velocity to cause the conduit diameter to increase with z, giving the concentration profile a conical shape, as shown in Fig. 4.2e-f. This is in contrast to the constant diameter conduits that were observed for non-reacting, compositional plumes. When the diameter of the conduit is sufficiently large, the upward flow within the plume is fastest at its edge, and a minimum appears in the velocity profile along the axis.

The velocity profile of the more complex autocatalytic conduit can be phenomenologically described by a symmetric bimodal distribution of the form

$$u(z,r) = u_0[e^{-(r-\mu(z))^2/\sigma^2} + e^{-(r+\mu(z))^2/\sigma^2}], \tag{4.2}$$

where $\mu(z)$ is the radial distance between the axis of symmetry and the sharp chemical front. Clearly, the width σ of the maximum localized near the front must be related to the length scale over which the heat of the reaction is diffused, creating part of the buoyancy that drives the flow. As the conduit radius $\mu(z)$ becomes larger, it eventually exceeds this length, and the velocity minimum on the axis becomes apparent. The bimodal shape is a good phenomenological description of the velocity field of an autocatalytic plume because these plumes do not have a localized source of buoyancy. Rather, they have a distributed "sheet" source of buoyancy that exists all over the surface of contact between reacted and unreacted species. The entire conduit edge is a conical reaction front that provides buoyancy to the plume.

4.2.2   The conical shape of the concentration front

In separate indicator and shadowgraph experiments, for autocatalytic and compositional plumes respectively, the radii of the edge of the steady state plume conduits, such as the autocatalytic conduits shown in Fig. 4.2e-f, were determined as a function of z using image analysis. Fig. 4.4 shows a comparison. The autocatalytic conduit achieves a steady, approximately conical shape, characterized by a half-angle $\theta \approx 1.7°$, as determined by averaging the conical spreading of several plumes. The compositional conduit remains cylindrical.

The autocatalytic conduit attains a remarkable steady state, which is a balance between upward flow, buoyancy production, and the advance of the chemical front due to diffusion of the autocatalyst. The spreading of the conical conduit is sufficient to balance the front speed v and the upward hydrodynamic flow U, as shown in Fig. 4.5. For our reactant composition, the measured front speed in the absence of convection is $v = 9.9 \times 10^{-3}$ mm/s [3]. At this front speed, a half-angle of $1.7°$ should be achieved for $U = v/\sin\theta \sim 0.3$ mm/s. Typical upward velocities of fluid in an autocatalytic plume, as measured by MRI velocimetry, lie in the range of $\sim 0.2 - 0.5$ mm/s, in agreement with this simple picture.

4.3   Summary

We have described a study of the steady state plume conduits produced by the IAA reaction. We have quantified the flow profile and morphology of these conduits, and compared them to plume conduits produced by non-reacting glycerol-water mixtures. To examine the flow profile we used a dynamic MRI imaging sequence called GERVAIS to resolve vertical velocity components across a horizontal cross section of the pipe housing the rising plume. We found that the vertical flow across a chemical plume conduit may be phenomenologically described by an axisymmetric bimodal distribution, one that widens in accordance with the approximately uniform conical widening of the plume. This is in contrast to the Gaussian velocity distribution that describes flow across a non-reacting plume conduit that remains cylindrical. This finding shows that the buoyancy flux that drives the plume upward is created by the plume boundary, or reaction front. Such an

---

[3]Front speed in the absence of convection was determined by measuring a flat descending front in a vertical capillary tube. This experiment was discussed in Section 3.1.2. The inner bore of the tube was 3.0 mm, and it was placed inside a fluid jacket held at a constant temperature of 25.0°C.
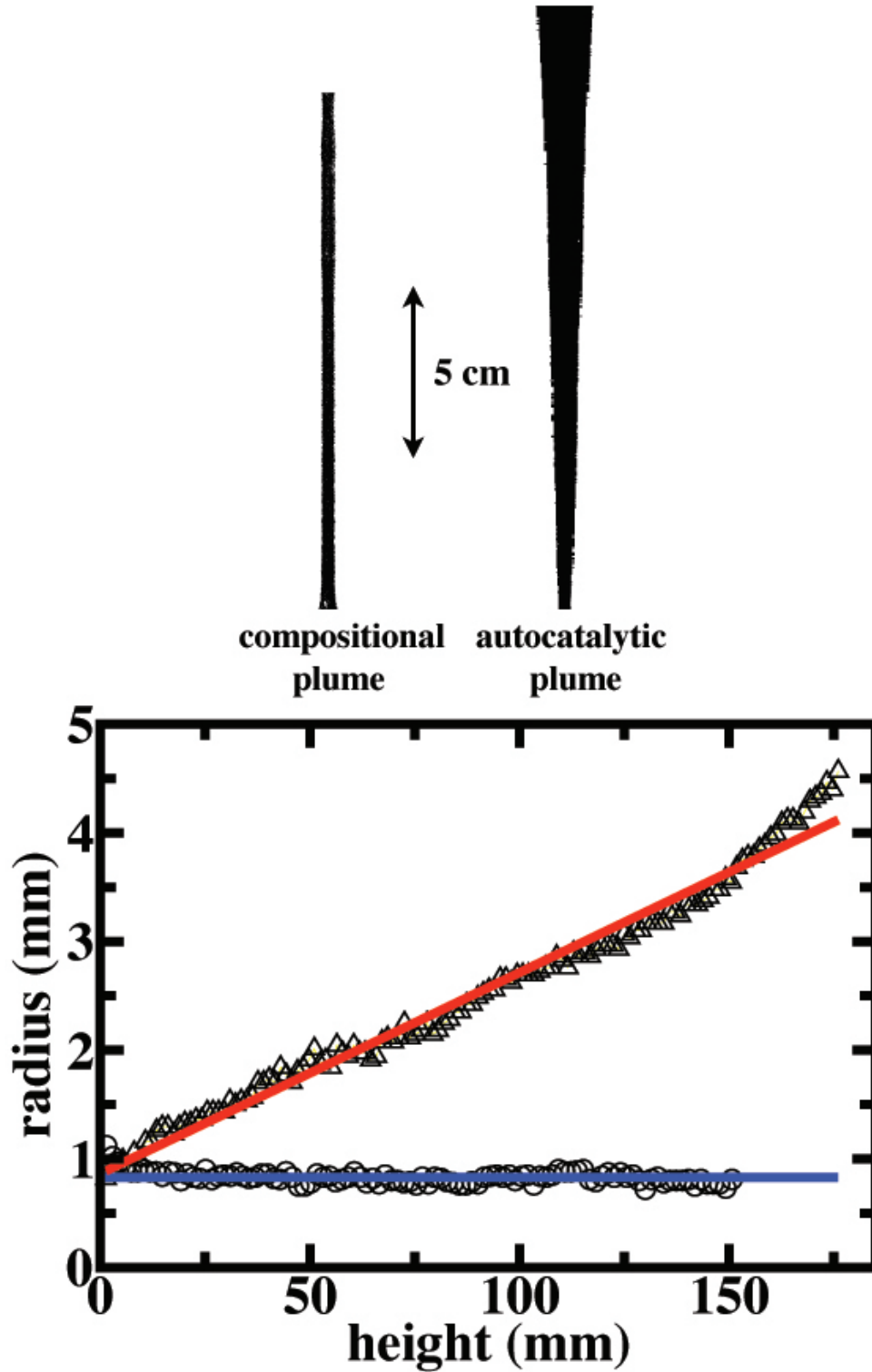
Figure 4.4: Top: The typical morphology of a compositional and an autocatalytic plume, obtained from image analysis of experimental data, shown to scale. Bottom: The radius of the autocatalytic plume ($\triangle$) and compositional plume ($\bigcirc$), and their lines of best fit, as a function of height from the capillary tube outlet.
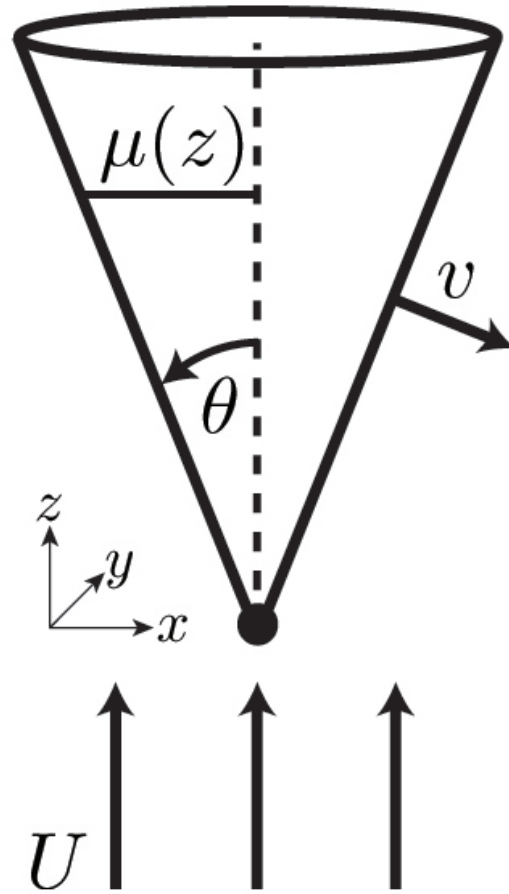
Figure 4.5: A simple geometrical model of an autocatalytic plume conduit. The cone half-angle is θ, the radius of the cone as a function of distance above $z = 0$ is $\mu(z)$.

addition of buoyancy by means of entrainment is unique to IAA chemical plumes, since entrainment of ambient fluid in a non-reacting system incorporates less buoyant fluid into the plume. This creates a unique scenario whereby the source of buoyancy for an autocatalytic plume is distributed along the entire plume boundary, in contrast to the sole localized bouyancy source for non-reacting plumes.

Chapter 5

Numerical simulations of autocatalytic plumes

Chapters 3 and 4 focused primarily on the study of autocatalytic chemical plumes. Starting plumes were discussed in Chapter 3, while steady plumes were the focus of Chapter 4. In each of these Chapters, simple models were constructed in order to explain the ascent velocity of the starting plume and the conical shape of steady conduit. In this Chapter, we develop and test a much more sophisticated model in which we use computational fluid dynamics to simulate autocatalytic chemical plumes.

The computational fluid dynamics simulation of autocatalytic plumes is capable of producing detailed concentration, temperature, pressure, and velocity fields. The purpose of this model is to gain understanding of the dynamic interplay between these fields and how they contribute to autocatalytic plume behaviour. For autocatalytic starting plumes, our experimental results have been limited to an exploration of the concentration field only, and only in a "one-bit" sense - the acid-base indicator enabled us to visualize the location of reactant and product, but not variations in their concentrations. Velocities were measured across the conduit of steady autocatalytic plumes using dynamic MRI, however at any given instant in time only the velocities in a horizontal cross section of the fluid could be determined.

In addition to plumes, we also use our simulation to explore the evolution of buoyant autocatalytic "flame balls", which are spherical balls of reacted fluid. In these simulations, flame balls are placed in an initially quiescent environment. Under the influence of gravity, buoyancy then causes them to rise as viscous forces deform their initially spherical shape. As discussed in Chapter 3, shortly after an autocatalytic plume begins to

form, it forms a small spherical head. Depending on the size of the head relative to the cylindrical conduit below it, the velocity of the head can ascend like a growing sphere. Autocatalytic flame balls are therefore closely related to plumes in the sense that their initial conditions are very similar, the difference being that autocatalytic flame balls are initiated far from any boundary, and therefore they are not attached to a fixed "source" like a plume.

The contents of this Chapter are organized as follows. In Section 5.1, we provide details about the formulation of the simulation. In Section 5.2, we explore the effects of mesh size and time step on the simulation results. Section 5.3 discusses simulation results for reaction fronts in very thin tubes. Simulation results for autocatalytic chemical plumes are examined in detail in Section 5.4, and Section 5.5 is devoted to autocatalytic flame balls. A summary follows in Section 5.6.

5.1 Simulation formulation

5.1.1 System description

The simulation is constructed by assuming that autocatalytic plumes are axisymmetric, with the axis of symmetry aligned with the gravitational field. The three-dimensional problem can then be reduced to two dimensions by describing plume motion in cylindrical coordinates. A sketch of the relevant dimensions for the simulation is shown in Fig. 5.1. Since the IAA reaction is exothermic in addition to producing an isothermally buoyant product, we employ two separate Rayleigh numbers to quantify these effects. The thermal and concentration Rayleigh numbers, first introduced in Section 1.2, are

$$\mathrm{Ra}_T \;=\; \frac{g\alpha L^3}{\nu D_c}\Delta T \;\; \text{and} \;\; \mathrm{Ra}_c = \frac{g\beta L^3}{\nu D_c}\Delta c \; . \tag{5.1}$$

$\Delta T = T - T_0$ and $\Delta c = c - c_0$ are the temperature and concentration differences across the reaction front, α and β are the thermal and compositional expansion coefficients, ν is the kinematic viscosity, D_c is the diffusion constant of the autocatalyst, and L is the length scale. Here, we choose L to be the diffusion length of the front, which is defined by $\ell = \sqrt{D_c\tau}$. We calculated ℓ by measuring the front velocity, v_f, in the absence of convection (see Section 3.1.2), and by using $v_f = \sqrt{D_c/\tau}$ and $\tau = \ell/v_f$. For a 40% glycerol solution, $v_f = 9.9 \times 10^{-4}$ cm/s and $D_c = 4.2 \times 10^{-10}$ m^2/s, which gives $\tau = 4.3$ s
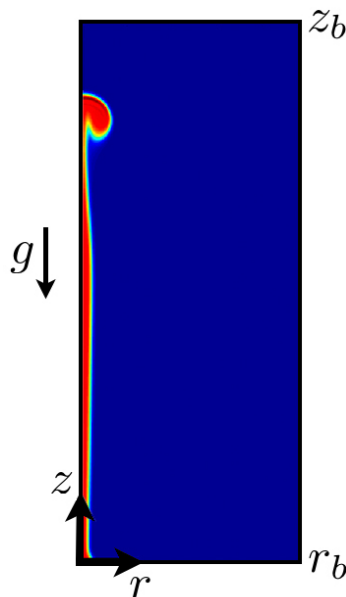
Figure 5.1: A sketch of the cylindrical coordinate system used, along with a concentration field for a plume produced by the simulation.

and $\ell = 4.2 \times 10^{-3}$ cm. These values, along with $\alpha = 4.3 \times 10^{-4}$ K^{-1}and $\Delta T = 0.5$ K [4], give $\text{Ra}_T = 0.10$ and $\text{Ra}_c = 0.17$, which were the Rayleigh number values used in all of our simulations.

In the simulation, we assume that the density change from reaction is linearly dependent on changes to both c and T. By nondimensionalizing c by its maximum value, fully reacted fluid has a product concentration of $c = 1$, and fluid absent of any product solution has $c = 0$. The temperature change from reaction, $T - T_0$ is scaled by $\Delta T = -\Delta H \Delta c / \rho_0 C_p$, which bounds T as $0 \leq T \leq 1$. ΔH is the heat of reaction and is negative for the exothermic reactions, C_p is the constant pressure specific heat of the solvent. Since the solution initially free of product has $c_0 = T_0 = 0$, we have $\Delta c = c$ and $\Delta T = T$. This gives it the density dependence

$$\rho(c, T) = \rho_0[1 - \alpha T - \beta c]. \tag{5.2}$$

Using the assumptions we have stated above, and quantifying the effects of buoyancy as we have in Eq. 5.1, the dimensionless equations that describe the system are similar to equations that describe chemo-hydrodynamic flow in a thin vertical slot with infi-

---

[4]Estimated from values available in Refs. [65, 83]

nite dimensions [67, 45]. In the Boussinesq approximation, the dimensionless equations describing our system are

$$\nabla \cdot \mathbf{u} = 0, \tag{5.3}$$

$$\frac{1}{\text{Sc}} \frac{D\mathbf{u}}{Dt} = -\nabla p + \nabla^2 \mathbf{u} + (R_T T + R_c c)\mathbf{e}_z, \tag{5.4}$$

$$\frac{Dc}{Dt} = \nabla^2 c + F(c). \tag{5.5}$$

and

$$\frac{DT}{Dt} = \text{Le}\nabla^2 T + F(c). \tag{5.6}$$

The continuity Eq. 5.3 is reduced to incompressible form, and the nondimensionalized Navier-Stokes equation has $\mathbf{e}_z$ as the unit vector pointing in the z-direction, with p denoting the pressure. The pressure calculated by the simulation is dimensionless, and it represents a difference in pressure between the quiescent fluid and the fluid when it is in motion, rather than the absolute pressure, which would vary with the depth of fluid. The reaction-diffusion-convection equation (Eq. 5.5) and the energy balance (Eq. 5.6) both incorporate the cubic autocatalytic reaction rate term

$$F(c) = c^2(1 - c), \tag{5.7}$$

This term was first introduced in dimensional form in Eq. 1.24, however as a consequence of the nondimensionalization of our system, here it appears without rate constant k_c. Sc=ν/D_c and Le=κ/D_c, where κ is the thermal diffusivity, are the Schmidt and Lewis numbers, respectively. The parameter values used for our simulation are Sc=9.0×10^3 and Le=2.8×10^2, which were calculated in Section 3.2.2.

As shown in Fig. 5.1, the cylindrical dimensions are bounded by $\sigma = r_b$ and $z = z_b$. The boundary conditions are no-slip for the velocity field, and there is no flow of energy or chemical species across the boundary. These conditions are expressed as

$$\mathbf{u} = \frac{\partial \mathbf{T}}{\partial \mathbf{r}} = \frac{\partial \mathbf{c}}{\partial \mathbf{r}} = \mathbf{0} \tag{5.8}$$

at $\sigma = r_b$, and

$$\mathbf{u} = \frac{\partial \mathbf{T}}{\partial \mathbf{z}} = \frac{\partial \mathbf{c}}{\partial \mathbf{z}} = \mathbf{0} \tag{5.9}$$

at $z = 0$ and $z = z_b$.

In the following Sections, when presenting data from the concentration, temperature,

pressure, and velocity fields, we reflect the fields across the axis of symmetry, giving the data the appearance of a plume. When this is done, data from the simulation is shown along the positive direction in σ, and its mirror image is shown in the negative σ direction. We also calculated vorticity fields from the u and v velocity fields. Vorticity is defined as

$$\boldsymbol{\omega} = \boldsymbol{\nabla} \times \mathbf{u}. \tag{5.10}$$

Negative values of vorticity therefore appear for clockwise fluid motion, and positive values for counter-clockwise motion in the rz-plane. Across the axis, plumes should therefore have opposite vorticity fields. For this reason, when we present vorticity data, it is not reflected across the axis as it is for the other fields.

5.1.2 Initial conditions

All plume simulations are initiated in a quiescent solution of reactant fluid with $c = T = 0$. Plumes were initiated using product solution geometries with either a sphere on top of a cylinder or simply a sphere. For the sphere-cylinder initial condition, a small cylinder of product solution with radius r_{c0} and initial concentration and temperature values of $c_0 = T_0 = 1$, is placed along the axis of the cylindrical geometry, at $\sigma = 0$. In some cases, $c_0 = T_0 < 1$ was also used. The bottom of the cylinder starts at $z = 0$, and the cylinder extends up into a small sphere of product solution whose center is located at $z = Z_0$. The sphere is given an initial radius r_{s0}, and initial concentration and temperature values equal to that of the cylinder. Spheres located just above the bottom boundary were also used to initiate plumes, and spheres well above the bottom boundary were used for autocatalytic flame ball simulations. In some cases, the concentration and temperature profiles at edge of the cylinder and the sphere (or just the sphere), were smoothed. This was done in order to avoid a steep gradient across the initial reaction front. To smooth the temperature front of the cylinder, the following smooth approximation of the step function is used to define T_0 in the region $0 \leq r \leq r_{c0}$,

$$T_0(r) = \frac{1}{2}(1 - \tanh(\zeta(r - r_{c0}))), \tag{5.11}$$

where ζ is a constant bounded by $0 \leq \zeta \leq 1$. The initial concentration front is defined the same way as the initial temperature front, so $c_0(r) = T_0(r)$. A typical value used for constructing our initial conditions was $\zeta = 0.5$. For initial conditions $c_0 = T_0 = 1$,

this gives the front a smooth transition from $c = T \sim 1$ to $c = T \sim 0$ across a length of $\sim 10\ell$ centered about r_{co}. This is similar to the width of the reaction front. Centered at $c = 0.5$, spanning a length of $\sim 10\ell$ the reaction front has a concentration range of $0.05 \leq c \leq 0.95$, and over a length of $\sim 15\ell$ the concentration range is $0 \leq c \leq 1$. An equation similar to Eq. 5.11 was used to smooth the initial spherical fronts as well.

Other initial conditions were also explored, such as a disk with $c = T = 1$ at $z = 0$. Initial conditions starting with disks at $z = 0$ did not produce plume behaviour that resembled experimental data as closely as spherical initial conditions. In addition, the disk initial conditions took much longer to develop into a plume than a sphere or the sphere-cylinder geometries, wasting valuable computational time. Therefore, runs with these initial conditions will not be further discussed.

5.2   Mesh spacing and time-step selection

The algorithm we used for our simulation is known as the SIMPLE (Semi-Implicit Method for Pressure Linked Equations) method [107, 108]. The SIMPLE method involves advancing the Navier-Stokes equation in time using an implicit numerical method. Implicit numerical methods use iterative techniques to solve coupled sets of equations, where the equation solutions are defined by the current state of the system and a future state. This is in contrast to solving for a future state of a system using only known quantities from the present state, which is how explicit numerical methods operate.

For computing the unsteady flow of an autocatalytic starting plume, both space and time are discretized. In our simulation, space is discretized by a uniformly distributed mesh of grid points, or nodes. The nodes are the locations at which the values of the dependent variables are solved. Each node is separated spatially by Δr in the radial direction and Δz in the vertical direction, where $\Delta r = \Delta z$. While meshes for the dependent variables of the system have the same node spacing, the locations of the nodes do not necessarily coincide for all variables. Instead, the nodes for some of the system variables are organized in a staggered arrangement. Pressure, temperature, and concentration are all on the same mesh, while in between the nodes of this mesh, and on their own separate meshes, are the nodes for the two velocity components u (σ component) and v (z component). This is done so that there is a strong coupling between the velocities and the pressure, which helps avoid convergence problems in these fields [108]. For all of our simulations, we limited the node spacing so that $\Delta r = \Delta z \leq \ell$. The diffusion

length of the autocatalyst, ℓ, was selected as the maximum grid spacing because it is the smallest length scale in the problem. Node spacing of this size is necessary to be able to resolve changes in the concentration fields across the reaction front. Were it not for the sharp change in concentration across the reaction front, the spacing of the nodes could be made much larger.

In the same way that space was discretized, time must also be discretized. This is done by stepping time forward in discrete amounts called time steps, denoted as Δt. All values of Δt are expressed in units of τ. A typical value of Δt used in our simulations was $\Delta t = 0.005\tau$. If Δt used for the simulation is excessively large, the solutions of transient behaviour can be inaccurate. The smaller Δt is, however, the more computationally expensive it is to let the solutions evolve in time. In Section 5.2, we describe our efforts to find appropriate values for Δr, Δz, and Δt for the simulation.

5.2.1 Minimizing instabilities in the concentration field

The concentration gradient across the reaction front is the steepest of any gradient calculated in the solution fields. As the simulation algorithm marches forward in time, the advection of this steep gradient in concentration must be resolved, and it is across the front that numerical instabilities in the concentration field develop. With minimizing these instabilities in mind, we explored the effects of adjusting the mesh spacing and time step on simulation results. Since $\Delta r = \Delta z \leq \ell$, we define the resolution factor

$$\sigma = \frac{\ell}{\Delta r} \tag{5.12}$$

to express changes in the mesh spacing. The coarsest mesh is $\sigma = 1$, and as σ increases, so does the resolution of the concentration, temperature, pressure, and velocity fields.

Figure 5.2 shows the concentration fields, and the concentration field values along $r = 0$, for chemical plume simulations with $\sigma = 1$ and $\sigma = 4$. Both simulations used the equivalent smoothed sphere-cylinder initial condition, with $r_{c0} = 34\ell$ and $r_{s0} = 40$ and $c_0 = T_0 = 0.99$. The center of the sphere was initially placed at $z = 180\ell$, and the spatial dimension used for each simulation was $r_b = 160\ell$ and $z_b = 640\ell$. The most striking difference between the two fields is the presence of large scale oscillations in the concentration field for the $\sigma = 1$ simulation. The oscillations occur across the concentration gradient created by the reaction front, and they attenuate behind the

front, where the concentration well behind the front reaches a stable value of $c = 1$. The oscillation causes a concentration spike that occurs right at the front, where the maximum value of $c = 1.0990$ occurs. Since physically, c is supposed to be bounded by the values 0 and 1, and since such oscillations do not occur in reality, attempts were made to remove this undesirable numerical artifact.

Many measures were taken to reduce the oscillations in the concentration, with the hope of eliminating them entirely. These included making adjustments to the initial conditions, exploring the effect of changing the time step, and altering the resolution of the mesh. As Fig. 5.2 shows, the sensitivity in the solutions for the concentration field across the reaction front is considerably reduced by increasing σ. For $\sigma = 4$, a very small spike in the concentration occurs across the reaction front, with a value of $c = 1.0029$. This concentration spike is approximately two orders of magnitude less than the peak value for the $\sigma = 1$ run, a significant improvement. According to our results for simulations with variations in time step only, changes in the time step did nothing to reduce the effect of oscillations. Smoothing of the reaction front in the initial conditions also yielded only a marginal improvement, and only for results not long after initiation. Initial conditions with steep gradients in the concentration concentration field, such as a sphere with $c = 1$ surrounded by fluid with $c = 0$, produced oscillations earlier in the evolution of the plume than spheres with smoothed edges. However, spheres with smoothed edges would eventually give rise to oscillations as the sphere began to rise and the gradient across the leading edge of the ascending front increased.

Despite the difficulty to rid the system of concentration oscillations across the front, the large scale dynamics of the simulated plumes were barely affected by their presence. This can be seen by comparing the temperature and vorticity fields of the $\sigma = 1$ and $\sigma = 4$ plumes shown in Fig. 5.3, which are very nearly identical. These fields are for the same point in the plume evolution shown in Fig. 5.2. The biggest difference in any field other than the concentration was found in the temperature fields. Figure 5.4 shows the temperature fields along $r = 0$, the axis of symmetry of the plumes. The greatest difference between the two temperature fields occurs at the leading edge of the plume, where the $\sigma = 4$ temperature field is much smoother than the sudden jump in the $\sigma = 1$ field. Other than the slight temperature differences near the front, the temperature fields along $\sigma = 0$ are very nearly identical. The velocity and pressure fields for the $\sigma = 4$ and $\sigma = 1$ fields, however, are essentially identical at all grid points. Thus, while oscillations in the concentration field across the front are not a desirable effect, they clearly do not

Figure 5.2: a) The concentration field for an autocatalytic plume simulation with mesh resolution of $\sigma = 1$. The results shown are for time 6.5τ. z and r are expressed in increments of ℓ. Left: an image of the entire concentration field. Right: The concentration oscillations across the reaction front along the axis of symmetry of the plume. b) Shows the same data as in a) for a mesh resolution of $\sigma = 4$ where the oscillations in the concentration field occur on a much smaller scale.
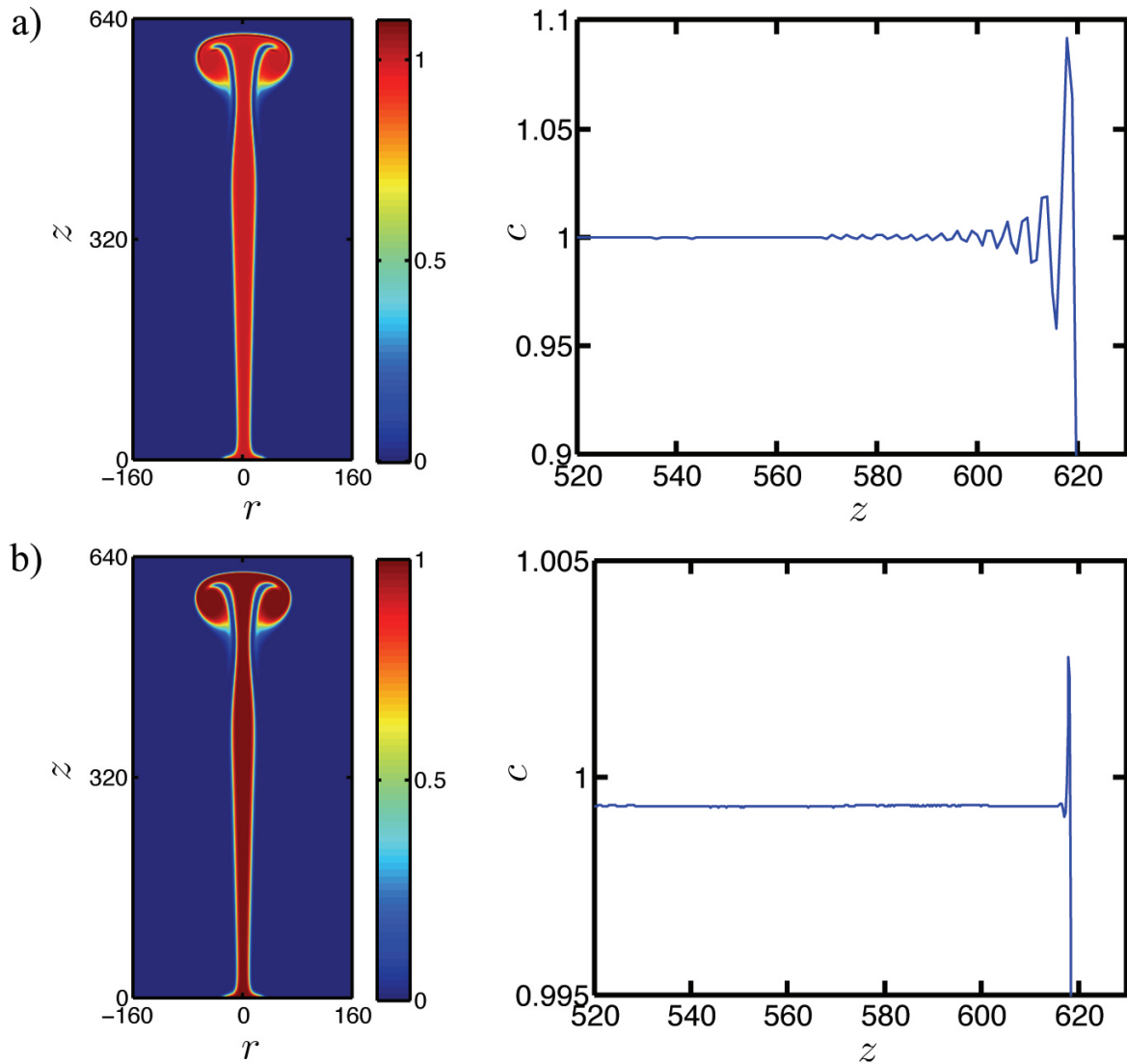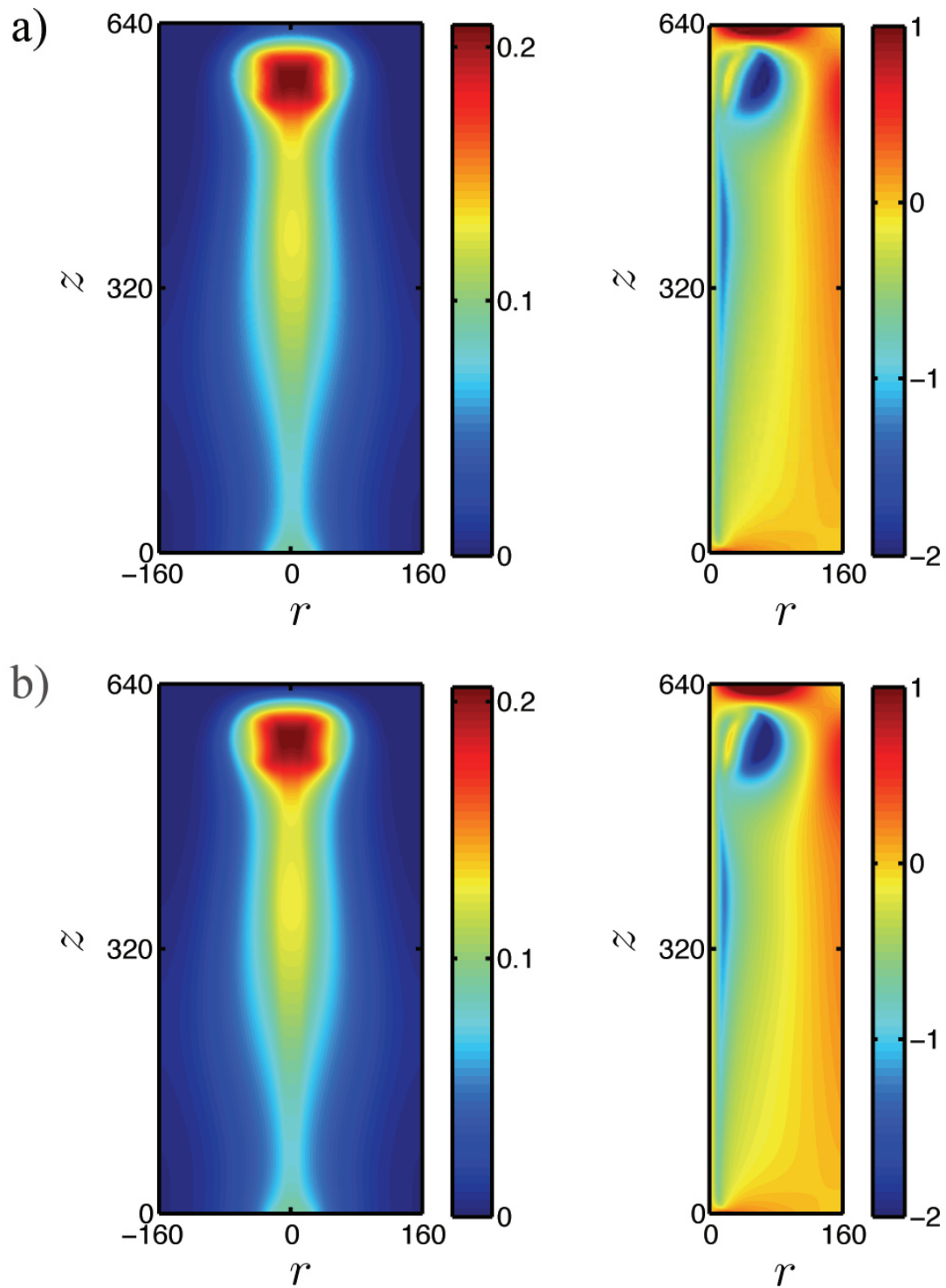
Figure 5.3: a) The temperature field (left) and the vorticity field (right) for an autocatalytic plume simulation with a mesh resolution of $\sigma = 1$. The results shown are for time 6.5τ. b) Shows the same data as in a) for a run with $\sigma = 4$.

have a catastrophic effect on the larger scale plume dynamics, even for coarse mesh ($\sigma = 1$) simulations.

While values of $\sigma = 4$ or higher were needed to quench the concentration oscillations as much as possible, the computational expense of running simulations for spatial domains comparable to those of our plume experiments at these mesh resolutions is considerable. The computational burden of running simulations at high resolution was eased by parallelizing our algorithm. The serial version of our simulation uses a single processor to calculate solutions on all nodes in the spatial domain. The parallel version, on the other hand, divides the spatial domain equally into a stack of smaller vertical domains, which we will call "slices". Each slice is assigned its own computer processor, which is responsible only for the solutions on the domain of the slice. The computational task is therefore divided amongst numerous processors working in parallel with each other, each computing solutions for a single slice. Between each time step, processors communicate information to the other using MPI (Message Passing Interface). This ensures that solutions in different slices make physical sense once data from all slices is combined to form a solution for the entire domain.

All parallel simulations were performed on computer clusters available through SHARCNET (Shared Heirarchical Academic Research Computing Network). Despite the improvements in simulation time afforded by using up to 64 processors working in parallel, high resolution simulations for large spatial domains still came at significant computational expense. As an example, it took 64 processors one week to simulate the first 97.5τ (~ 420s) of a plumes evolution in a spatial domain of $r_b = 240\ell$ and $z_b = 2240\ell$ at a resolution of $\sigma = 2$ (giving a mesh with size 480×4480 mesh points). This spatial domain corresponds to a physical space with $r_b = 1.0$cm and $z_b = 9.4$cm, which is much smaller than the dimensions of the experimental apparatus. In order to simulate the entire life of a plume in a domain size comparable to the physical size used in our experiments, many of our simulations were therefore carried out at less than ideal resolutions. As we have outlined above, however, the problem that this causes with concentration fields does not invalidate the large scale flow calculated for the plume. It should also be noted that results from the serial version of our simulation match almost exactly with those obtained from the parallel version. This was determined by comparing serial and parallel solutions for the same σ values, which showed that differences in results are typically very small, as shown in Figs. 5.3 and 5.4, and that these differences remain small and do not cause divergence in plume behaviour. For the plumes shown in Fig 5.2, the $\sigma = 1$
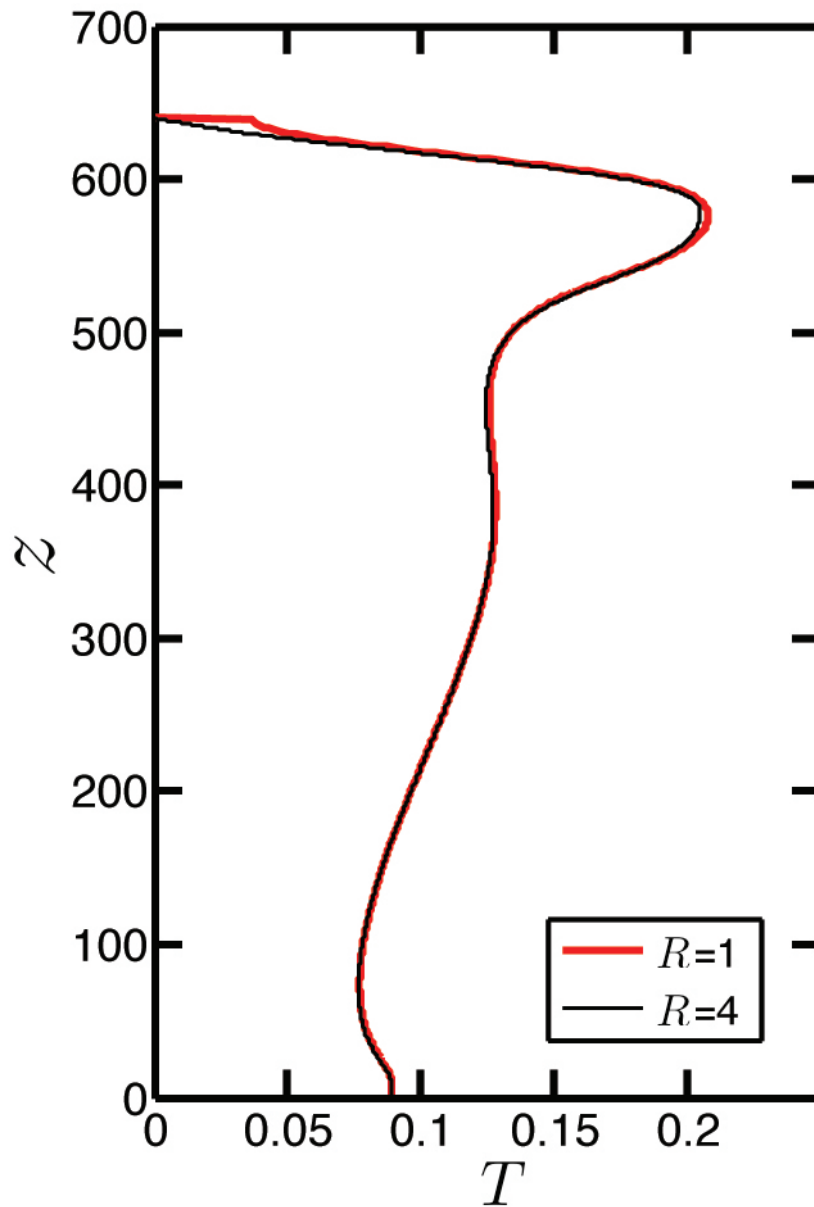
Figure 5.4: The dimensionless temperature profile along the plume axis, $r = 0$, for plumes with resolution $\sigma = 1$ and $\sigma = 4$. z is in multiples of ℓ. Note the very small discrepancy near the leading edge of the plume.
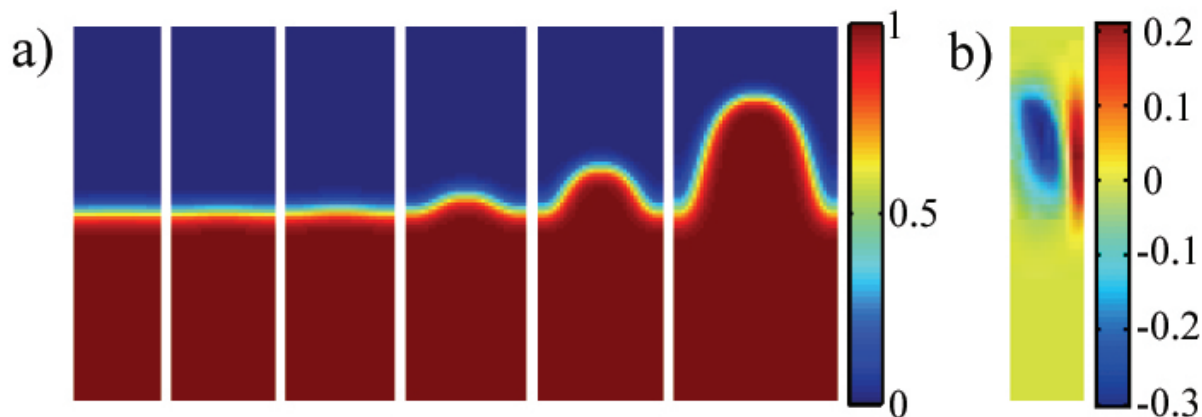
Figure 5.5: a) Concentration fields showing the shape of the reaction front for various tube radii. From left to right, the tube radii are 10, 12, 13, 14, 15, and 20ℓ. The vertical dimension for all images is 100ℓ, and each image is from 250τ after initiation. b) The vorticity field for the 20ℓ front shown in a). showing buoyancy-driven fluid motion in the vicinity of the front.

plume was calculated using a serial simulation, while the $\sigma = 4$ was calculated in parallel using 32 processors.

5.3 Thin tube simulations

In Section 3.1.2 we examined the ascent and descent of reaction fronts in a very thin capillary tube. When convection was not suppressed by the viscosity of the solution, ascending reaction fronts took on a fixed convex shape. For descending fronts and ascending fronts where convection was suppressed by viscosity, the shape of the front was flat. When convection of an ascending front is suppressed in a thin tube, it can occur for the same viscosity fluid in a slightly larger tube. We examined this phenomenon using our simulation as a simple test case. Indeed, we found in our simulations that beyond a certain tube radius, an IAA reaction front will deform due to the presence of convection. Below this radius, convection is suppressed, and the front remains flat, as observed experimentally (see Section 3.1.2).

The concentration fields for reaction fronts in thin tubes of various radii are shown in Fig.5.5a. These runs were performed in spatial domains with $z = 500$, and the reaction fronts were initiated by disks with $c = T = 1$ at the bottom of the spatial domain. The disks were the full width of the tube. The spatial resolution was $\sigma = 1$. Fronts in

tubes with $r_b \leq 13\ell$ all had fronts that remained flat and propagated with the same front velocity. For tubes with $r_b > 13$, however, fronts deformed into a convex curve, indicating the presence of convection. The convection driven flow creates a vorticity field such as the one shown in Fig.5.5b for a front in a tube with $r_b = 20$. As the fronts deformed, their velocity increased until their stable shape was reached. At this point the shape of the fronts remained the same and their velocity reached a constant value, as shown in the progression of the height of the fronts in Fig. 5.6. Above the onset of convection, increasing the value of r_b increased both the velocity and the curvature of the front. As a consequence of the viscous interaction of the convective flow with the boundary, flow velocities in thin tubes are substantially lower than those achieved by plumes. Since high flow velocities create oscillations in the concentration field, even coarse grid simulations of thin tube flows are sufficient to keep the concentration field in the range $0 \leq c \leq 1$.

The imposed axisymmetry on our simulated flow is an important difference between the simulation and the physical system. Since asymmetric flow patterns cannot be produced by our simulation, the asymmetric mode of convection shown in Fig. 1.2 and observed in experiments [59] and other simulations [87, 47] cannot be reproduced. The asymmetric mode of convection occurs for values of S (defined in Eq. 1.16) just above the critical value for the onset of convection, S_c. For larger values of S, the convective state forms an axisymmetric reaction front, which our thin tube simulations were able to reproduce.

Converted to dimensional units, the velocity of the flat fronts is $v_f = 6.9 \times 10^{-4}$ cm/s. This is less than the experimentally determined value of $v_f = 9.9 \times 10^{-4}$ cm/s for a front in fluid with the same parameters as those used for the simulations. It is possible that this difference can be attributed to possible errors in the experimental measurements used to calculate the fluid parameters and Ra numbers used for the simulation. An additional possibility is the effect that temperature change has on the diffusion constant. While the diffusion of the autocatalyst occurs at a fixed value in the simulations, in reality the diffusion of the autocatalyst is enhanced by heat generation around the front. Since the reaction is exothermic, the diffusion constant in a localized region around the front is increased, in turn increasing the front velocity. Furthermore, it is important to note that while our thin tube simulations take place in tubes that have r_b similar to our experimental thin tube radius, they should not be considered to be a direct simulation of our experimental system. The reason for this lies in the difference in the experimental boundary conditions and those used for our simulation. In the simulation, no heat flows

across the boundary, and therefore all of the heat in the system remains in the fluid. For a fluid-jacketed capillary tube experiment, however, heat produced by the reaction is lost through conduction with the glass walls of the capillary tube, which is then transferred to the circulating fluid. The equivalent experimental system would therefore have insulating walls housing the traveling reaction front.

Despite the discrepancies noted between the experimental and simulation boundary conditions, the general behaviour of reaction fronts in thin vertical tubes corresponds well with what is expected. This confirms that at the very least the simulation is capable of reproducing the essential behaviour expected of convecting autocatalytic fronts. In the following Section, we explore the simulations ability to reproduce the fundamental behaviour of autocatalytic plumes. These simulations occur in a much larger cylindrical spatial domain, and since the plumes do not have direct contact with the boundary, the discrepancies between the boundary conditions in the experiment and the simulation discussed above are irrelevant.

5.4 Simulation of autocatalytic chemical plumes

5.4.1 Starting plume morphology and ascent

The fluid parameters used for the model are those measured or calculated for a reactant solution in 40% glycerol. The evolution of the morphology of simulated plumes should therefore be consistent with the experimental observations of 40% glycerol plumes from Section 3.2.1. Below we show that this is indeed the case; simulated autocatalytic plumes produce accelerating plumes heads that pinch-off from the conduit. The c, T, p, and ω fields of a starting plume are shown in Fig. 5.7. Note the similarity of the concentration field with the experimental plume shown in Fig. 3.3c. The initial conditions for the simulation are a spherical product with $r_{s0} = 15\ell$ with $c_0 = T_0 = 1$. The sphere was placed just above the bottom boundary so that its center is initially located at $z_0 = 16\ell$. The spatial domain used for the simulation is $r_b = 500\ell$ and $z_b = 2000\ell$ resolved with resolution $\sigma = 1$, and the time step is $\Delta t = 0.005\tau$. Converting the units of the spatial domain to real units, it has a radius of 2.1 cm with a height of 8.4 cm. These dimensions are approximately one half of the corresponding dimensions of the experimental apparatus.

The concentration field in Fig. 5.7 shows a plume with a similar morphology to the
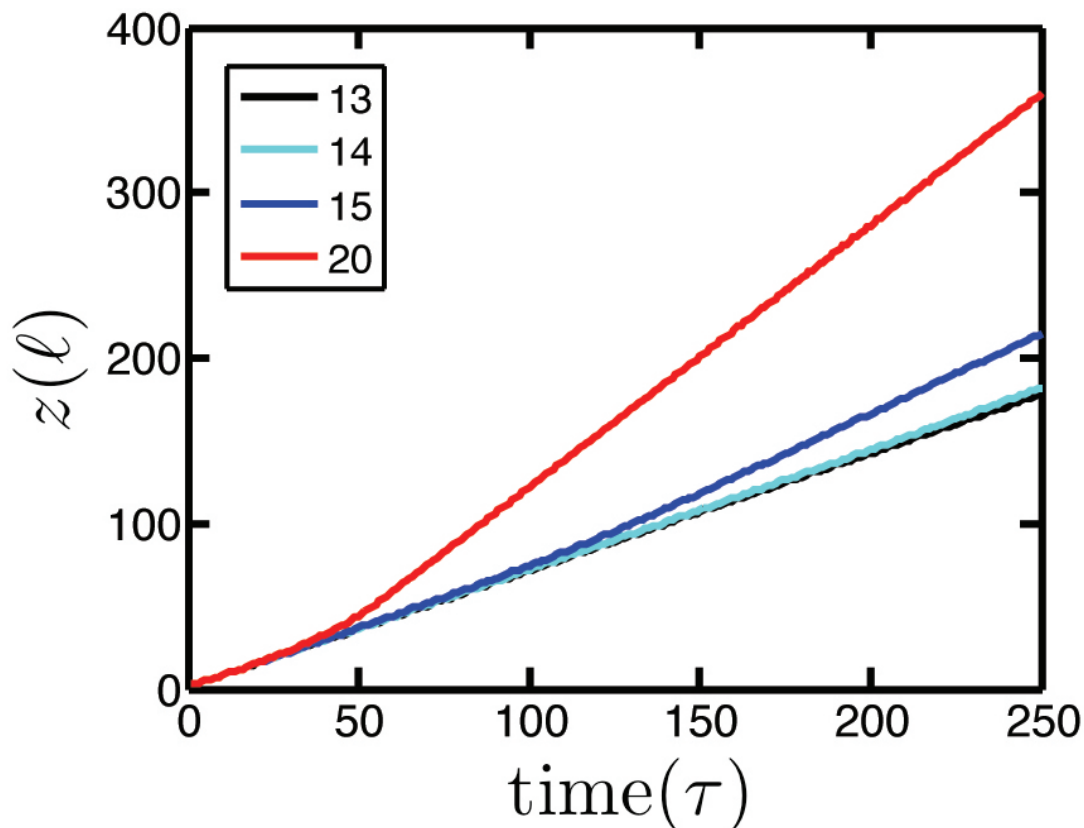
Figure 5.6: The upwards progression of the leading edge of the front in thin tubes with different r_b. The r_b used to produce the data in each curve is given in the legend in units of ℓ. As r_b is increased, so is the velocity of the ascending front. Note that the curvature in the lines shown occurs as the front makes a transition from flat to its stable, curved shape. Once it reaches a stable shape, the relationship between z and ℓ becomes linear.

experimental plume shown in Fig. 3.3c. In this stage of the evolution of the plume, it has already undergone the pinch-off process and a new, second generation head has started to form. The simulated plume arrived at this stage of evolution by stepping through the stages of evolution outlined for experimental plumes in Section 3.2.1. Each of these stages of growth correspond with one of the three regimes of plume head growth shown in Fig. 3.4a. The three regimes of head growth were also displayed by the simulated plume, as shown in Fig. 5.8a. To reiterate, each head growth regime can be described as follows. The growth regime is the slowest, when sufficient vorticity is not produced in the head to produce a vortex ring that entrains fresh reactant within its structure. Increased head growth is seen in the second regime, where buoyancy in the head is increased by vortical motion on the now clearly distinguishable vortex ring. The third
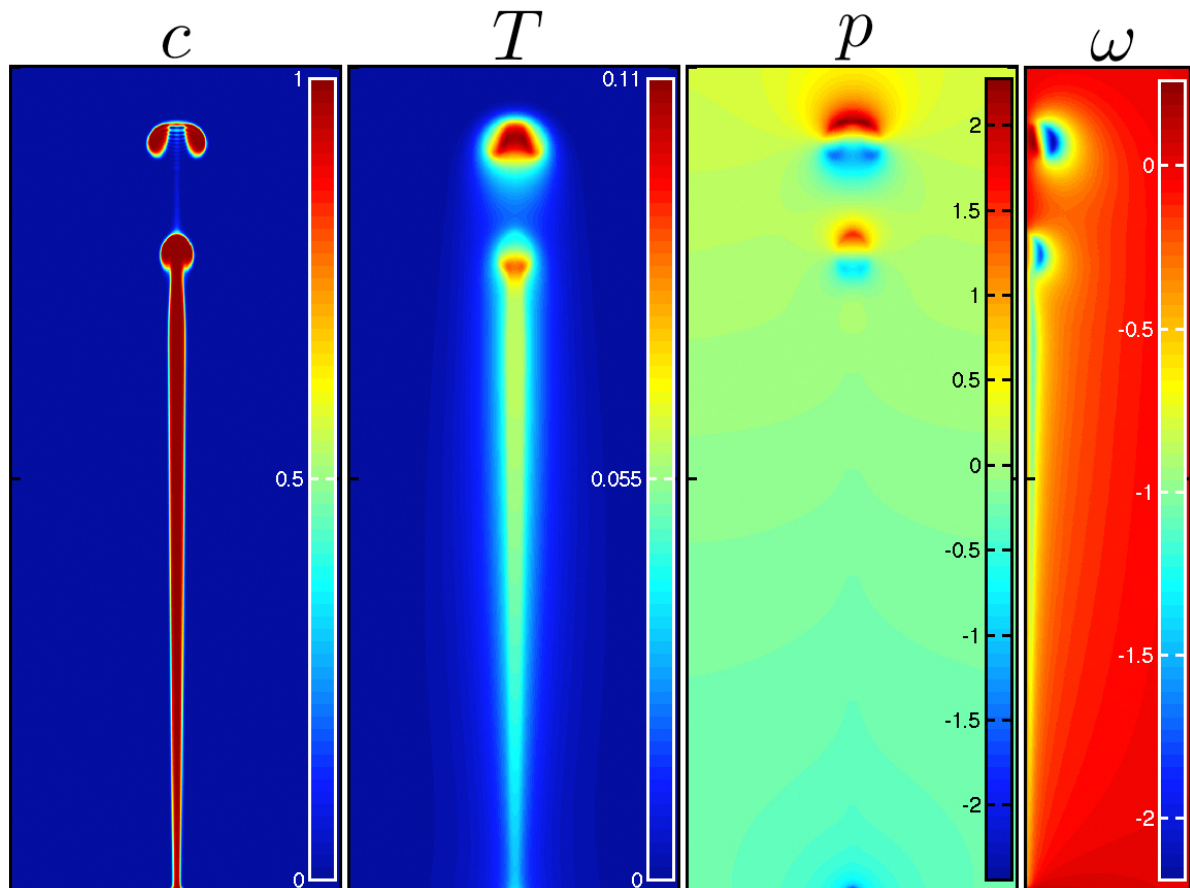
Figure 5.7: From the left: concentration, c, temperature, T, pressure, p, and vorticity, ω, fields for an autocatalytic plume that has pinched-off. The spatial domain for the simulation was $r_b = 500\ell$ and $z_b = 2000\ell$, only data in the space bounded by $\sigma = 300\ell$ and $z = 1500$ is shown.
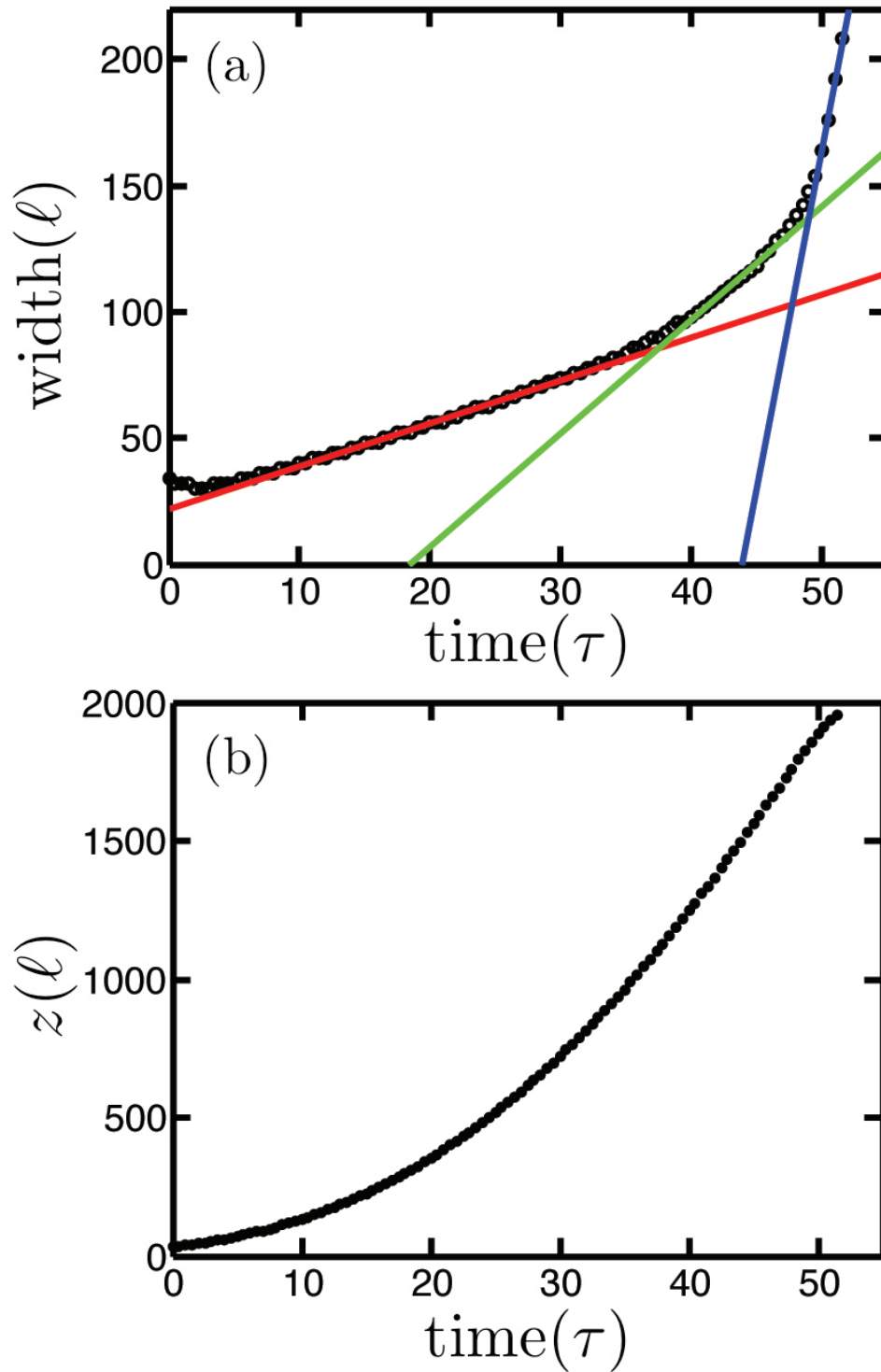
Figure 5.8: The growth of initial plume head as a function of time, showing (a) the width of the head, and (b) its height. Coloured lines in (a) show the nearly linear evolution of the width in the growth regimes. Note the similarity of this figure with the corresponding figure produced for experimental data in Fig. 3.4

and final growth regime is the fastest and it occurs when the plume head pinches-off from the conduit and becomes a thermal. Figure 5.8b shows that the simulated data for the ascent of the plume head during these stages of growth was also corresponds well with the experimental data, which was shown in Fig. 3.4b. The head accelerates as it ascends, even after it has pinched-off from the conduit. The pinched-off head continues to accelerate until it reaches a maximum velocity, after which time it decelerates because of boundary effects near the top of the tank. The maximum velocity of the head achieved in the simulation is $v_{max} = 67\ell/\tau = 0.065$ cm/s. This compares well with $v_{max} = 0.077$ cm/s extracted from the experimental data in Fig. 3.4b. Since the spatial domain for the simulation is less than the experimental tank dimensions, the head is more constrained by viscous interaction with the boundary and it has less vertical space to grow. A value of v_{max} for the simulation less than what achieved in the experimental plume is therefore not surprising.

A close up of the c, T, and p fields on the head of the plume with the reaction front superimposed is shown in Fig. 5.9. The temperature field around the plume head is much more dispersed than the concentration field comprising the head. This occurs because the thermal diffusivity is much greater than the molecular diffusion constant for the autocatalyst, by a factor of 2.8×10^2 (the Lewis number). Interestingly, the warmest region of fluid is only partially enclosed by the reaction front, while most of it resides in between the vortex rings. This location also happens to be where the only negative vorticity appears. The pressure field shown in Fig. 5.9 also has interesting features. As the plume head grows, the buoyant force acting on it increases and causes it to accelerate. As the velocity of the head increases, so does the pressure on the head that develops from viscous resistance to its motion. The pressure that builds up on top of the head deflects upwelling fluid outwards, where vortical flow causes it to wrap back inwards towards the conduit and form a mushroom-shaped plume head. In the wake of the plume head there is a pressure drop.The same distribution of pressure is also observed in experiments on rising spherical cap bubbles [109]. For a bubble, when the viscous force (causing pressure on top of the bubble) and the force of buoyancy (causing pressure on the bubble bottom) equilibrate, the bubble reaches its terminal velocity, which was given in Eq. 3.10.

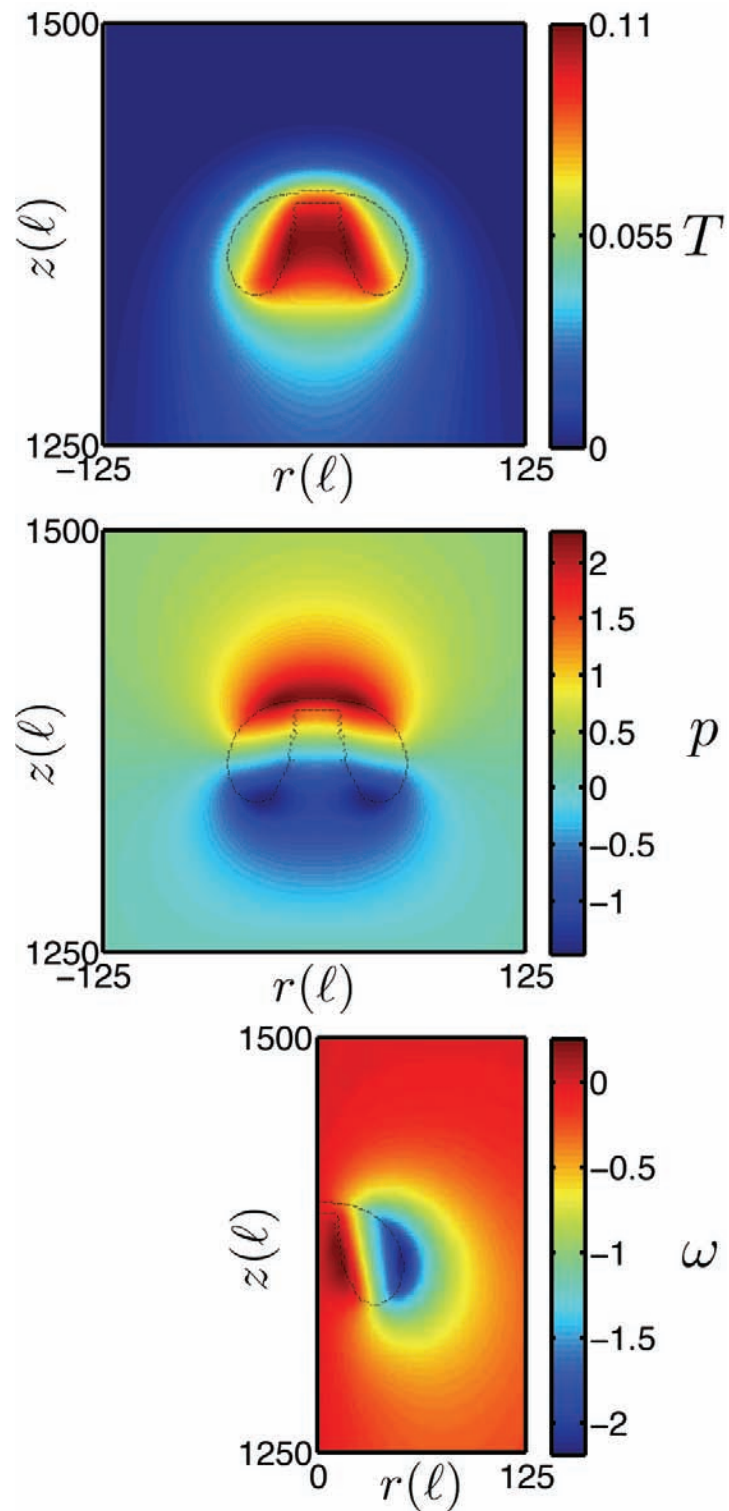Figure 5.9: A close up of the c, T, and p fields on the head of the plume from Fig.5.7 with the reaction front of the head superimposed as a black line.
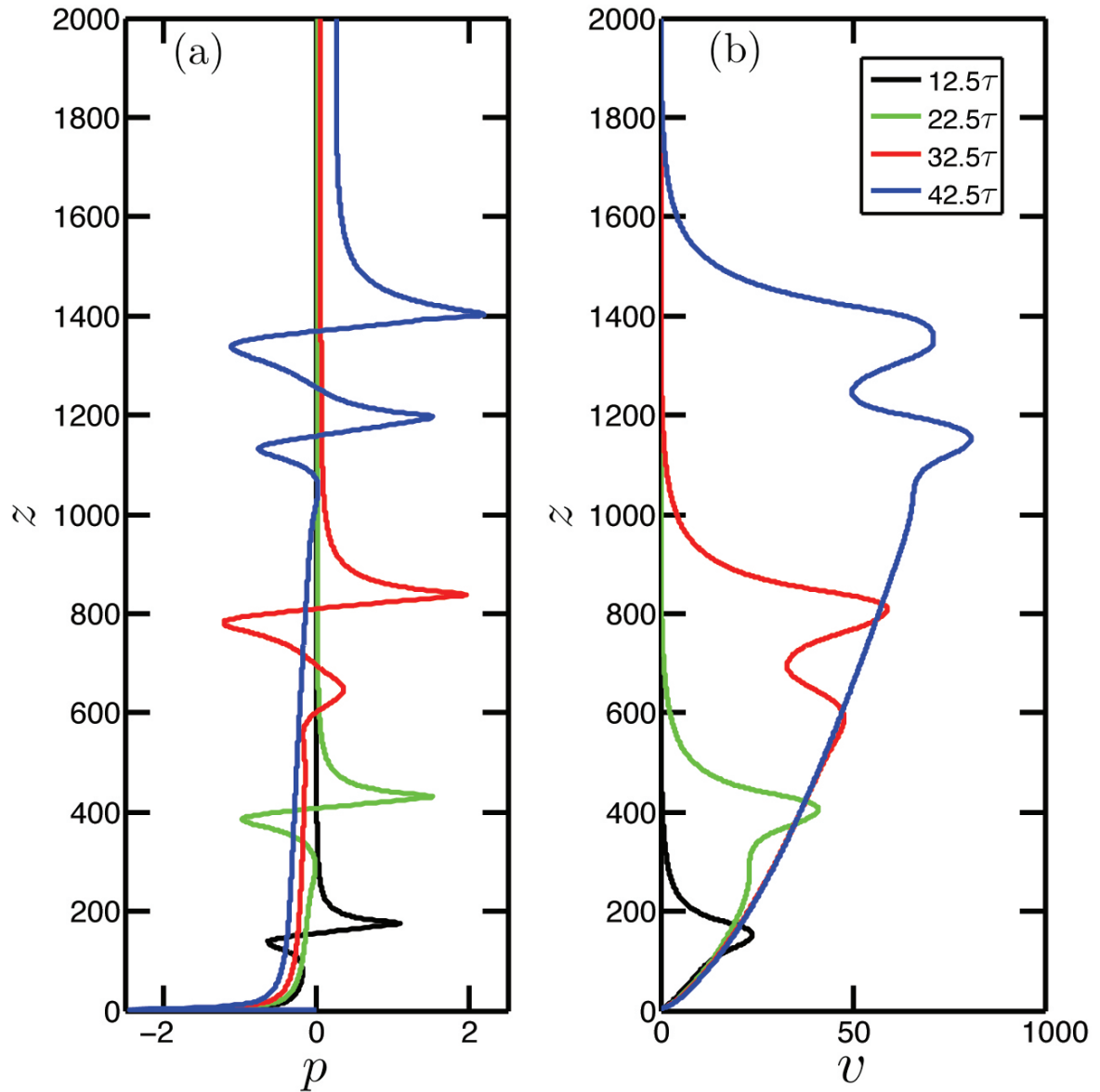
Figure 5.10: a) The pressure field and the b) the vertical velocity field along the plume axis for different times. As the plume evolves, a secondary maximum develop in both fields, indicating the development of a second generation plume head.

5.4.2   Pinch-off

The basic process of autocatalytic plume head pinch-off was described in Section 3.2.1. The description given can be summarized as follows. The head disconnects from the conduit once it has achieved a high enough velocity to separate from the flow that was once feeding it. As the head pulls away from the conduit, a bottleneck forms where the conduit narrows from the pinch, and a new, second generation plume head forms. In this Section we outline further insight into the pinch-off process that comes from our simulation results. Simulations show that pinch-off is not the sole consequence of plume head acceleration, which also involves acceleration within the conduit itself.

A compositional plume head is formed by buoyancy flux from its upwelling plume conduit. In order to feed the head, the conduit velocity must rise at a greater velocity than the head, as discussed in the context of forced plumes in Section 2.2.1. Therefore, the plume head cannot detach from the conduit. As the head rises it must push its way up through quiescent fluid, and this induces large scale flow in the tank. Once this flow has been established, fluid rising in the conduit has less resistance to motion than what was experienced by the head - it is moving upwards into fluid that already has momentum in the direction that it is going. This leads to the formation of a steady-state "pipe" flow below the plume head, where the geometry of the conduit and velocity profile across the conduit is constant, independent of height. The velocity profile of steady state compositional plume conduits was discussed in Section 4.2.1, and the cylindrical geometry in Section 4.2.2.

Autocatalytic plumes also develop a steady state conduit (see Section 4.2), however the transient phase is much more complex than in compositional plumes. The complexity is highlighted by the pinch-off process, which our simulations were able to reproduce. The pressure field for a plume that has pinched-off is shown in Fig. 5.7. In the pressure field, there are two regions where there are local maxima. One is at the top of the head, where resistance to flow is greatest, and the second maximum is located underneath the plume head, where the second generation head is forming. Clearly, the steady corridor for conduit flow set beneath a compositional plume head is not present for autocatalytic plumes. This is due to the unsteady nature of the developing plume conduit.

Prior to pinch-off, there is only one maximum in the autocatalytic plume pressure field, which appears at the top of the head. This is shown in Fig. 5.10a, which displays the pressure along the axis of the plume at various times. In early stages of plume evolution,

the pressure distribution for the entire plume is characterized by a pressure maximum at the top of the head, followed by a pressure drop in the wake. As the plume evolves, a localized region of increased pressure emerges in the conduit, forming a second maximum followed by pressure drop in the wake. By the time the plume reaches the point that is shown in Fig. 5.7, the second pressure maximum is almost the same magnitude as the first. The development of the second maximum coincides with the development of the second generation plume head, which is a consequence of reaction in the conduit.

As the plume evolves and the conduit elongates, reaction along the conduit wall causes it to increases in volume, and therefore increase the flux and velocity of fluid ascending in the conduit. This is shown in Fig. 5.10b, which displays the vertical velocity profiles along the plume axis at different times. The velocity profiles also show that in the early stages of plume growth, the conduit velocity increases with distance from the bottom boundary. In contrast to the velocity of compositional plume conduits, the velocity at every location along the conduit is also less than the velocity of the head, which is where the maximum ascent velocity is achieved. Despite this contrast with compositional plume behaviour, before the autocatalytic plume head pinches-off it maintains an appearance approximately like that of a compositional plume. The autocatalytic plume maintains this appearance because viscous deformation of the head pulls a "tail" underneath the head. Tail formation is discussed at length below, in Section 5.5.2. The tail, coupled with the continued elongation of the conduit upwards into the tail, gives the autocatalytic plume prior to pinch-off the general morphology of a compositional plume. Based on its morphology, it therefore seems as if the autocatalytic plume head is being fed by a higher velocity conduit. However, simulations show this assumption to be incorrect.

It should be noted that while the initial condition for the simulation explored in detail in this Section was a sphere of catalyst just touching the bottom boundary, very similar results to those presented occur for simulations using a sphere-cylinder arrangement. In these simulations, in the very early stages of plume development, the highest vertical velocity is found in the conduit. Only a short time into the evolution of the plume, however, the maximum velocity can be found in the head, and a velocity profile along the axis very similar to the one in Fig. 5.10b is found. As an example, consider a simulation with $r_{s0} = 40\ell$, $r_{c0} = 34\ell$, and $c_0 = T_0 = 0.99$, where the sphere was initially placed at $z = 180\ell$ in a domain $r_b = 1060$ and $z_b = 4800$. In this simulation, it only took $\sim 4\tau$ after initiation for the velocity in the head to exceed the velocity in the conduit. The biggest difference between simulations using the sphere-cylinder initial condition instead of the

sphere initial condition was the height at which pinch-off occurs. Pinch-off occurs closer to the bottom boundary for sphere initial conditions, just like pinch-off was observed to occur much earlier for experimental autocatalytic plumes that ascend according to the simple reacting sphere model discussed in Section 3.3. In Section 5.5, only reacting spheres are considered. Unlike the initial conditions used to produce plumes, where spheres are initiated on top of the bottom boundary, we will explore the evolution of these spheres when they are initially placed far above the bottom boundary.

5.4.3 Steady conduit

Given the computational expense of a plume simulation, it was usually the case that only transient starting plumes were simulated. When the last plume head reached the top of the spatial domain, simulations were usually aborted. However, in some cases simulations were left running long enough for a steady plume conduit to form. Results from one of these simulations are shown in Fig. 5.11. The simulation parameters used the sphere-cylinder initial conditions with $r_{s0} = 40\ell$, $r_{c0} = 34\ell$, and $c_0 = T_0 = 0.99$. The initial location of the sphere is $z = 180\ell$ in a spatial domain with $r_b = 1060$ and $z_b = 4800$ and $\sigma = 1$. Figure 5.11a shows the vertical velocity component v across a horizontal cross section of the plume located at $h = 3571\ell \sim 15$ cm at time 200τ. The concentration field of the plume shows the steady conduit in Fig. 5.11b.

Compared to the dynamic MRI vertical velocity measurements previously discussed in Section 4.2.1 and shown in Fig. 4.3, the simulation data does not resemble the velocity profile given at $h = 15$ cm, or even the profile at $h = 10$ cm. However, as shown in Fig. 5.11a, the simulation velocity data in the vicinity of the conduit does fit well with the symmetric bimodal Gaussian distribution given in Eq. 4.2. The simulation conduit width at the location where the velocity profile is given is only $\sim 50\ell = 2$ mm. In comparison, the conduit width for the experimental data is ~ 7 mm at $h = 15$ cm and ~ 5 mm at $h = 10$ cm. Since the simulation conduit is so much thinner than the experimental conduit, the buoyancy contribution at the plume edge is not far enough apart to show an off-centre velocity maximum in the symmetric bimodal distribution.

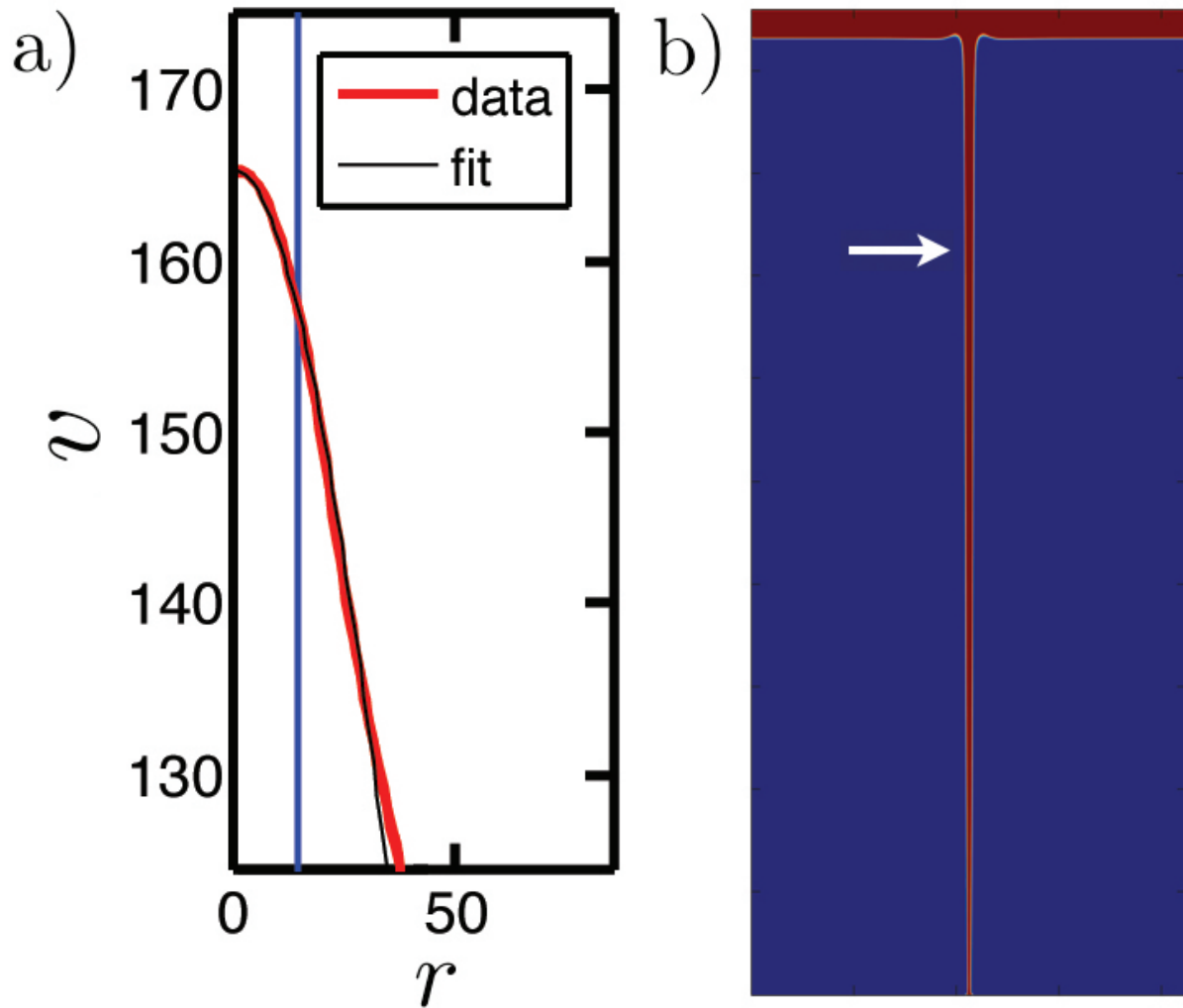Figure 5.11: a) The vertical velocity profile across the autocatalytic plume conduit shown in b) at $h = 3571\ell \sim 15cm$. a) Data from the simulation (red line) is the vicinity of the conduit is fit to a bimodal Gaussian distribution (black line). b) The concentration profile for the entire spatial domain of the simulation. A white arrow indicates the location along the conduit where $h = 3571\ell$.

5.5 Buoyant autocatalytic flame balls

Autocatalytic reaction fronts under gravity are in some ways analogous to flame fronts [74, 75] where the feedback through temperature change in combustion systems is analogous to the feedback of autocatalyst in chemical reaction systems. Autocatalytic reaction fronts, like the IAA reaction, also have considerably weaker buoyancy effects. Therefore, the deformation of a highly buoyant flame ball in a small gravitational field is analogous to the deformation of a weakly buoyant *autocatalytic flame ball* in terrestrial gravity. Previous studies on isothermal autocatalytic flame balls have focused on and the effect of autocatalyst decay [72], and on the existence and the stability of spherically symmetric solutions in the absence of buoyant forces [70, 71].

In this Section, we simulate the deformation of autocatalytic flame balls caused by buoyancy-driven convection. Using different sizes of autocatalytic flame balls in our simulations, we found three regimes with differing behaviour. In the first regime, below a minimum threshold size, flame balls undergo front death, where a reaction front is not sustained. In the second size regime above the front death threshold, buoyant autocatalytic flame balls grow reacting "tails" which are analogous to flame strings. In the third regime, above another size threshold, reacting tails no longer develop. For convenience, in this Section autocatalytic flame balls will be referred to as flame balls.

5.5.1 Front death

As previously noted in Section 3.1.3, small localized regions of product solution are not capable of sustaining reaction fronts. When an outlet tube with a diameter of 0.9 mm is used to attempt a plume initiation, a small spherical ball of product solution formed at the outlet. When this happened, the small spheres did not initiate propagating fronts, instead the spheres slowly faded out of view, signifying that the front had dissipated. In this Section, this phenomenon is investigated by simulation.

To explore front death, the same fluid conditions used for simulations in previous Sections was used. Spheres of product solution with $c_0 = 1$ and various radii r_0 were used as initial conditions. Convective effects are suppressed in these simulations so we can study front death as a pure reaction-diffusion phenomenon. Even when buoyancy is introduced into the calculation, the buoyant force on small spheres of product solution is nearly negligible, and there is therefore very little transport during the time scale it takes for the front to die. All simulations were performed on a spatial domain of $z_b = r_b = 120\ell$
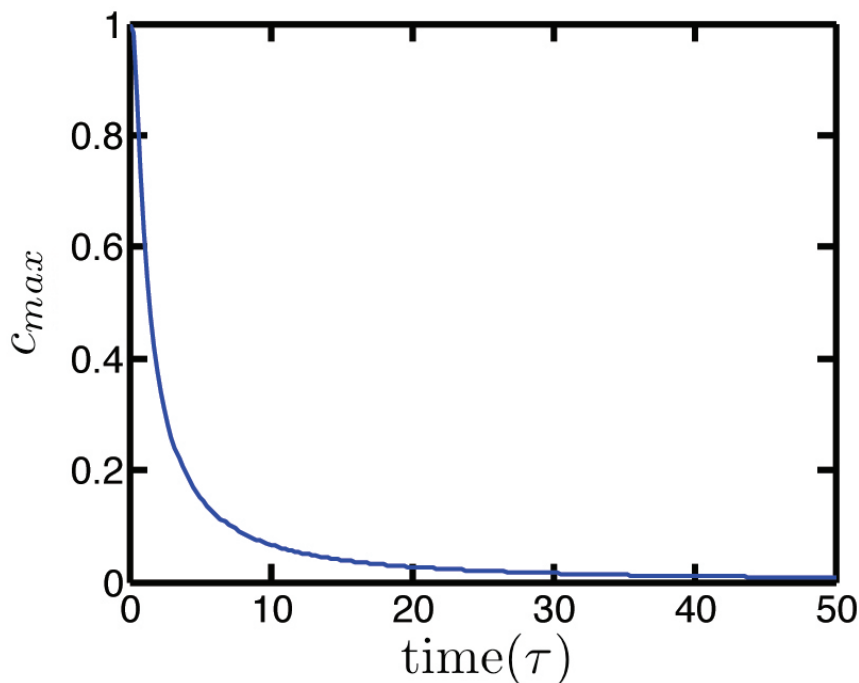
Figure 5.12: The change in the maximum value of the concentration field over time. The curve continuously approaches $c_{max} = 0$ as the product in the initial flame ball diffuses and fails to reignite a reaction front.

at a high mesh resolution of $\sigma = 5$.

The maximum value of the concentration, c_{max}, as a function of time for a flame ball with $r_0 = 2\ell$ is shown in Fig. 5.12. The decrease in c_{max} over time shows that no new catalyst is being produced by a reaction front, and therefore the front set up in the initial condition has died. The distribution of catalyst at different times is shown in Fig. 5.13. The structure of the front shows that over time, the catalyst simply diffuses away from its initial position without forming a reaction front. A simulation with $r_0 = 2.5\ell$ also exhibited front death. However, a simulation with $r_0 = 3\ell$ shows an entirely different outcome. The initial front appears to be dying as it did in the $r_0 < 3\ell$ cases. After a period of time, however, sufficient new catalyst is generated, signifying that the front has recovered from the initial concentration loss. Front recovery is shown in a plot of the maximum concentration over time in Fig. 5.14, and in the distribution of catalyst in space for various times in Fig. 5.15. At times less than $\sim 10\tau$ the concentration diffuses and new product is not generated. Past this point in time, however, the front recovers, leading to the stable propagating front structure shown in Fig. 5.15 at 40τ and 50τ.

Front death in the IAA reaction is caused by diffusion effects, and is not a consequence
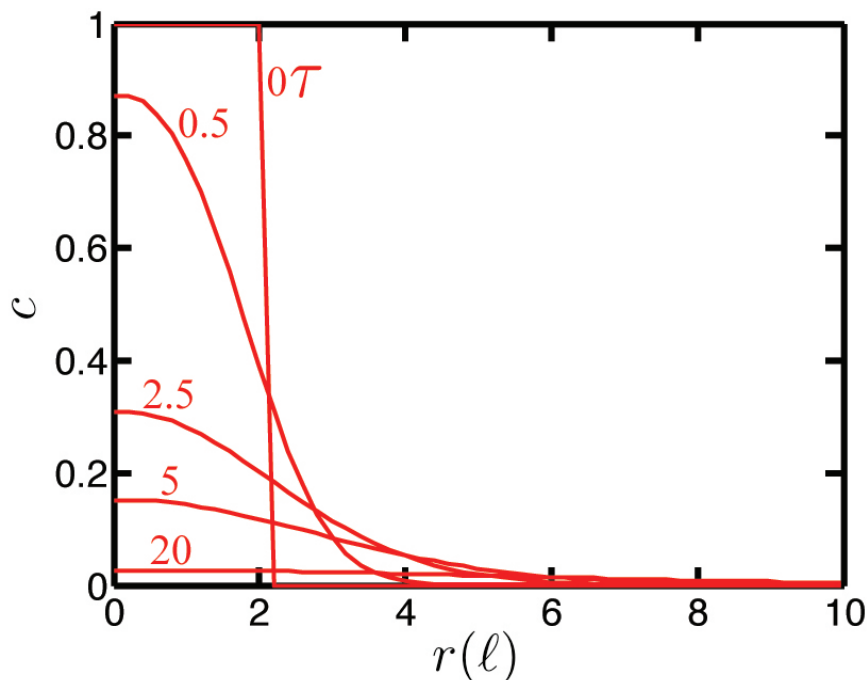
Figure 5.13: Concentration profiles at different times (in multiples of τ) for a flame ball with $r_0 = 2$. The reaction front imposed as the initial condition dies, and over time the concentration profiles spread outwards and flatten.

of more commonly observed threshold behaviour in excitable systems, like the action potential of neurons [110] or the propagating oxidation wave in the Belousov-Zhabotinsky (BZ) reaction [111]. Neurons and the BZ reaction are excitable in the sense that they remain in a stable state until a threshold is reached. At the threshold, the system becomes "excited" and is pushed into an unstable state. For a neuron, this excited state occurs when an electric signal is transmitted once a certain voltage, or action potential, is reached. In the BZ reaction, excitation is reached when enough catalyst is present to transmit a propagating oxidation wave through the system. A pulse, unlike a reaction front, does not consume all of the reactants as it proceeds through a solution, allowing the system to be excited more than once. The IAA reaction, on the other hand, always has locally unstable kinetics [73]. The presence of any amount of autocatalyst in the IAA system will therefore always render it unstable. However, despite the localized instability created by the presence of autocatalyst, in a three dimensional system, diffusion effects alone are enough to quench the instability and hinder production of a reaction front.

In general, for an autocatalytic system, front death depends on the dimensionality of the system, and the mechanism of autocatalysis. For a quadratic autocatalytic reaction
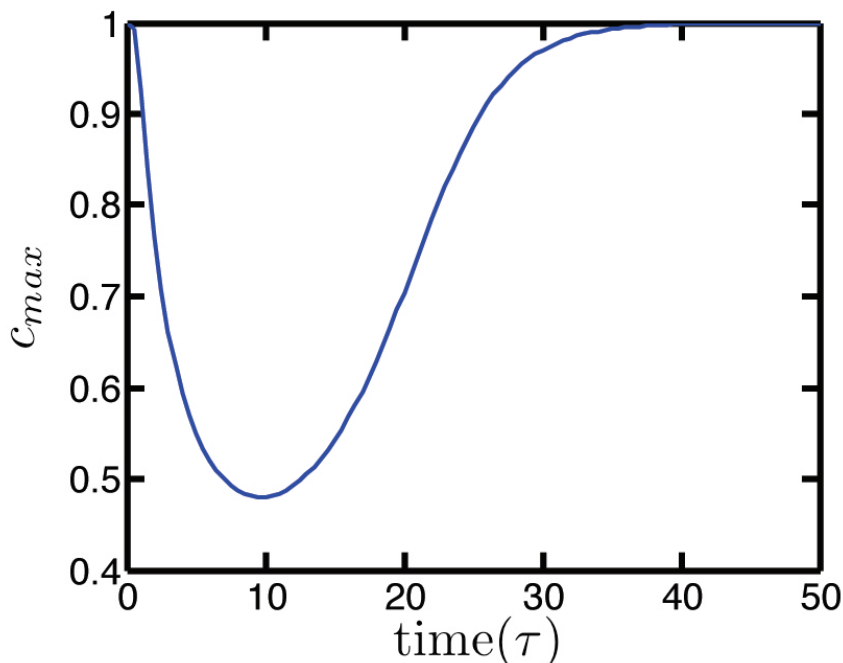
Figure 5.14: The change in the maximum value of the concentration field over time. The curve decrease indicates the front appears to be dying, but it then rebounds upwards as the front recovers and restores the maximum concentration to $c_{max} = 1$.

scheme, theory predicts that a traveling front will evolve from any amount of autocatalyst in any geometrical configuration [73]. For a cubic autocatalytic reaction-diffusion system, like the IAA reaction, a mathematical treatment of the relevant reaction-diffusion equations has shown that the presence of any amount of autocatalyst will always form a reaction front in a one dimensional slab geometry [112, 113]. Two dimensional calculations show equivalent behaviour [73]. In three dimensions, however, the theory predicted that below a certain spatial distribution of autocatalyst, diffusion alone inhibits front propagation. We confirmed this prediction by observing front death in the IAA system experimentally. In this Section, we also used physical fluid parameters to determine the size threshold below which a flame ball concentrated with autocatalyst will not produce a reaction front. [5]

---

[5]We have referred to this phenomenon as front death because we consider the front imposed by the initial conditions to be a "live" front. Furthermore, in our experimental system the front propagated through a capillary tube before dying after it had emerged into the larger vessel. In Ref. [73] a slightly different interpretation of front death is given, where the front is considered not to be present until it propagates in its stable form. In this interpretation, if a front does not emerge from the initial conditions, then the front has not died because it never existed.
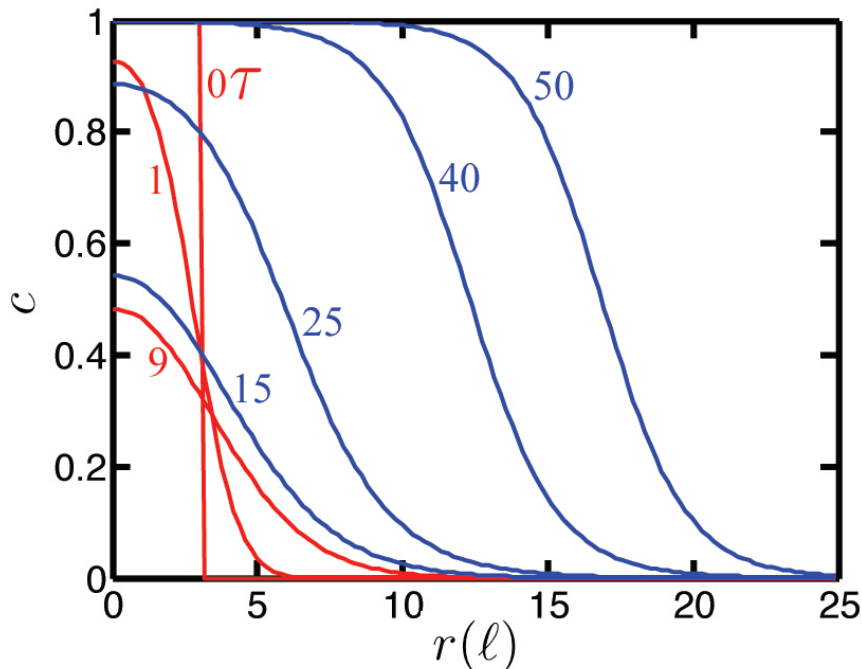
Figure 5.15: Concentration profiles at different times (in multiples of τ) for a flame ball with $r_0 = 3$. Red curves indicate concentration profiles where the front appears to be dying, blue curves are for profiles after the front has recovered.

5.5.2 Flame ball heads and tails

In Section 5.5.1, the approximate threshold radius that the initial flame ball must have for it to sustain a propagating front was established. For flame balls below, $r_0 <\sim 3\ell$ front death occurs. To simplify our front death calculations, buoyancy was suppressed in the simulations. In this Section, buoyancy effects are once again considered, and the evolution of a flame ball is due to the dynamic interplay between reaction, diffusion, and buoyancy driven flow. The only difference between the flame ball simulations in this Section and the plume simulations discussed in Section 5.4 is the location of the initial condition. While plume simulations used initial catalyst distributions on or slightly above the bottom boundary, flame balls have spherical initial conditions that are initially placed many flame ball radii above the bottom boundary. The concentration on the bottom boundary is therefore always $c = 0$. Similar to the threshold in r_0 that is necessary to sustain a reaction front, by simulating the evolution of different radii flame balls, we have found a threshold in r_0 below which a flame ball will stretch and form a reacting "tail". The flame ball is stretched in the direction of the gravitational force, and in addition

Figure 5.16: The ascent of flame balls with different initial radii over time. The curves correspond to flames balls with r_0 values of a) 27.5, b) 22.5, c) 17.5, d) 15, e) 10, f) 7.5, and g) 5ℓ.

to a tail it also develops a head like an autocatalytic plume. For r_0 values above this threshold value, tails are too thin to form a reaction front, and the majority of reaction product remains in a localized "thermal".

The ascent of flame balls over time with different initial radii is shown in Fig. 5.16. For all flame balls discussed in this Section, the centre of the flame balls were initially located at the same height $z_0 = 100\ell$ in a spatial domain with $r_b = 500\ell$ and $z_b = 2000\ell$. The resolution was $\sigma = 1$, and the time step was $\Delta t = 0.005$. Like all of the simulations in this Chapter, the fluid parameters for this simulation correspond to those in a reactant solution with a 40% glycerol concentration. Not surprisingly, the flame ball with the largest r_0 reaches the top of the spatial domain faster than any other flame ball. The other flame balls reach the top in descending order according of r_0. Despite the difference

in the amount of time it takes flame balls with different r_0 to reach the top of the tank, all of the flame balls reach a terminal velocity that is nearly identical, increasing only marginally with r_0. The range of terminal velocities was 64.9 to 68.9 in units ℓ/τ, which corresponds to a difference of only 5×10^{-3}cm/s between the velocities achieved by the smallest and largest r_0 flame balls. Velocities were determined by calculating the slope of each line in Fig. 5.16, and the terminal velocity was determined by taking the maximum value of the slope for any five consecutive data points. For all of the data, five consecutive data point corresponds to time window of 2τ, or 8.6 seconds.

The evolution of the morphology of a small flame ball, only twice the size of a flame ball where the reaction front dies, is shown in Fig. 5.17. The entire spatial domain of the simulation is not shown in the figure images. In the initial stages of the evolution of the flame ball, it remains roughly spherical. However, as it continues to convect upwards, it develops a thin, elongating trail of autocatalyst in its wake, which we refer to as the tail. As the tail elongates, the upper portion of the flame ball develops into a vortex ring that resembles a plume head. Just as an autocatalytic plume head pinches-off from its conduit, a flame ball head pinches-off from its tail. As it does so, the top of the tail grows a new, second-generation head, and the first-generation head rises upwards as a thermal that takes the form of a free vortex ring.

The structure of a laminar starting plume was established in the introductory Chapter of this thesis in Fig. 1.1, where the main components of a laminar plume were identified to be the head and the conduit. For the compositionally buoyant forced plumes discussed in Chapter 2, it is clear that upwelling flow from the conduit provides volume flux to the growing, rising head. Given their similar appearance to compositionally (and thermally) buoyant laminar plumes, we chose to label autocatalytic plumes with the same terminology. The autocatalytic flame ball simulations, however, call into question use of this terminology. As outlined above, there are many similarities between autocatalytic flame ball tails and autocatalytic plume conduits. The only appreciable difference between the two is that a conduit remains fixed to the bottom boundary, while a tail does not. Based on the simulation results in this Section, it seems that in the experiments discussed in Section 3.2, autocatalytic plume heads are very likely to be *producing* a large portion of the trailing conduit in the same way that a tail is produced by an autocatalytic flame ball. This is in stark contrast to the relationship between the conduit and head in compositionally buoyant plumes. While we will continue to refer to the fluid structure connecting the bottom boundary to the head as a "conduit", and the structure

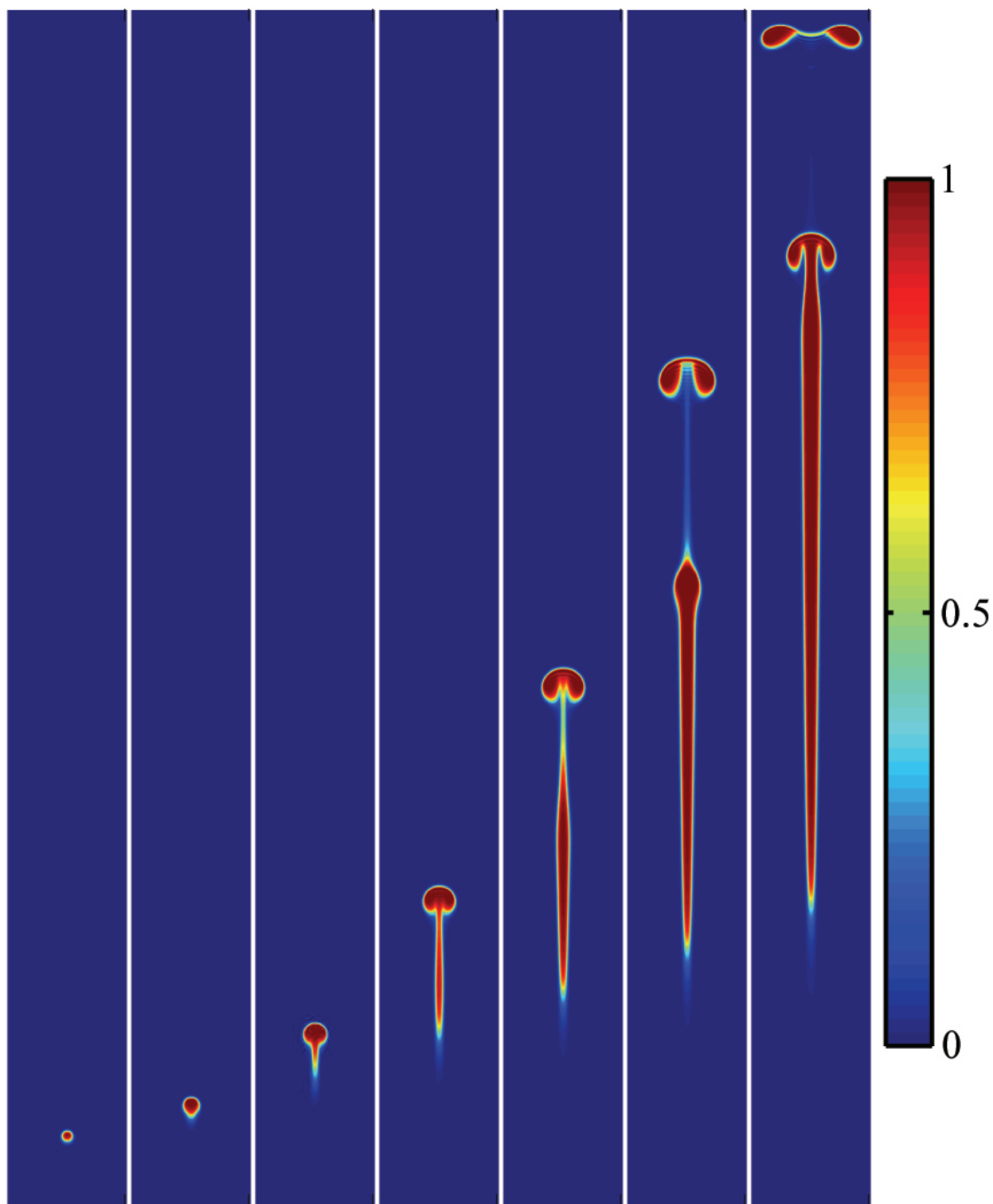Figure 5.17: The evolution of a flame ball with $r_0 = 5$, showing the development of a the head and reacting tail. The spatial domain of the simulation is $r_b = 500$ and $z_b = 2000$, however the portion of the field displayed field shown has a radius of 100ℓ. From the left-most frame to the right-most frame, the elapsed time after t_0 is 10τ to 70τ in increments of 10τ.

beneath a flame ball as a "tail", their near equivalence should be recognized. Similarly, the corresponding near equivalence of an autocatalytic plume and an autocatalytic flame ball should be noted.

An interesting morphological transition occurs for simulations of flames balls with $r_0 \geq 27.5$. In these simulations, a reacting tail does not develop. This is shown in Fig. 5.18 which shows the concentration field at different times for a flame ball with $r_0 = 27.5\ell$. As the flame ball rises, it leaves behind a tail. However, unlike the tails formed in the wake of flame balls with $r_0 \leq 25$, the tail it leaves behind is so thin and dilute that it does not react. Since the tail is very thin and is composed of only a dilute quantity of product, it is not capable of producing a propagating front, much like a tiny flame ball that undergoes front death. While the exact cutoff radius for reacting tail development, r_{0t}, was not determined, simulation results show that it lies in the range $25 < r_{0t} \leq 27.5$.

Despite the obvious difference between the amount of product produced by a flame ball with and without a reacting tail, the amount of product that initially arrives at the top of the domain in the head is similar for all values of r_0. The integral of the concentration field for each head was calculated, and the difference between the amount of product reaching the top for the $r_0 = 5\ell$ simulation and the $r_0 = 27.5\ell$ was determined to be only $\sim 8\%$, with the larger flame ball delivering the slightly larger amount of product. Even though larger r_0 flame balls start with a larger amount of product, small flame balls take longer to reach the top allowing them more time to react. This allows for the initial volume of product arriving at the top to be approximately the same regardless of initial flame ball radius.

To understand why tail production ceases once r_0 surpasses r_{0t}, it is useful to use a dimensional analysis scheme for flame balls similar to the one developed for astrophysical flame bubbles [114]. For highly viscous flame balls, two time scales are useful for estimating the conditions when a spherical ball of product undergoes distortion induced by buoyancy driven flow. These time scales are the viscosity time scale

$$\tau_v = \frac{r_0^2}{\nu}, \tag{5.13}$$

and the buoyancy time scale

$$\tau_b = \sqrt{\frac{r_0}{g'}}, \tag{5.14}$$
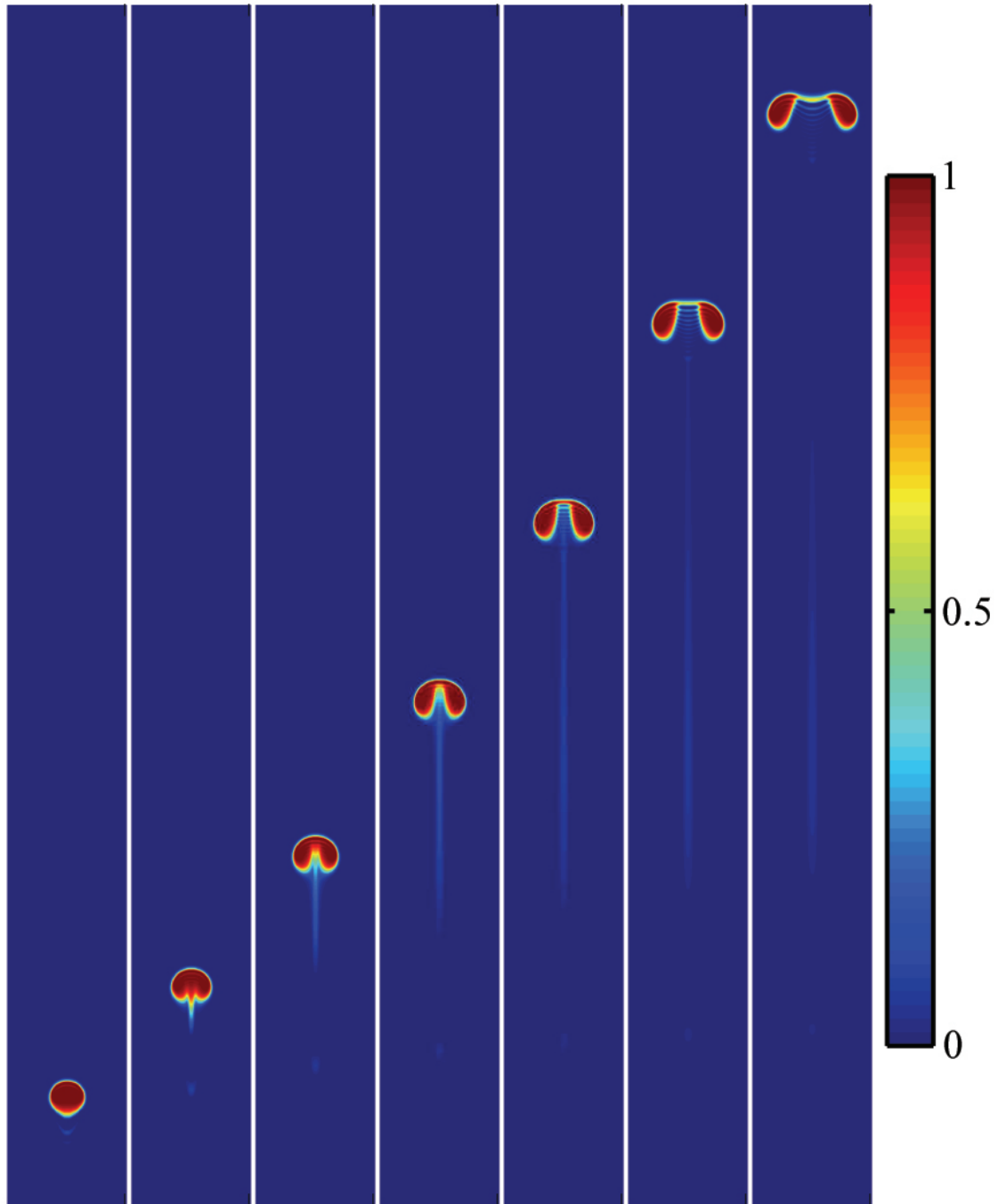
Figure 5.18: The evolution of a flame ball with $r_0 = 27.5$, showing that a very thin tail of autocatalyst trails the head, and that the tail is not capable of producing a reaction front. The spatial domain of the simulation is $r_b = 500$ and $z_b = 2000$, however the portion of the field displayed field shown has a radius of 100ℓ. From the left-most frame to the right-most frame, the elapsed time after t_0 is 2.5τ to 32.5τ in increments of 5τ.
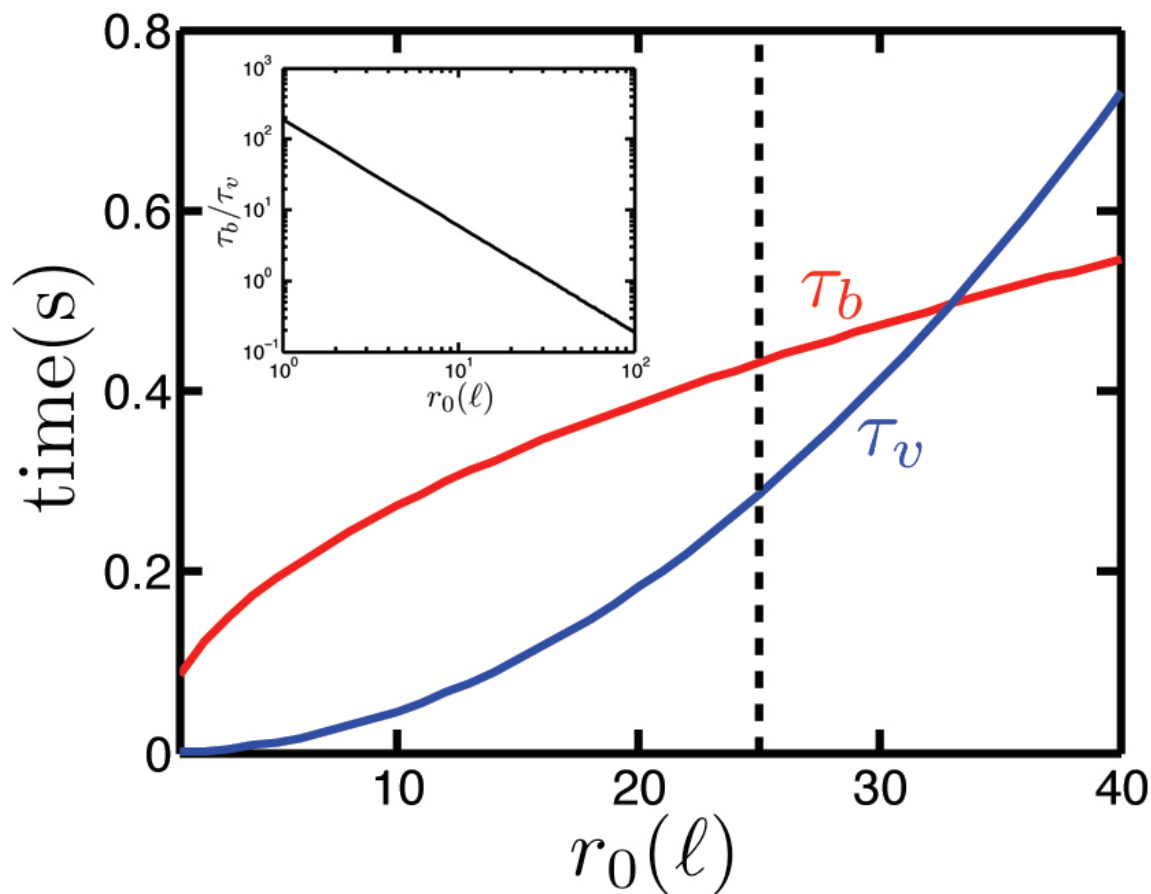
Figure 5.19: The viscosity time scale, τ_v, and the buoyancy time scale, τ_b, as a function of flame ball radius r_0. The time scales meet at r_c. The cutoff value for r_0 above which simulations showed that tails cannot form a reaction front is shown by the vertical dashed line. The inset shows the power law relationship between the ratio of the two time scales as a function of r_0, which is $\tau_b/\tau_v \sim r_0^{-3/2}$.

where $g' = g(\rho_u - \rho_r)/\rho_u$ is the buoyancy of the flame ball, with g being the gravitational acceleration, and ρ_r and ρ_u being the densities of the reacted and unreacted fluid, respectively.

A balance between the viscous and buoyancy forces is reached when $\tau_v = \tau_b$. This occurs at the critical flame ball radius

$$r_c = \left(\frac{\nu^2}{g'}\right)^{1/3}. \tag{5.15}$$

Using fluid parameters from Table 3.1, and a total density jump across the front from compositional and thermal changes of $\Delta\rho = (\rho_u - \rho_r) = 6.4 \times 10^{-4}$ g/cm^3, this gives $r_c \sim 33\ell$ [6]. A plot of τ_b and τ_v is shown in Fig. 5.19. For $r_0 \ll r_c$, $\tau_v \ll \tau_b$, and therefore viscous forces have more time to act on, and therefore deform, the flame ball as it ascends. As r_0 increases, the ratio of τ_b/τ_v decreases as a power law

$$\frac{\tau_b}{\tau_v} = \frac{\nu}{\sqrt{g'}}r_0^{-3/2}, \tag{5.16}$$

and viscous forces have a decreasing impact on flame ball morphology. In our simulations, viscous deformation of the flame balls for $r_0 \leq 25\ell$ was capable of dragging enough product out of the flame ball to form a tail capable of producing a reaction front. For $r_0 \geq 27.5\ell$, however, the dilute, filamentous tail pulled into the wake of the flame ball does not leave enough catalyst to sustain a reaction front.

5.6   Summary

In summary, we have simulated autocatalytic plumes using an axisymmetric computation in a cylindrical coordinate system. The simulation produces concentration, temperature, pressure, and velocity fields in the σ and z directions. Reaction fronts in thin tubes were simulated, and the results produced an axisymmetric mode of convection once the tube radius was extended across a threshold value of r_b. Below this value, front velocity is not enhanced by convection and the front is flat. The behaviour of fronts in thin tubes produced by our simulations was generally consistent with experimental observations

---

[6]The total density difference between a reacted fluid with $c = T = 1$ and $c = T = 0$ is $\Delta\rho = \Delta\rho_c + \Delta\rho_T$, where $\Delta\rho_c = 4 \times 10^{-4}$ g/cm^3 is the isothermal density difference from compositional change, and $\Delta\rho_T = 2.4 \times 10^{-4}$ g/cm^3 is the density difference caused by heating the reactant solution by 0.5 K.

of reaction fronts in thin tubes, and the front velocity without the aid of convection was on the order of what we measured experimentally. The discrepancy between the front velocities is likely due to differences in the experimental and simulation boundary conditions.

In spatial domains much larger than those used for thin tubes, plumes were simulated. It was determined that numerical instabilities lead to oscillations in the concentration field across the reaction front. These oscillations could be minimized by increasing the mesh resolution. However, it was also determined that the concentration oscillations have a small effect on the other fields calculated by the simulation.

Simulated autocatalytic plumes reproduced the general behaviour of those produced experimentally. Using simulation results, it was possible to refine our understanding of autocatalytic plume dynamics by having access to fields not available through our experiment. We were thus able to construct a better understanding of the dynamics that leads to pinch-off in autocatalytic plumes, which is summarized as follows. An autocatalytic plume head increases in size as it ascends, and vortical flow enhances this growth by entraining fresh reactant solution. Head velocity is greater the conduit velocity, in contrast to the head velocity of compositional plumes. However the velocity of the conduit, coupled with tail formation from the viscous deformation of the head, creates the appearance of a connected conduit that feeds the head buoyant fluid. While a plume head experiences growth in volume and buoyancy from reaction, so too does its conduit. As a result, flow velocity in the conduit increases, and a second generation head forms underneath a pressure maximum that develops within the conduit. Fluid rising in the conduit accumulates in the new head, and this cuts off flow to the portion of conduit between the first head and the newly forming head. This portion of the conduit therefore narrows, giving the appearance that the first generation plume head has pinched-off from the conduit. However, the first generation head was already rising independent of flux from the conduit long before the appearance of pinch-off occured.

In addition to plumes, we also simulated autocatalytic flame balls. The only difference between the plume simulations and the flame ball simulations was the location of the initial distribution of autocatalyst. The evolution of flame balls with different initial radii were studied, and three different regimes of behaviour were found. Very small flame balls that undergo front death occupy the first regime, where $r_0 < \ \sim 3$. In the second regime, $3 \leq r_0 \leq 25$, autocatalytic flame balls have reacting heads and tails. In the third regime, $r_0 \geq 27.5$, only a small amount of product is dragged into the wake of the head,

and the resulting filamentous tail does not produce a reacting tail. Tail formation was explained using two time scales, the viscosity time scale and the buoyancy time scale, which vary based on flame ball radius. The smaller the value of the time scale, the faster the respective effect acts on the flame ball. For the entire regime of flame balls presented in this Section, the buoyant time scale is greater than the viscous time scale. However, flame balls in the regime that do not produce a reacting tail is close to the radius where the two time scales are equal. Viscosity therefore has much less time to drag a tail into the wake of the flame ball, and the amount that is dragged in is not enough to form a reaction front.

Chapter 6

Conclusion

In this thesis, we have described a study of buoyant laminar plumes induced by two distinct types of forcing: inertial forcing for *forced* plumes and chemical reaction-driven forcing for *autocatalytic* plumes. Plumes were studied in detail for both starting and steady phases. In this Chapter, we come to some conclusions and discuss possible future research directions extending on the thesis work.

In Chapter 2, we discussed an experimental investigation of the scaling and morphology of forced starting plumes. Plumes were produced by injected slightly buoyant fluid into an initially quiescent fluid-filled tank. The plume heads formed in these experiments exhibited two distinct forms that we define as confined and dispersed. Confined plume heads contain a stable vortex ring and retain a self-similar shape as they grow. Plume heads become unconfined when the flow feeding the vortex ring fails to wrap underneath the head crest, and a trailing fluid skirt is formed. We determined that the type of head that forms depends on the dimensionless plume Richardson number, Ri, where the transition between the two types occurs at Ri~ 1. Confined heads are formed above this value, while dispersed heads form below.

Using dimensional analysis, we found that the system is described by a power law relationship between Ri and the Reynolds number of the injected buoyant fluid in the outlet pipe. This relationship is independent of the diameter of the outlet pipe d, which reflects the physical fact that plume morphology and ascent velocity eventually become independent of the details of the localized source of buoyancy and momentum that produced it. This result generalizes some previous observations and theory for thermal plumes to the case of forced compositionally buoyant plumes.

Our results are specific to the case of nearly isoviscous plumes with small density

contrasts. Mantle plumes, for example, have significant density and viscosity differences between the plume and its surroundings, and it would therefore be interesting to extend our study to incorporate these differences. It would also be interesting to explore plumes with both thermal and compositional buoyancy effects, particularly in the case where these buoyancy effects oppose each other in a double diffusive scenario. In many cases in Nature, plumes are subject to crossflow and occur in density stratified fluids (like the ocean, for example). An examination of forced buoyant plumes in these experimental conditions would also be an interesting extension of our study.

In Chapter 3, we described an experimental study of buoyant autocatalytic plumes, where no external forcing was imposed on the system and buoyancy was entirely due to chemical reaction. The reaction used to drive plume motion was the autocatalytic iodate-arsenous acid reaction. In sufficiently viscous water-glycerol solvents, we found that plumes form with well-defined heads that eventually pinch-off from their conduit. The detached heads form essentially free reacting vortex rings. The entrainment of reactant solution into an autocatalytic plume head or vortex ring provides additional buoyancy to these structures, leading to their acceleration. This acceleration is the result of a self-stirring mechanism that is provided by the interplay between chemical reaction and the flow that it induces.

During an experimental run with pinch-off, detachment of the plume head resulted in the generation of at least one additional plume head. Often, this interesting dynamical process was repeated several times for a single experimental run, and many subsequent generation heads were produced. With the exception of the final plume head produced, all plume heads for a given run, and all plumes for a given set of fluid parameters, yielded approximately the same value of Re_h. However, the location of initial pinch-off of a plume head and the number of pinch-offs observed were variable. This variability is attributed to the fact that autocatalytic plumes are sensitively dependent to the dimensions they take in the very earliest stages after they emerge from the outlet. Small fluctuations in flow near the outlet from exchange flow or other factors lead to large variations in the later stages of autocatalytic plume evolution.

The effect of the variability of these earliest, or "initial" conditions, on the ensuing evolution of an autocatalytic plume was tested using two simple chemical plume models, a reacting cylinder and a reacting sphere. It was found that the behaviour of an auto-catalytic plume could conform to the flow predicted by one of either of the models. The factor determining the model that could be used for a specific plume run was the initial

dimensions of the plume head and conduit. Slight variations in these dimensions could cause the head to behave either as a reacting cylinder or a reacting sphere. For autocatalytic plumes that ascended like a reacting sphere, pinch-off occurred much earlier in plume evolution. Early pinch-off would consequentially lead to the production of more subsequent generation heads. To explore wall effects in the autocatalytic plume system, it would be interesting to extend our experimental work by performing experiments in cylindrical tanks with different diameters.

Autocatalytic plumes may have a useful analogy to important geophysical and astrophysical processes. Hotspots due to upwelling from deep in the mantle have been the subject of laboratory analog experiments using conventional plumes [98]. Instabilities in the bottom layer of the mantle are also likely to give rise to thermals which may contain internal sources of buoyancy due to radiogenic heating [115]. Additionally, the IAA reaction with convection has been compared to a numerical model of a rising astrophysical flame bubble [80]. In future work, autocatalytic plumes and vortex rings could serve as an interesting laboratory analog of these processes.

The autocatalytic plumes studied in this thesis were all produced by the IAA reaction. There are a host of other reactions that produce propagating fronts with density gradients across the front. Plumes produced by the relatively highly exothermic chlorite-thiosulfate reaction front, for example, would likely evolve differently than IAA reaction plumes. Extending the work on autocatalytic plumes from this thesis by using different reactions would allow for an exploration into the effects of differing the relative contribution to buoyancy from thermal and compositional changes. Furthermore, a reaction with opposing thermal and compositional contributions to buoyancy could be used. Double-diffusion with opposing buoyancy effects is an important part of fluid flow in the ocean, where salinity gradients are responsible for compositional buoyancy differences. It would be interesting to compare the behaviour of double-diffusive salt plumes with plumes where double-diffusive effects are a consequence of chemical reaction.

In Chapter 4, we described a study of the steady state conduits produced by forced and autocatalytic plumes. The flow profile and morphology of these conduits were quantified and compared. The flow profile was examined using a dynamic MRI sequence called GERVAIS. This velocity imaging sequence was used to resolve vertical velocity components across a horizontal cross section of the flow. It was found that the vertical flow across an autocatalytic plume conduit may be phenomenologically described by an axisymmetric bimodal distribution, one that widens in accordance with the approximately

uniform conical widening of the plume. This is in contrast to the Gaussian velocity distribution that describes flow across a non-reacting plume conduit that remains cylindrical. These results emphasize that the buoyancy flux that drives the plume upward is created by the reaction front that forms the plume boundary. Autocatalytic plumes therefore have a source of buoyancy that is distributed along the entire interface between the plume and the surrounding fluid. This distinguishes autocatalytic plumes from forced plumes, or any other type of plume that has buoyancy supplied at a localized source. The possible extensions of our work on starting plumes discussed above are equally applicable for steady plumes. Persistent conduits subjected to crossflow in the mantle are believed to be the mechanism behind volcanic hot spot formation [9], and would be interesting to study in a reacting plume context.

A simulation of autocatalytic plumes was discussed in Chapter 5. The simulation involves an axisymmetric computation in a cylindrical coordinate system, and it produces concentration, temperature, pressure, and velocity fields for the plume. The simulation was tested by examining the flow produced in thin tubes. The behaviour of simulated fronts was generally consistent with experimental observations of reaction fronts in thin tubes, and the front velocity in the absence of convective effects was on the order of our experimental measurements.

In much larger diameter tubes, autocatalytic plumes were simulated. These simulations reproduced the general behaviour of what we observed experimentally: accelerating plume heads that pinch-off and spawn the growth of a secondary head. By simulating autocatalytic plumes, we were able to refine our understanding of the mechanisms at play that facilitate pinch-off. We found that the enhancement of buoyancy through reaction in both the head and the trailing conduit lead to vertical acceleration in the flow of both structures. As flow velocity in the conduit increases, a second generation head forms underneath a pressure maximum that develops in the wake of the first generation head. Fluid accumulates in the second generation head, and this disconnects the flow between the primary and newly forming secondary heads. This portion of the conduit between the two heads therefore narrows, giving the appearance that the first generation head has built enough buoyancy to accelerate away from the conduit. However, the first generation head was found to be rising independently of buoyancy flux from the conduit long before the thinning of the conduit in its wake.

By slightly changing the initial conditions for autocatalytic plume simulations, we investigated the consequences of initiating a "plume" well above the bottom boundary of

the spatial domain (recall that by definition a plume is connected to an isolated source, which isn't the case here). These runs were initiated using spheres of product solution which we refer to as autocatalytic flame balls because of their analogy to flame balls produced by combustion. Depending on the initial radius of the autocatalytic flame ball, it could have evolved similarly to an autocatalytic plume. In this scenario, the flame ball grows a head like a plume. However, instead of a conduit it grows a tail that remains does not attach to the bottom boundary. If the initial radius of the flame balls were beyond a critical length, the tail that drags behind the head is too filamentous to be able to sustain a reaction front, and the front dies. Front death also occurs for flame balls below a critical radius, where diffusion effects alone are sufficient to kill a reaction front.

The morphology of autocatalytic flame balls was explained using time scales for viscosity and buoyancy which vary based on flame ball radius. For all of the autocatalytic flame balls that we simulated, the buoyant time scale is greater than the viscous time scale. However, flame balls in the regime that do not produce reacting tails are on the vicinity where the two time scales are equal. Viscosity therefore has much less time to drag a tail into the wake of the flame ball, and the filamentous tail left behind is not sufficiently concentrated to sustain a reaction front.

There are no limitations on the fluid parameters that are used for the simulation. For this thesis, the parameters we used for our simulations were for IAA plumes in a 40% glycerol solution. Parameters for other reactions in less or more viscous solutions could be used. It would be particularly interesting to implement parametric investigation for double-diffusive autocatalytic reactions, where Ra_T and Ra_c have different signs and therefore opposing buoyancy effects.

In summary, through experimentation, simulation, and some simple theoretical analysis, we investigated the behaviour of laminar buoyant plumes. Two types of plumes with different forcing mechanisms were investigated: forced plumes were compositionally buoyant and were injected with momentum into a fluid filled tank, and in the absence of imposed mechanical forcing autocatalytic plumes were produced as the consequence of a buoyancy-producing chemical reaction. Rich fluid-dynamical behaviour was observed for both types of plumes and was discussed in this thesis. In forced plumes, the rich behaviour we observed was a consequence of the relative effects of buoyancy and forcing. For autocatalytic plumes, it was the interplay between chemical reaction and fluid flow that served as the foundation for compelling dynamics.

References

[1] P. Francis and C. Oppenheimer. *Volcanoes, 2nd ed.* Oxford University Press, 2004.

[2] S. R. Weart. *Nuclear Fear: A History of Images.* Harvard University Press, 1988.

[3] G. K. Batchelor. Heat convection and buoyancy effects in fluids. *Q. J. R. Met. Soc.*, 80:339, 1954.

[4] J. S. Turner. *Buoyancy Effects in Fluids.* Cambridge University Press, 1979.

[5] J. Warnatz, U. Maas, and R. W. Dibble. *Combustion.* Springer, 2001.

[6] S. R. Tieszen. On the fluid mechanics of fires. *Annu. Rev. Fluid Mech.*, 67:33, 2001.

[7] J. S. Turner. The 'starting plume' in neutral surroundings. *J. Fluid. Mech.*, 13:356, 1962.

[8] M. Matalon. Intrinsic Flame Instabilites in Premixed and Nonpremixed Combustion. *Annu. Rev. Fluid Mech.*, 39:163, 2007.

[9] W. J. Morgan. Convection Plumes in the Lower Mantle. *Nature*, 230:42, 1971.

[10] J. A. Whitehead and D. S. Luther. Dynamics of Laboratory Diapir and Plume Models. *J. Geo. Res.*, 80:705, 1975.

[11] P. Olson and H. Singer. Creeping plumes. *J. Fluid. Mech.*, 158:511, 1985.

[12] R. W. Griffiths. Entrainment and stirring in viscous plumes. *Phys. Fluids A*, 3:1233, 1991.

[13] B. Gebhart. Instability, Transition, and Turbulence in Buoyancy Induced Flows. *Annu. Rev. Fluid Mech.*, 5:213, 1973.

[14] E. J. List. Turbulent Jets and Plumes. *Annu. Rev. Fluid Mech.*, 14:189, 1982.

[15] R. W. Schmitt. Double Diffusion in Oceanography. *Annu. Rev. Fluid Mech.*, 26:255, 1994.

[16] M. C. Rogers and S. W. Morris. Buoyant Plumes and Vortex Rings in an Autocatalytic Chemical Reaction. *Phys. Rev. Lett.*, 95:024505, 2005.

[17] M. C. Rogers, M. D. Mantle, A. J. Sederman, and S. W. Morris. Conduits of steady-state autocatalytic plumes. *Phys. Rev. E*, 77:026105, 2008.

[18] D. T. Conroy and S. G. L. Smith. Endothermic and exothermic chemically reacting plumes. *J. Fluid. Mech.*, 612:291, 2008.

[19] D. D. Reible. *Fundamentals of environmental engineering.* CRC Press LLC, 1999.

[20] A. M. Leitch, G. F. Davies, and M. Wells. A plume head melting under a rifting margin. *Earth Planet. Sci. Lett.*, 161:161, 1998.

[21] K. Shariff and A. Leonard. Vortex Rings. *Annu. Rev. Fluid Mech.*, 24:235, 1992.

[22] M. Gharib, E. Rambod, and K. Shariff. A universal time scale for vortex ring formation. *J. Fluid. Mech.*, 360:121, 1998.

[23] C. Schram and M. L. Riethmuller. Vortex ring evolution in an impulsively started jet using digital particle image velocimetry and continuous wavelet analysis. *Meas. Sci. and Technol.*, 12:1413, 2001.

[24] M. Shusser and M. Gharib. A model for vortex ring formation in a starting buoyant plume. *J. Fluid. Mech.*, 416:173, 2000.

[25] T. S. Pottebaum and M. Gharib. The pinch-off process in a starting buoyant plume. *Exp. Fluids*, 37:87, 2004.

[26] I. Iglesias, M. Vera, A. L. Sanchez, and A. Linan. Simualtions of starting gas jets at low Mach numbers. *Phys. Fluids*, 17:038105, 2005.

[27] D. J. Shlien. Some laminar and thermal plume experiments. *Phys. Fluids*, 8:1089, 1976.

[28] E. Moses, C. Zocchi, and A. Libchaber. An experimental study of laminar plumes. *J. Fluid. Mech.*, 251:581, 1993.

[29] E. Kaminski and C. Jaupart. Laminar starting plumes in high-Prandtl-number fluids. *J. Fluid. Mech.*, 478:287, 2003.

[30] A. Chay and D. J. Shlien. Scalar fields measurements of a laminar starting plume cap using digital processing interferograms. *Phys. Fluids*, 29:2358, 1986.

[31] J. Tanny and D. J. Shlien. Velocity field measurements of a laminar starting plume. *Phys. Fluids*, 28:1027, 1985.

[32] D. J. Shlien. Transition of the axisymmetric starting plume cap. *Phys. Fluids*, 21:2154, 1978.

[33] C. A. H. Majumder, D. A. Yuen, and A. P. Vincent. Four dynamical regimes for a starting plume model. *Phys. Fluids*, 16:1516, 2004.

[34] A. Hanna, A. Saul, and K. Showalter. Detailed studies of propagating fronts in the iodate oxidation of arsenous acid. *J. Am. Chem. Soc.*, 104:3838, 1982.

[35] R. J. Field and R. M. Noyes. Oscillations in chemical systems. V. Quantitative explanation of band migration in the Belousov-Zhabotinskii reaction. *J. A. Chem. Soc*, 96:2001, 1974.

[36] P. A. Epik and N. S. Shub. Frontalnoe Tetsenie Reaktii Okislenia Arsenita Iodatom *translation:* Frontal progress of the oxidation reaction of arenite with iodate. *Dokl. Akad. Nauk SSSR*, 100:503, 1955.

[37] S. Dushman. The Rate of the Reaction between Iodic and Hydriodic Acids. *J. Phys. Chem.*, 8:453, 1904.

[38] J. R. Roebuck. The Rate of the Reaction between Arsenious Acid and Iodine in Acid Solutions; the Rate of the Reverse Reaction; and the Equilibrium between Them. *J. Phys. Chem.*, 6:365, 1902.

[39] P. De Kepper, I. R. Epstein, and K. Kustin. Systematic Design of Chemical Oscillators. 3. Bistability in the Oxidation of Arsenite by Iodate in a Stirred Flow Reactor. *J. A. Chem. Soc.*, 103:6121, 1981.

[40] H. A. Liebhafsky and G. M. Roe. The Detailed Mechanism of the Dushman Reaction Explored by Computer. *Int. J. Chem. Kinet.*, 11:693, 1979.

[41] J. N. Pendlebury and R. H. Smith. Kinetics of the Reversible Reaction Between Arsenous Acid and Aqueous Iodine. *Int. J. Chem. Kinet.*, 6:663, 1974.

[42] R. J. Field and R. M. Noyes. Oscillations in chemical systems. V. Quantitative explanation of band migration in the Belousov-Zhabotinskii reaction. *J. Am. Chem. Soc.*, 96:2001, 1974.

[43] P. Gray and S. K. Scott. *Chemical Oscillations and Instabilities: Non-Linear Chemical Kinetics.* Oxford University Press, 1990.

[44] A. Saul and K. Showalter. *Oscillations and Traveling Waves in Chemical Systems.* Edited by R. J. Fields and M. Burger. Wiley, 1985. pp 419-439.

[45] J. D'Hernoncourt, A. De Wit, and A. Zebib. Double-diffusive instabilities of autocatalytic chemical fronts. *J. Fluid. Mech.*, 576:445, 2007.

[46] J. A. Pojman, I. R. Epstein, T. J. McManus, and K. Showalter. Convective effects on chemical waves. 2. Simple convection in the iodate-arsenous acid system. *J. Phys. Chem.*, 95:1299, 1991.

[47] D. Vasquez, J. Wilder, and B. Edwards. Convective instability of autocatalytic reaction fronts in vertical cylinders. *Phys. Fluids A*, 4:2410, 1992.

[48] J. Huang, D. A. Vasquez, B. F. Edwards and P. Kolodner. Onset of convection for autocatalytic reaction fronts in a vertical slab. *Phys. Rev. E*, 48:4378, 1993.

[49] M. R. Carey and S. W. Morris and P. Kolodner. Convective fingering of an auto-catalytic reaction front. *Phys. Rev. E*, 53:6012, 1996.

[50] M. Böckmann and S. C. Müller. Growth rates of the buoyancy-driven instability of an autocatalytic reaction front in a narrow cell. *Phys. Rev. Lett.*, 85:2506, 2000.

[51] A. De Wit. Fingering of Chemical Fronts in Porous Media. *Phys. Rev. Lett.*, 87:054502, 2001.

[52] B. F. Edwards. Poiseuille advection of chemical reaction fronts. *Phys. Rev. Lett.*, 89:104501, 2002.

[53] M. Leconte, J. Martin, N. Rakotomalala, and D. Salin. Pattern of reaction diffusion fronts in laminar flows. *Phys. Rev. Lett.*, 90:128302, 2003.

[54] L. Rongy, A. DeWit. Buoyancy-driven convection around chemical fronts traveling in covered horizontal solution layers. *J. Chem. Phys.*, 127:114710, 2007.

[55] T. A. Gribschaw, K. Showalter, D. L. Banville, and I. R. Epstein. Chemical Waves In the Acidic Iodate Oxidation of Arsenite. *J. Phys. Chem.*, 85:2152, 1981.

[56] J. Harrison and K. Showalter. Propagating Acidity Fronts in the Iodate-Arsenous Acid Reaction. *J. Phys. Chem.*, 90:225, 1986.

[57] L. Forstova, H. Sevcikova, M. Marek, and J. H. Merkin. Influence of External Electric Fields on Reaction Fronts in the Iodate-Arsenous Acid System. *J. Phys. Chem. A*, 104:9136, 2000.

[58] L. Forstova, H. Sevcikova, and J. H. Merkin. The influence of the starch indicator on front waves in the iodatearsenous acid system with applied electric fields. *Phys. Chem. Chem. Phys.*, 4:2236, 2002.

[59] J. A. Pojman and I. R. Epstein. Convective effects on chemical waves.1. Mechanisms and stability criteria. *J. Phys. Chem.*, 94:4966, 1990.

[60] D. Horváth, S. Tóth, and Á. Tóth. Periodic Heterogeneity-Driven Resonance Amplification in Density Fingering. *Phys. Rev. Lett.*, 97:194501, 2006.

[61] D. Sharp. An overview of Rayleigh-Taylor instability. *Physica D*, 12:3, 1984.

[62] J. P. Keener and J. J. Tyson. Singular perturbation theory of traveling waves in excitable media (a review). *Physica D*, 32:327, 1988.

[63] K. Mikaelian. Effect of viscosity on Rayleigh-Taylor and Richtmyer-Meshkov instabilities. *Phys. Rev. E*, 47:375, 1993.

[64] J. Martin, N. Rakotomalala, D. Salin, and M. Bockmann. Buoyancy-driven instability of an autocatalytic reaction front in a Hele-Shaw cell. *Phys. Rev. E*, 65:051605, 2002.

[65] B. F. Edwards, J. W. Wilder and K. Showalter. Onset of convection for autocatalytic reaction fronts: Laterally unbounded system. *Phys. Rev. A*, 43:749, 1991.

[66] J. W. Wilder, D. A.Vasquez, and B. F. Edwards. Modification of the eikonal relation for chemical waves to include fluid flow. *Phys. Rev. E*, 47:3761, 1993.

[67] J. D'Hernoncourt, A. Zebib, and A. De Wit. Reaction Driven Convection around a Stably Stratified Chemical Front. *Phys. Rev. Lett.*, 96:154501, 2006.

[68] J. A. Pojman and I. R. Epstein. Convective effects on chemical waves. 2. Simple convection in the iodate-arsenous acid system. *J. Phys. Chem.*, 95:1299, 1991.

[69] J. Masere, D. A. Vasquez, B. F. Edwards, J. W. Wilder, and K. Showalter. Non-axisymmetric and Axisymmetric Convection in Propagating Reaction-Diffusion Fronts. *J. Phys. Chem*, 98:6505, 1994.

[70] E. Jakab, D. Horváth, J. H. Merkin, S. K. Scott, P. L. Simon and Á. Tóth. Isothermal flame balls. *Phys. Rev. E*, 66:016207, 2002.

[71] Á. Tóth, P. Kevei, and D. Horváth. Lateral instability of sphericla reaction balls. *Phys. Rev. E*, 74:036214, 2006.

[72] E. Jakab, D. Horváth, J. H. Merkin, S. K. Scott, P. L. Simon and Á. Tóth. Isothermal flame balls: Effect of autocatalyst decay. *Phys. Rev. E*, 68:036210, 2003.

[73] D. J. Needham, J. H. Merkin. The effects of geometrical spreading in two and three dimensions on the formation of travelling wavefronts in a simple, isothermal, chemical system. *Nonlinearity*, 5:413, 1992.

[74] G. I. Sivashinsky. Diffusional-Thermal Theory of Cellular Flames. *Combust. Sci. Technol.*, 15:137, 1977.

[75] D. Horváth, V. Petrov, S. K. Scott, and K. Showalter. Instabilities in propagating reaction-diffusion fronts. *J. Chem. Phys.*, 98:6332, 1993.

[76] Y. B. Zel'dovich. *Theory of Combustion and Detonation of Gases*. USSR Academy of Sciences, 1944.

[77] P. D. Ronney. Near-Limit Flame Structures at Low Lewis Number. *Combust. Flame*, 82:1, 1990.

[78] P. D. Ronney, K. N. Whaling, A. Abbud-Madrid, J. L. Gatto, and V. L. Pisowicz. Stationary Premixed Flames in Spherical and Cylindrical Geometries. *AIAA J.*, 32:569, 1994.

[79] J. Buckmaster. A Flame-String Model and its Stability. *Combust. Sci. Technol.*, 84:163, 1992.

[80] N. Vladimirova. Model flames in the Boussinesq limit: Rising bubbles. *Combust. Theory and Mod.*, 11:377, 2007.

[81] A. J. Sederman, M. D. Mantle, C. Buckley and L. F. Gladden. MRI techniques for measurement of velocity vectors, acceleration, and autocorrelation functions in turbulent flow. *J. Magn. Reson.*, 166:182, 2004.

[82] M. C. Rogers and S. W. Morris. Natural versus forced convection in laminar starting plumes. *Phys. Fluids*, 21:083601, 2009.

[83] Manufacturers data for glycerine available online from The DOW Chemical Company, http://www.dow.com/glycerine/resources/dwnlit.htm.

[84] E. Buckingham. On Physically Similar Systems: Illustrations of the Use of Dimensional Equations. *Phys. Rev.*, 4:345, 1914.

[85] M. G. Worster. The axisymmetric laminar plume: asymptotic solution for large Prandtl number. *Stud. Appl. Maths*, 75:139, 1986.

[86] A. Einstein. Über die von der molekularkinetischen Theorie der Wärme geforderte Bewegung von in ruhenden Flüssigkeiten suspendierten Teilchen. *Ann. Phys.*, 17:549, 1905.

[87] D. A.Vasquez, B. F. Edwards, and J.W. Wilder. Onset of convection for autocatalytic reaction fronts: Laterally bounded systems. *Phys. Rev. A*, 43:6694, 1991.

[88] W. C. Allee. *Principles of Animal Ecology.* Saunders Publishing, 1949.

[89] J. Veysey and N. Goldenfeld. Simple viscous flows: From boundary layers to the renormalization group. *Rev. Mod. Phys.*, 79:883, 2007.

[90] T. Maxworthy. Accurate measurements of sphere drag at low Reynolds numbers. *J. Fluid Mech.*, 23:369, 1965.

[91] D. Tritton. *Physical Fluid Dynamics, 3rd ed.* Clarendon Press, Oxford, 1988.

[92] E. R. Lindgren. The Motion of a Sphere in an Incompressible Viscous Fluid at Reynolds Numbers Considerably Less Than One. *Phys. Scr.*, 60:97, 1999.

[93] R. M. Davies and G. Taylor. The mechanics of large bubbles rinsing through extended liquids and through liquids in tubes. *Proc. Royal Soc. A*, 200:375, 1950.

[94] A. Zebib and A. De Wit. private communication.

[95] B. S. Martincigh, R. H. Simoyi. Pattern formation fueled by dissipation of chemical energy: Conclusive evidence for the formation of a convective torus. *J. Phys. Chem. A*, 106:482, 2002.

[96] T. Bansagi Jr., D. Horváth, A. Tóth. Multicomponent convection in the chlorite-tetrathionate reaction. *Chem. Phys. Lett.*, 153:384, 2004.

[97] B. R. Morton, G. Taylor, and J. S. Turner. Turbulent gravitational convection form maintained and instantaneous sources. *Proc. R. Soc. Lond. A*, 234:1, 1956.

[98] I. H. Campbell and R. W. Griffiths. Implications of mantle plume structure for the evolution of flood basalts. *Earth Planet. Sci. Lett.*, 99:79, 1990.

[99] J. S. Turner. Buoyant vortex rings. *Proc. R. Soc. Lond. A*, 239:61, 1957.

[100] T. S. Lundgren and N. N. Mansour. Vortex ring bubbles. *J. Fluid. Mech.*, 224:177, 1991.

[101] T. S. Lundgren, J. Yao, N. N. Mansour. Microburst modelling and scaling. *J. Fluid. Mech.*, 239:461, 1992.

[102] D. Fabris and D. Liepmann. Vortex ring structure at late stages of formation. *Phys. Fluids*, 9:2801, 1997.

[103] J. Happel and H. Brenner. *Low Reynolds number hydrodynamics.* Noordhoff International Publishing, 1973.

[104] M. R. Cholemari and J. H. Arakeri. Experiments and a model of turbulent exchange flow in a vertical pipe. *Int. J. Heat Mass Transfer*, 48:4467, 2005.

[105] M. D. Mantle and A. J. Sederman. Dynamic MRI in chemical process and reaction engineering. *Prog. Nucl. Magn. Reson. Spectrosc.*, 43:3, 2003.

[106] L. F. Pratson, J. Imran, G. Parker, J. P. M. Syvitski, and E. Hutton. *Debris Flow vs. Turbidity Currents: a Modeling Comparison of their Dynamics and Deposits.* In: A.H. Bouma and C.G. Stone, (Eds.), Fine-Grained Turbidite Systems. AAPG Memoir 72 and SEPM Special Publication, 2000.

[107] S. V. Patankar. *Numerical Heat Transfer and Fluid Flow.* Hemisphere Publishing Corporation, 1980.

[108] J. H. Ferziger and M. Perić. *Computational Methods for Fluid Dynamics, 3rd Edition.* Springer-Verlag, 2002.

[109] W. F. Bessler and H. Littman . Experimental studies of wakes behind circularly capped bubbles. *J. Fluid. Mech.*, 185:137, 1987.

[110] R. Fitzhugh. Impulses and Physiological States in Theoretical Models of Nerve Membrane. *Biophys. J.*, 1:445, 1961.

[111] A. N. Zaikin and A. M. Zhabotinsky. Concentration wave propagation in two-dimensional liquid-phase self-oscillating system. *Nature*, 225:535, 1970.

[112] J. H. Merkin and D. J. Needham. The development of travelling waves in a simple isothermal chemical system II. Cubic autocatalysis with quadratic and linear decay. *Proc. R. Soc. A*, 430:315, 1990.

[113] J. H. Merkin and D. J. Needham. The development of travelling waves in a simple isothermal chemical system IV. Cubic autocatalysis with quadratic decay. *Proc. R. Soc. A*, 434:531, 1991.

[114] N. Vladimirova. Model flames in the Boussinesq limit: Rising Bubbles. *Combustion Theory and Modelling*, 11:377, 2007.

[115] R. W. Griffiths. Dynamics of mantle thermals with constant buoyancy or anomalous internal heating. *Earth Planet. Sci. Lett.*, 78:435, 1986.